



**FATIGUE AND CYCLIC PLASTICITY OF 304L
STAINLESS STEEL UNDER AXIAL, TORSIONAL
AND PROPORTIONAL AXIAL-TORSIONAL
LOADING**

CAINÃ BEMFICA DE BARROS

**DISSERTAÇÃO DE MESTRADO EM CIÊNCIAS MECÂNICAS
DEPARTAMENTO DE ENGENHARIA MECÂNICA**

FACULDADE DE TECNOLOGIA

UNIVERSIDADE DE BRASÍLIA

**UNIVERSIDADE DE BRASÍLIA
FACULDADE DE TECNOLOGIA
DEPARTAMENTO DE ENGENHARIA MECÂNICA**

**FATIGUE AND CYCLIC PLASTICITY OF 304L
STAINLESS STEEL UNDER AXIAL, TORSIONAL
AND PROPORTIONAL AXIAL-TORSIONAL
LOADING**

CAINÃ BEMFICA DE BARROS

Orientador: PROF. FÁBIO COMES DE CASTRO, PHD. (ENM/UNB)

Coorientador: PROF. EDGAR NOBUO MAMIYA, PHD. (ENM/UNB)

DISSERTAÇÃO DE MESTRADO EM CIÊNCIAS MECÂNICAS

**PUBLICAÇÃO PPGENM-DM 273/2018
BRASÍLIA-DF, 26 DE FEVEREIRO DE 2018.**

**UNIVERSIDADE DE BRASÍLIA
FACULDADE DE TECNOLOGIA
DEPARTAMENTO DE ENGENHARIA MECÂNICA**

**FATIGUE AND CYCLIC PLASTICITY OF 304L
STAINLESS STEEL UNDER AXIAL, TORSIONAL
AND PROPORTIONAL AXIAL-TORSIONAL
LOADING**

CAINÃ BEMFICA DE BARROS

DISSERTAÇÃO DE MESTRADO ACADÊMICO SUBMETIDA AO DEPARTAMENTO DE ENGENHARIA MECÂNICA DA FACULDADE DE TECNOLOGIA DA UNIVERSIDADE DE BRASÍLIA, COMO PARTE DOS REQUISITOS NECESSÁRIOS PARA A OBTENÇÃO DO GRAU DE MESTRE EM ENGENHARIA MECÂNICA.

APROVADA POR:

Prof. Fábio Comes de Castro, PhD. (ENM/UnB)
Orientador

Prof. Jorge Luiz de Almeida Ferreira, PhD. (ENM/UnB)
Examinador Interno

Prof. Francisco Evangelista Junior, PhD. (ENC/UnB)
Examinador Externo

BRASÍLIA, 26 DE FEVEREIRO DE 2018.

FICHA CATALOGRÁFICA

CAINÃ BEMFICA DE BARROS

Fatigue and Cyclic Plasticity of 304L Stainless Steel under Axial, Torsional and Proportional Axial-Torsional Loading

[Distrito Federal] 2018.

x, 85p., 201x297 mm (ENM/FT/UnB, Mestre, Engenharia Mecânica, 2018)

Dissertação de Mestrado - Universidade de Brasília

Faculdade de Tecnologia

Departamento de Engenharia Mecânica

- | | |
|-------------------------|--------------------------|
| 1. Multiaxial Fatigue | 2. Cyclic Plasticity |
| 3. 304L Stainless Steel | 4. Critical Plane Models |
| I. ENM/FT/UnB | II. DM 273/2018 |

REFERÊNCIA BIBLIOGRÁFICA

CAINÃ BEMFICA DE BARROS (2018) Fatigue and Cyclic Plasticity of 304L Stainless Steel under Axial, Torsional and Proportional Axial-Torsional Loading. Dissertação de Mestrado em Ciências Mecânicas, Publicação DM-273/2018, Departamento de Engenharia Mecânica, Universidade de Brasília, Brasília, DF, 85p.

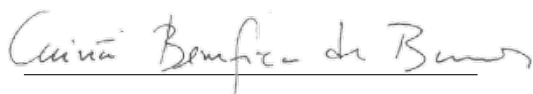
CESSÃO DE DIREITOS

AUTOR: Cainã Bemfica de Barros

TÍTULO: Fatigue and Cyclic Plasticity of 304L Stainless Steel under Axial, Torsional and Proportional Axial-Torsional Loading.

GRAU: Mestre ANO: 2018

É concedida à Universidade de Brasília permissão para reproduzir cópias desta dissertação de Mestrado e para emprestar ou vender tais cópias somente para propósitos acadêmicos e científicos. O autor se reserva a outros direitos de publicação e nenhuma parte desta dissertação de Mestrado pode ser reproduzida sem a autorização por escrito do autor.



Cainã Bemfica de Barros

Rua 12, Chácara 320 n° 20

Vicente Pires, Brasília, DF (CEP: 72007-815)

“Eu quase que nada não sei. Mas desconfio de muita coisa.”

João Guimarães Rosa

Acknowledgements

I would like to thank CNPq (contract 131847/2017-1), which has provided financial support, and Centro Universitário do Distrito Federal (UDF), whose partnership was vital to the machining of the specimens.

I would also like to thank Prof. Fábio Castro, who has always been very thoughtful and of paramount importance to this work; Prof. Edgar Mamiya, who has always provided some important advice and challenging questions; Luiz Carneiro, whose help was essential to the development of the experiments; Leonel Morales, who has always been very helpful with the machining process; my friend Jessica, who has helped me with the photographs of the specimens; and all colleagues and technicians who have helped me throughout this work.

Finally, I would like to thank my parents, without whom I would not be here. And also my friends and family, who have been tolerating me for so long.

Abstract

The goals of this work are to investigate the cyclic stress-strain behaviour and the multiaxial fatigue of the 304L stainless steel through fully reversed strain-controlled axial, torsional and proportional axial-torsional experiments at room temperature and to evaluate the critical plane fatigue models proposed by Smith, Watson and Topper (1970), and Fatemi and Socie (1988) regarding the fatigue life and the macroscopic fatigue crack orientation. Thin-walled tubular specimens machined after a normalization heat treatment were submitted equivalent von Mises strain amplitudes such that $0.20\% \leq \Delta\varepsilon_{eq}/2 \leq 1.00\%$. Due to the rate-dependent cyclic stress-strain behaviour of the 304L stainless steel, all experiments were performed with frequencies (0.30–2.00 Hz) such that the equivalent von Mises strain rate was equal to 10^{-2} s^{-1} . It was observed that the secondary hardening upon proportional loads occurred only for $\Delta\varepsilon_{eq}/2 \geq 0.80\%$, whilst it occurred for all axial and torsional experiments. Based upon the comparison between stress states, it was concluded that fatigue failure occurs before the secondary hardening becomes important for proportional experiments whose $\Delta\varepsilon_{eq}/2 \leq 0.60\%$. A Masing-type behaviour was observed for a range of axial strain $\Delta\varepsilon/2 \leq 0.40\%$ and torsional strain $\Delta\gamma^{sur}/2 \leq 0.61\%$ for axial, torsional and proportional experiments. The equivalent von Mises strain amplitude cannot be used as a threshold since the proportional experiment whose $\Delta\varepsilon_{eq}/2 = 0.50\%$ exhibits a behaviour similar to experiments whose $\Delta\varepsilon_{eq}/2 < 0.50\%$, which does not occur for the axial experiment with the same equivalent strain amplitude. non-proportionality upon deviatoric stress and plastic strain spaces was observed for proportional experiments upon total strain space. Nonetheless, an increase in stress amplitude was not observed for those experiments when compared to axial and torsional ones, which suggests that non-proportional hardening is related to non-proportionality upon the total strain space. There was no significant influence of secondary hardening upon fatigue analysis since there was no significant difference between life predictions generated from material constants obtained from different reference cycles for both models. The investigated models predicted accurately fatigue life, but failed to predict crack orientation for all the three strain histories.

Keywords : Multiaxial Fatigue, Cyclic Plasticity, 304L Stainless Steel, Critical Plane Models

Resumo

Os objetivos deste trabalho são investigar o comportamento tensão-deformação cíclico e a fadiga multiaxial do aço inoxidável 304L por meio de ensaios axiais, torsionais e axiais-torsionais proporcionais totalmente alternados controlados por deformação à temperatura ambiente e avaliar os modelos de fadiga do tipo plano crítico propostos por Smith, Watson e Topper (1970), e Fatemi e Socie (1988) em relação à previsão de vida à fadiga e à orientação das trincas macroscópicas. Corpos de prova tubulares com paredes finas usinados após o tratamento térmico de normalização foram submetidos a amplitudes de deformação equivalente de von Mises tais que $0.20\% \leq \Delta\varepsilon_{eq}/2 \leq 1.00\%$. Devido à dependência da taxa de carregamento do comportamento tensão deformação do aço inoxidável 304L, todos os ensaios foram realizados com frequências (0,30–2,00 Hz) tais que a taxa de deformação equivalente de von Mises fosse igual a 10^{-2} s^{-1} . Observou-se que o endurecimento secundário nos ensaios proporcionais só ocorreu para amplitudes de deformação equivalente $\Delta\varepsilon_{eq}/2 \geq 0,80\%$, enquanto todos os ensaios axiais-torsionais apresentaram endurecimento secundário. Baseado na comparação entre os estados de tensão, concluiu-se que há falha por fadiga antes que o endurecimento secundário se torne significativo para os ensaios proporcionais cuja $\Delta\varepsilon_{eq}/2 \leq 0,60\%$. Observou-se um comportamento do tipo Masing para uma faixa de deformação axial $\Delta\varepsilon/2 \leq 0,40\%$ e torsional $\Delta\gamma^{sur}/2 \leq 0,61\%$ para ensaios axiais, torsionais e proporcionais. A deformação equivalente de von Mises não pode ser usada como parâmetro limite para o comportamento Masing já que o ensaio proporcional cuja $\Delta\varepsilon_{eq}/2 = 0,50\%$ apresenta comportamento semelhante àquele de ensaios cuja $\Delta\varepsilon_{eq}/2 \leq 0,50\%$, o que não ocorre para o ensaio axial de mesma amplitude de deformação equivalente. Observou-se não proporcionalidade nos espaços das tensões desviadoras e das deformações plásticas para os ensaios proporcionais no espaço das deformações totais. No entanto, não se observou um aumento na amplitude de tensão destes ensaios quando comparados a ensaios axiais e torsionais, o que sugere que o endurecimento não proporcional está associado à não proporcionalidade no espaço das deformações totais. Não houve influência significativa do endurecimento secundário na análise de fadiga, já que não houve diferença significativa entre as estimativas de vida realizadas com constantes materiais obtidas de diferentes ciclos de referência para os dois modelos. Os modelos investigados previram a vida à fadiga com boa acurácia, mas falharam em prever a orientação das trincas para todas as três histórias de deformação.

Palavras-chave: Fadiga Multiaxial, Plasticidade Cíclica, Aço Inoxidável 304L, Modelos de Plano Crítico

Contents

1	Introduction	1
1.1	Motivation and objectives	1
1.2	Outline of the dissertation	2
2	Literature Overview	3
2.1	Phase transformation and secondary hardening	3
2.2	Fatigue	6
2.3	Cyclic plasticity	9
3	Multiaxial Fatigue Models	11
3.1	Critical plane models	11
3.2	Non-stabilized cyclic stress-strain behaviour	13
3.3	Fatigue life	14
4	Experimental Procedures	16
4.1	Material, heat treatment and specimens	16
4.2	Fatigue test procedure and crack orientation	17
4.3	Equipments and softwares	19
4.4	Rate-dependence and fatigue test design	24
5	Results and Discussions	27
5.1	Fatigue life	27
5.2	Cyclic stress-strain behaviour	29
5.3	Fatigue models	39
5.4	Further discussion	53
6	Conclusions and Suggestions for Future Work	57
A	Stresses and Strains	I
B	Observed Fatigue Cracks	V

List of Figures

2.1	(a) Bright field photography, (b) dark field α' -martensite reflection, (c) dark field ε -martensite reflection and (d) dark field γ reflection observed after 258 loading blocks of a plastic-strain controlled tension-compression experiment whose $\Delta\varepsilon^p/2 = 0.5\%$ (Bayerlein et al., 1989). Observations made by transmission electron microscope (TEM).	4
2.2	Two α' -martensite morphologies observed after (A) a direct transformation and (B) a three-stage transformation (Hennessy et al., 1976). Observations made by light microscopy.	4
2.3	Secondary hardening upon strain-controlled (a) axial and (b) torsional tests (Kalnaus, 2009).	5
2.4	Classification of fatigue cracking behaviour according to Jiang (2000).	8
2.5	Cracking behaviour of 304 stainless steel tested under torsion strain-controlled conditions (Bannantine and Socie, 1988).	8
3.1	Hysteresis Loops for two prescribed shear strain amplitudes at half fatigue life cycle.	13
3.2	Smith–Watson–Topper fatigue parameter during fully reversed strain-controlled test for a 7050-T7451 aluminium alloy and the 304L stainless steel.	14
4.1	Thin-walled tubular specimens used in fatigue experiments, all dimensions in mm (Carneiro Junior, 2017).	17
4.2	Axial-torsional strain paths.	18
4.3	Crack orientation convention.	19
4.4	MTS 632.80F-04 axial-torsional extensometer.	20
4.5	MTS 809 axial-torsional test system.	20
4.6	Proposed amplitude measures for (a) stress and (b) plastic strain amplitude for a non-proportional loading path (Jiang and Kurath, 1997a).	24
5.1	Equivalent strain amplitude vs. fatigue life for axial, torsional and axial-torsional proportional loading.	27
5.2	Equivalent stress amplitude vs. number of loading cycles for strain-controlled axial, torsional and proportional loading.	30

5.3	Equivalent stress amplitude vs. fatigue life percentage for strain-controlled axial, torsional and proportional loading.	31
5.4	Equivalent stress amplitude vs. number of loading cycles for $\Delta\varepsilon_{eq}/2 = 0.20\%$ and $\Delta\varepsilon_{eq}/2 = 1.00\%$	32
5.5	Normalized stress amplitude vs. fatigue life percentage for proportional experiments whose $\Delta\varepsilon_{eq}/2 = 0.80\%$ and $\Delta\varepsilon_{eq}/2 = 1.00\%$	32
5.6	Axial stress range vs. axial plastic strain range for axial loading.	33
5.7	Shear stress range vs. plastic shear strain range for torsional loading.	33
5.8	Axial stress range vs. axial plastic strain range for proportional loading.	34
5.9	Shear stress range vs. plastic shear strain range for proportional loading.	34
5.10	Axial stress range vs. axial plastic strain range for axial and proportional loading for selected amplitudes.	35
5.11	Axial stress range vs. axial plastic strain range for axial and proportional loading for selected amplitudes.	35
5.12	Total strain paths for selected proportional experiments.	37
5.13	Plastic strain paths for selected proportional experiments.	37
5.14	Stress paths for selected proportional experiments.	38
5.15	Equivalent stress amplitude vs. equivalent plastic strain amplitude for minimum softening.	38
5.16	Smith–Watson–Topper material constants obtained from three different error functions at half fatigue life.	41
5.17	Life prediction for the Smith–Watson–Topper model for three different sets of material constants obtained from different error functions at half fatigue life.	41
5.18	Smith–Watson–Topper material constants for different reference cycles.	42
5.19	Smith–Watson–Topper fit for half fatigue life.	43
5.20	Fatemi–Socie material constants for different reference cycles.	43
5.21	Fatemi–Socie fit for half fatigue life.	44
5.22	Smith–Watson–Topper life estimates for $0.2N_f$	45
5.23	Smith–Watson–Topper life estimates for $0.5N_f$	45
5.24	Smith–Watson–Topper life estimates for $0.8N_f$	46
5.25	Smith–Watson–Topper life estimates for maximum softening.	46
5.26	Smith–Watson–Topper life estimates for average fatigue parameter.	47
5.27	Fatemi–Socie life estimates for $0.2N_f$	47
5.28	Fatemi–Socie life estimates for $0.5N_f$	48
5.29	Fatemi–Socie life estimates for $0.8N_f$	48
5.30	Fatemi–Socie life estimates for maximum softening.	49
5.31	Observed and predicted fatigue crack angle based upon the Smith–Watson–Topper for axial loading.	50
5.32	Observed and predicted fatigue crack angle based upon the Smith–Watson–Topper for torsional loading.	50

5.33	Observed and predicted fatigue crack angle based upon the Smith–Watson–Topper for proportional loading.	51
5.34	Observed and predicted fatigue crack angle based upon the Fatemi–Socie for axial loading.	51
5.35	Observed and predicted fatigue crack angle based upon the Fatemi–Socie for torsional loading.	52
5.36	Observed and predicted fatigue crack angle based upon the Fatemi–Socie for proportional loading.	52
5.37	Shear hysteresis loops for selected proportional experiments.	53
5.38	Crack orientation vs prescribed shear strain amplitude for torsional and proportional experiments.	56

List of Tables

4.1	Monotonic properties of the 304L stainless steel (Carneiro Junior, 2017).	16
4.2	Chemical composition of the 304L stainless steel, weight %	16
5.1	Fatigue test data for the 304L stainless steel.	28

List of Symbols

ε	Strain Tensor
σ	Cauchy Stress Tensor
\mathbf{S}	Deviatoric Stress Tensor
γ	Shear Strain
γ^{sur}	Surface Shear Strain
γ^{mid}	Middle Shear Strain
$\Delta\gamma$	Shear Strain Range
$\Delta\gamma/2$	Shear Strain Amplitude
$\Delta\gamma^p/2$	Plastic Shear Strain Amplitude
$\Delta\varepsilon$	Axial Strain Range
$\Delta\varepsilon/2$	Axial Strain Amplitude
$\Delta\varepsilon_{eq}/2$	Equivalent von Mises Strain Amplitude
$\Delta\varepsilon^p/2$	Plastic Axial Strain Amplitude
$\Delta\varepsilon_{eq}^p/2$	Equivalent Plastic Axial Strain Amplitude
$\Delta\sigma/2$	Axial Stress Amplitude
$\Delta\sigma_{eq}/2$	Equivalent Stress Amplitude
$\Delta\tau/2$	Shear Stress Amplitude
ε	Axial Strain
ε^e	Elastic Axial Strain
ε_{eq}	Equivalent von Mises Strain
$\dot{\varepsilon}_{eq}$	Equivalent von Mises Strain Rate
ε_f	Strain at Fracture
ε^p	Plastic Axial Strain
ε_0	Material Constant
θ	Fatigue Crack Orientation
θ_{Twist}	Angle of Twist
λ	Biaxial Strain Ratio
ν	Poisson's Ratio
σ	Axial Stress
σ_{collet}	Collet Pressure
σ_{eq}	Equivalent von Mises Stress Amplitude
σ_m	Mean Axial Stress

σ_{nmax}	Maximum Normal Stress
σ_u	Ultimate Tensile Stress
σ_y	Monotonic 0.2% Yield Stress
τ	Shear Stress
τ_m	Mean Shear Stress
ϕ	Phase Angle
ω	Angular Frequency
C	Material Constant
D	Outer Diameter
d	Inner Diameter
D_{grip}	Outer Diameter in the Grip End
E	Young's Modulus
f	Frequency
F	Ratio between Estimated and Observed Fatigue Life
FD	Fatigue Damage
FD _c	Critical Fatigue Damage
FP	Fatigue Parameter
FP ₀	Material Constant
k	Material Constant
L	Gauge Length
P	Axial Force
N_f	Observed Fatigue Life
N_{est}	Estimated Fatigue Life
R_ϵ	Strain Ratio
T	Torque
v	Material Constant
\mathcal{E}	Least Squares Error Function
\mathcal{E}'	Relative Error Function
\mathcal{E}''	Logarithmical Error Function

Chapter 1 – Introduction

1.1 Motivation and objectives

Fatigue failure is an important aspect of engineering design since many components are submitted to cyclic loading, which are usually of multiaxial nature. Hence, multiaxial experiments designed to investigate the cyclic plasticity and the fatigue behaviour of engineering materials are essential to predict the fatigue life of these components. Similarly, it is also necessary to develop multiaxial fatigue models that can be applied to a wide range of complex loading, as variable amplitude ones, and cyclic plasticity models that incorporate the material phenomena observed during cyclic loading.

Stainless steels are steels that have at least 10.5% chromium content by mass. Those steels exhibit an important corrosion resistance due to the presence of this chemical element, which may be accompanied by other elements, as nickel, molybdenum and manganese. The Society of Automotive Engineers (SAE) proposed a classification for the stainless steels based upon the chemical content and crystalline structure. The 300 series is composed of austenitic chromium-nickel alloys, such as the Type 302, Type 304 and Type 306.

The 304L stainless steel is a low carbon version of the Type 304 stainless steel that has many industrial applications, like pressurized water nuclear reactors (Haddar and Fissolo, 2005; Zinkle and Was, 2013), aeronautical (Huda and Edi, 2013; Kral et al., 2018) components, pipelines (Martins et al., 2014), and pressure and chemical vessels (Chopra and Gavenda, 1998; Yoon et al., 2015). Despite the widespread industrial application of this material, it exhibits many material phenomena that are still subject of research, as the non-proportional hardening (Krempf and Lu, 1984), secondary hardening (Bayerlein et al., 1989; Mughrabi and Christ, 1997), rate-dependence of the stress-strain behaviour (Krempf, 1979), creep and ratcheting (Taleb and Cailletaud, 2011), and crack orientation dependent upon loading amplitude (Bannantine and Socie, 1988; Kalnaus, 2009).

In this work, several phenomena of cyclic plasticity and the multiaxial fatigue behaviour of the 304L stainless steel will be investigated. The main objectives of this work are:

- Perform fully reversed axial-torsional proportional experiments in order to supplement the fully reversed axial and torsional experiments performed by Carneiro Junior (2017).

- Investigate the cyclic stress-strain behaviour of the 304L stainless steel, especially the secondary hardening, the non-Masing behaviour and the proportionality upon the deviatoric stress, total and plastic strain spaces.
- Analyse the influence of the secondary hardening upon fatigue life estimates, as well as evaluate the critical plane models proposed by Smith, Watson and Topper (1970), and Fatemi and Socie (1988) regarding crack orientation and fatigue life predictions.

1.2 Outline of the dissertation

This dissertation is composed of five chapters: in Chapter 2, a review of the phenomenon of martensitic phase transformation, of the fatigue literature and of the cyclic plasticity of the 304L stainless steel will be introduced; in Chapter 3, the critical plane fatigue models of Smith, Watson and Topper (1970) and Fatemi and Socie (1988), which will be used in this work, will be briefly discussed; in Chapter 4, the experimental procedures and methodology, as well as the program developed to post-process experimental data, will be exposed; in Chapter 5, experimental results and the subsequent analysis will be presented and discussed; and in Chapter 6, the conclusions and suggestions for future works will be presented.

Chapter 2 – Literature Overview

In this section, it is presented a literature review of the martensitic phase transformation, which is the cause of the secondary hardening, a late cyclic hardening phenomenon; uniaxial and multiaxial fatigue, as well as the fatigue cracking behaviour of the 304L stainless steel; and the cyclic plasticity phenomena of rate-dependence, creep, ratcheting and non-proportional hardening.

2.1 Phase transformation and secondary hardening

The 304L stainless steel is a metastable austenitic steel that may undergo martensitic transformation induced by temperature or by plastic deformation at room temperature (Bayerlein et al., 1989). Two martensitic phases have been observed upon both temperature and deformation-induced transformations (Reed, 1962): α' -martensite, a body centred cubic (BCC) phase, and ε -martensite, a hexagonal close-packed (HCP) phase. The α' -martensite formation may occur directly from γ -austenite phase or from an intermediate ε -martensite, with the latter occurring especially near stacking faults (Bayerlein et al., 1989). The α' -martensite morphology depends upon the formation process: for the direct transformation, an elongated block shape occurs, whilst a lathlike shape is observed for a three-stage transformation. Experimental evidence of the formation of α' and ε -martensite for a plastic-strain controlled tension-compression experiment performed by Bayerlein et al. (1989) and the two α' -martensite phases observed by Hennessy et al. (1976) after 1031 reversals of a fully reversed strain-controlled tension-compression experiment performed at 93°C (366K) whose $\Delta\varepsilon/2 = 1.5\%$ are shown in Figures 2.1 and 2.2.

Due to martensitic transformation, the 304L stainless steel exhibits a phenomenon called secondary hardening when submitted to cyclic deformation (Mughrabi and Christ, 1997). Therefore, there may be a late increase in stress amplitude throughout strain-controlled experiments. An important consequence is that the notion of a stabilized stress-strain hysteresis loop, which is often used in fatigue analysis, may not be appropriated for this material. To illustrate this phenomenon, the stress amplitude vs. the number of loading cycles for axial and torsional strain-controlled experiments performed by Kalnaus (2009) upon a 304L stainless steel is shown in Figure 2.3.

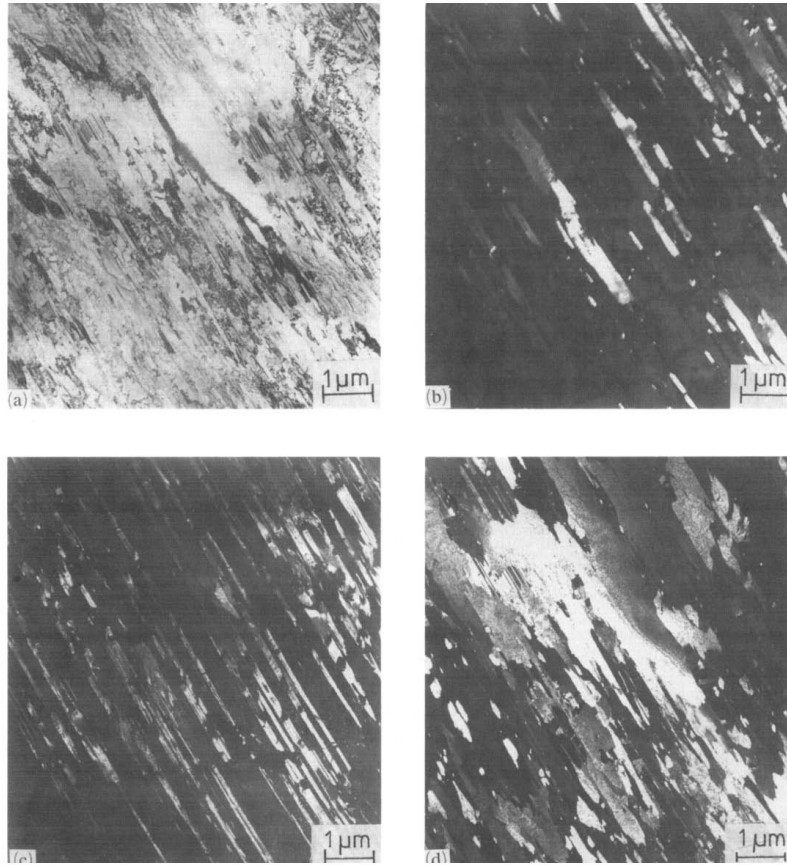


Figure 2.1: (a) Bright field photography, (b) dark field α' -martensite reflection, (c) dark field ε -martensite reflection and (d) dark field γ reflection observed after 258 loading blocks of a plastic-strain controlled tension-compression experiment whose $\Delta\varepsilon^p/2 = 0.5\%$ (Bayerlein et al., 1989). Observations made by transmission electron microscope (TEM).

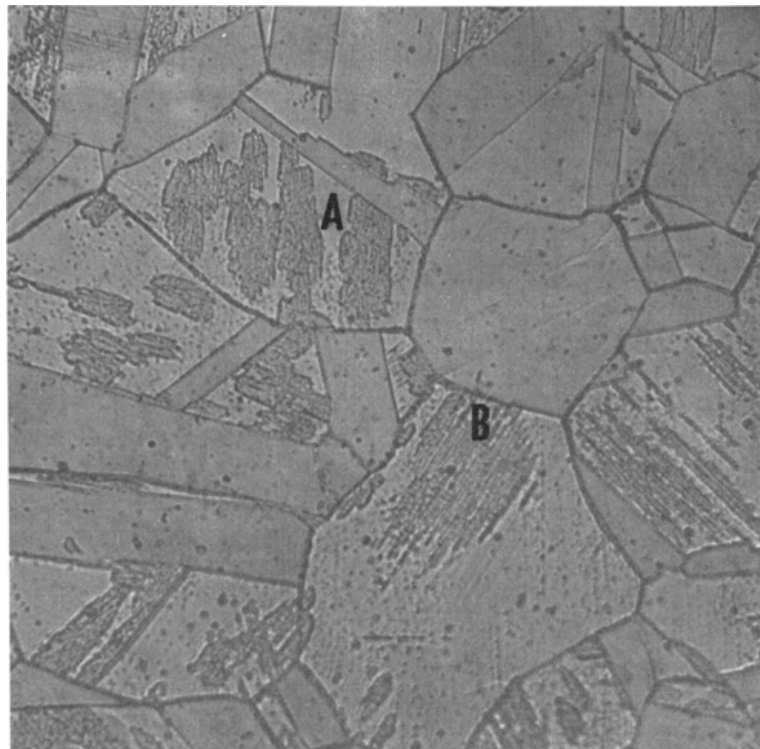


Figure 2.2: Two α' -martensite morphologies observed after (A) a direct transformation and (B) a three-stage transformation (Hennessy et al., 1976). Observations made by light microscopy.

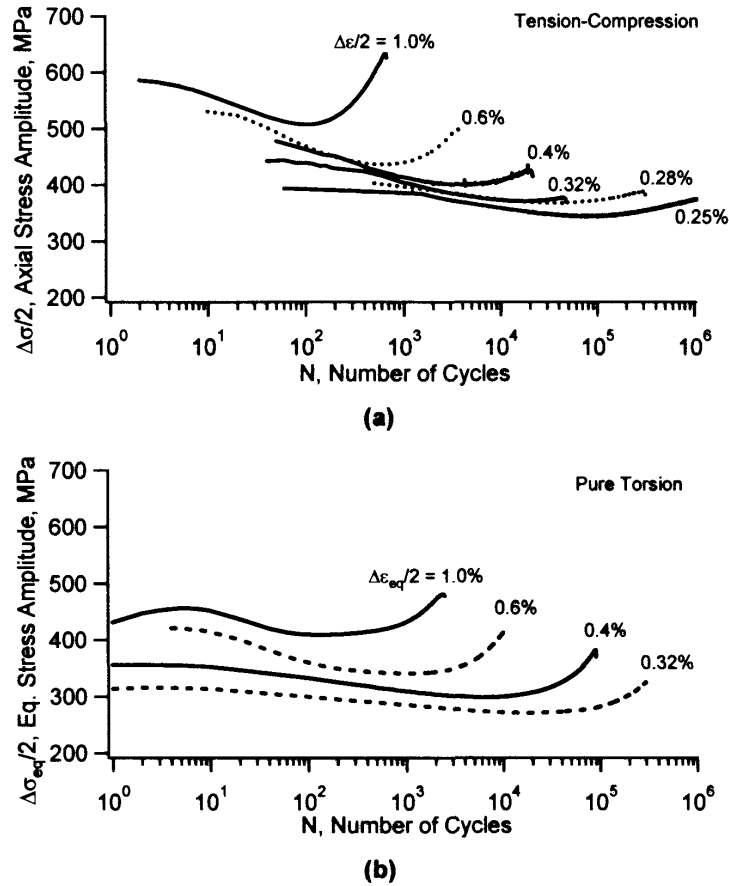


Figure 2.3: Secondary hardening upon strain-controlled (a) axial and (b) torsional tests (Kalnaus, 2009).

Martensitic transformation does not occur for all stress states. Several authors did not observe secondary hardening upon cyclic loads and attempted to determine whether martensitic transformation would occur based upon a total or plastic strain amplitude threshold:

1. Baudry and Pineau (1977) observed negligible secondary hardening for $\Delta\varepsilon^p/2 < 0.18\%$ at room temperature and for $\Delta\varepsilon^p/2 < 0.50\%$ at 50 °C (323 K).
2. Bayerlein et al. (1989) observed negligible secondary hardening for $\Delta\varepsilon^p/2 < 0.30\%$ at room temperature.
3. Krupp et al. (2001) observed negligible secondary hardening for $\Delta\varepsilon^p/2 < 0.30\%$ at room temperature.
4. Kalnaus (2009) observed almost insignificant secondary hardening for fully reversed 90° out-of-phase non-proportional loads at room temperature for an equivalent von Mises strain amplitude $\Delta\varepsilon_{eq}/2 \leq 0.40\%$.
5. Colin et al. (2010) observed secondary hardening upon uniaxial experiments at room temperature in which $R_\varepsilon = -1$, $R_\varepsilon = 2$ and $R_\varepsilon = \infty$ for strain amplitudes $\Delta\varepsilon/2 \leq 0.25\%$.
6. Vincent et al. (2012) observed secondary hardening upon uniaxial experiments at room

temperature whose $\Delta\varepsilon/2 \leq 0.20\%$. On the other hand, it was also observed that cyclic softening and secondary hardening are almost negligible if there is a positive mean stress, especially for large strain amplitudes.

2.2 Fatigue

2.2.1 Uniaxial fatigue

There have been several works that investigated the uniaxial fatigue behaviour of this material:

1. Baudry and Pineau (1977) investigated the influence of temperature upon strain-life curves up to 10^5 cycles and observed that low cycle fatigue life was longer at the range 50–70 °C (323–348 K), and that the formation of α' -martensite accelerated both crack initiation and propagation.
2. Colin (2010) observed that prestraining produced several shallow microcracks, with more microcracks being observed upon High-Low than Low-High two-step sequence loading. Nonetheless, those microcracks did not affect significantly fatigue failure, which was caused by the presence of macrocracks. It was also observed that this material features loading sequence effects, which was verified by Belattar et al. (2012) too.
3. Colin (2010) also observed mean stress relaxation for experiments whose $R_\varepsilon \neq -1$, and that they lasted longer than specimens subjected to fully reversed loadings.
4. Müller-Bollenhagen et al. (2010) investigated the very high cycle fatigue behaviour of this material and observed no failure (up to 10^9 cycles) upon 304 stainless steel specimens for $\Delta\sigma/2 \leq 250$ MPa.
5. Vincent et al. (2012) investigated the high cycle fatigue behaviour of the 304L stainless steel and observed that a stress amplitude parameter and the fatigue parameter proposed by Smith, Watson and Topper (1970) predicted accurately fatigue life based upon the maximum softening cycle.

2.2.2 Multiaxial fatigue

Some important work upon multiaxial fatigue of the 304L stainless steel are presented below:

1. Socie (1987) performed strain-controlled experiments upon thin-walled tubular specimens using six different strain paths: axial, torsional, proportional, 90° out-of-phase, box and two boxes. It was observed that the fatigue parameter proposed by Smith, Watson and Topper (1970) correlated well the observed fatigue lives, which was attributed to the agreement between the observed fatigue crack mode and the one assumed by this fatigue model.

2. Itoh et al. (1995) performed experiments upon thin-walled tubular specimens of 304 stainless steel using fourteen axial-torsional strain paths, including proportional and complex non-proportional paths. It was observed a reduction up to a factor of ten upon fatigue life for non-proportional experiments when compared to proportional paths with equal strain amplitude. In addition, an equivalent non-proportional strain range parameter was proposed and successfully tested in order to render unnecessary a cyclic plasticity model that incorporates non-proportional hardening whilst estimating fatigue life.
3. Jiang (2000) verified that a proposed incremental fatigue damage model based upon the concept of plastic strain energy could accurately predict fatigue life for the experimental data obtained by Itoh et al. (1995) and Jiang and Kurath (1997b).
4. Shamsaei et al. (2011) performed proportional experiments upon tubular specimens with four strain paths: three fully reversed in which the angle $\theta = \arctan \gamma / \sqrt{3} \varepsilon$ increment was 1° , 15° and random, and a unbalanced path such that $R_\varepsilon = R_\gamma = 0$ with an angle increment of 1° . It was observed that an additional hardening occurred for loadings in which the angle varied randomly, whilst it does not occur for the other experiments. Nonetheless, there was no impact upon observed fatigue life. The fatigue model proposed by Fatemi and Socie (1988) accurately predicted both fatigue life and crack orientation.

2.2.3 Fatigue cracking behaviour

Fatigue cracking behaviour depends upon the material, the stress state and the loading amplitude (Bannantine and Socie, 1988; Zhao and Jiang, 2008; Kalnaus, 2009; Castro and Jiang, 2016). Jiang (2000) proposed a classification based upon the crack orientation of axial and torsional loads, illustrated in Figure 2.4: a shear mode material exhibits crack orientations that coincide with the orientation of the planes in which shear stress is maximum ($\pm 45^\circ$ for axial loads, and 0 and 90° for torsional ones); a tensile mode material exhibits crack orientations that coincide with the orientation of the planes in which normal stress is maximum (0 for axial loads, and $\pm 45^\circ$ for torsional ones); and a mixed mode material exhibits crack orientations that coincide with the orientation of the planes in which normal stress is maximum for axial loads, and with planes in which shear stress is maximum for torsional ones.

Bannantine and Socie (1988) observed three cracking behaviour regions for the 304 stainless steel: region I, characterized by crack initiation upon grain boundaries and slip band, with the nucleation of a myriad of small cracks that coalesced into a large crack; region II, characterized by the bifurcation of region I obstructed cracks in the direction of the maximum tensile stress; and region III, characterized by the nucleation of few cracks that bifurcated too, like cracks of region II, and failure by crack growth instead of crack coalescence. The three regions are shown in Figure 2.5.

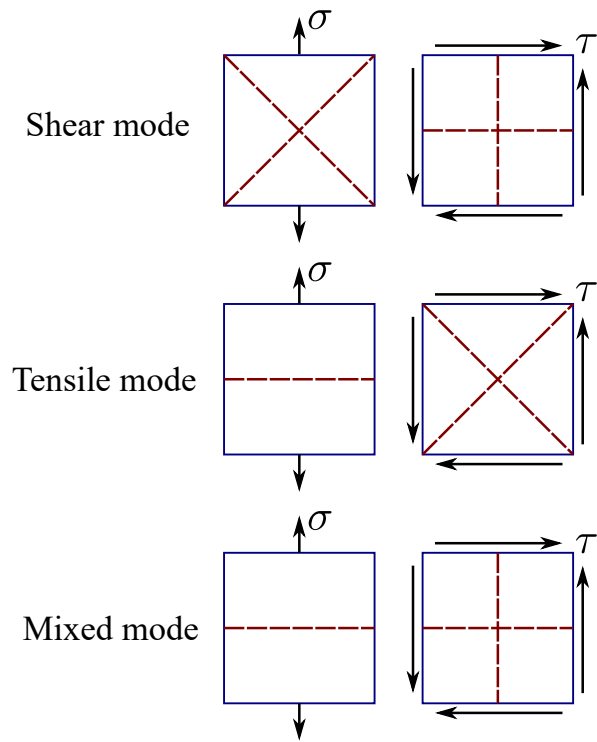


Figure 2.4: Classification of fatigue cracking behaviour according to Jiang (2000).

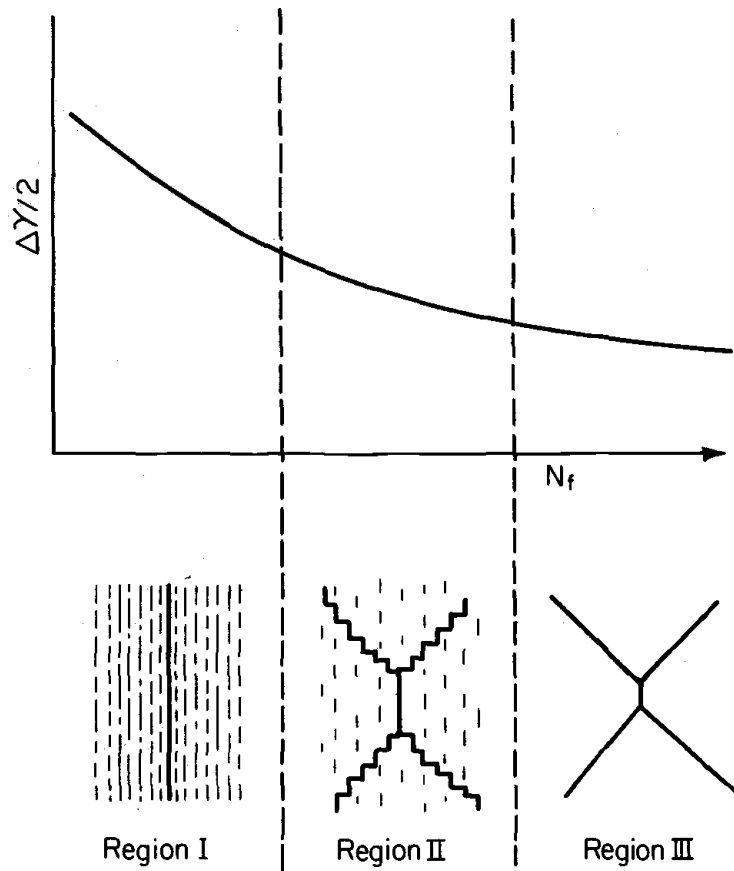


Figure 2.5: Cracking behaviour of 304 stainless steel tested under torsion strain-controlled conditions (Bannantine and Socie, 1988).

Kalnaus (2009) observed that the cracking behaviour of the 304L stainless steel is dependent upon the load as well. For axial loads, a tensile cracking behaviour was observed, whilst for torsional loads, cracking behaviour was dependent upon shear strain amplitude: for $\Delta\gamma/2 \geq 0.7\%$, a shear mode was observed; for $\Delta\gamma/2 < 0.7\%$, a tensile mode was observed. Therefore, based upon Figure 2.4, the crack behaviour of the 304L stainless steel can be classified as mixed or tensile mode, depending upon the strain amplitude.

2.3 Cyclic plasticity

The cyclic stress-strain behaviour of the 304L stainless steel has been extensively investigated due to its complexity. It exhibits many effects, as rate-dependence, creep, ratcheting, non-proportional hardening, secondary hardening, mean stress relaxation (Colin et al., 2010), pre-hardening (Belattar et al., 2016; Colin et al., 2010) and load history dependence (Belattar et al., 2012), etc. In this work, a review of rate-dependence, creep, ratcheting and non-proportional hardening of the 304L stainless steel will be presented.

2.3.1 Rate-dependence, creep and ratcheting

Krempf (1979) observed that both monotonic and cyclic uniaxial behaviour of the 304L stainless steel were dependent upon the strain or the stress rate at room temperature, and that there is a significant inelastic strain accumulation due to creep during monotonic and cyclic loads. Some works have evaluated whether various cyclic plasticity models could predict uniaxial and multiaxial creep and ratcheting of the 304L stainless steel:

1. Yoshida (1990) applied a model previously developed by Liu and Krempf (1979) for cyclic creep, which yields reasonable results for high positive mean stress.
2. Kang et al. (2004) proposed a unified visco-plastic model that accurately predicted a uniaxial and four different non-proportional experiments.
3. Hassan et al. (2008) evaluated a modified Chaboche (Bari and Hassan, 2002) and a multi-mechanism (Taleb et al., 2006) models for non-proportional experiments and obtained, for single sequence loading paths, better results for the modified Chaboche than the multi-mechanism, and, for double sequence loading path, unsatisfactory results for both models.

2.3.2 Non-proportional hardening

Lamba and Sidebottom (1978a) performed some experiments upon annealed copper and verified that, during non-proportional loads, there was an increase of axial peak stress up to 40 % when compared with a uniaxial experiment with the same axial strain, a phenomenon so-called

non-proportional hardening. Doong et al. (1990) investigated the microstructure of four materials (1100 aluminium, OFHC copper, and type 304 and 310 stainless steel) after they were submitted to in-phase and 90° out-of-phase loads, and attributed non-proportional hardening to the change of dislocation substructures. Krempl and Lu (1984) performed four experiments in which a loading sequence composed of axial, torsional, in-phase and 90° out-of-phase blocks were applied upon a thin-walled 304L stainless steel specimen, and observed a threefold increase upon equivalent von Mises stress amplitudes.

There have been some attempts to incorporate this phenomenon into cyclic plasticity models:

1. Lamba and Sidebottom (1978b) compared the simulated results of three kinematic hardening rules (Prager, 1955; Ziegler, 1959; Mróz, 1969) with experimental data from Lamba and Sidebottom (1978a), and obtained unsatisfactory results for all models. However, a combination of the Tresca yield surface and the Mróz kinematic hardening provided excellent predictions.
2. Tanaka (1994) proposed a non-proportional parameter that depends upon a fourth-order tensor that describes the dislocation structure, incorporated it into a viscoplastic model developed by Chaboche and Rousselier (1983), and successfully simulated some experimental data for the 316 stainless steel.
3. Itoh et al. (2000) proposed a model that consisted of the combination of the kinematic hardening rules of Mróz (1969) and Ziegler (1959), and a non-proportional hardening factor, which successfully predicted the stabilized cyclic stress-strain behaviour of fourteen strain paths for the 304L stainless steel.

Chapter 3 – Multiaxial Fatigue Models

In this work, two fatigue models capable of predicting both the fatigue life and the orientation of the fatigue cracking plane will be evaluated: the multiaxial version of the Smith, Watson and Topper (1970) and the Fatemi and Socie (1988) models. It is important to emphasize that those models predict crack **initiation**, which is assumed to be a macroscopic crack. A brief review of stresses and strains upon a thin-walled tubular specimen is presented in Appendix A.

3.1 Critical plane models

3.1.1 Smith–Watson–Topper model

Smith, Watson and Topper (1970) originally proposed a uniaxial model to consider the effect of mean stress in fatigue life. Later, Socie (1987) proposed a multiaxial version of this model based upon the critical plane concept. The fundamental hypothesis of this model is that the maximum normal stress σ_{nmax} and the normal strain amplitude $\Delta\varepsilon/2$ acting at a material plane are the driving forces of fatigue in metals. The critical plane is the plane in which the product between maximum normal stress and normal strain is maximum. The mathematical description of this model is

$$\text{FP}_{\text{SWT}} = \sigma_{\text{nmax}} \frac{\Delta\varepsilon}{2} = g(N_f), \quad (3.1)$$

in which g is a function of the fatigue life N_f . For a fully reversed axial load, both the maximum normal stress and the strain amplitude maximum values occur at the plane $\theta = 0$. For a torsional load, the critical planes are $\theta = \pm 45^\circ$.

3.1.2 Fatemi–Socie model

Fatemi and Socie (1988) proposed a multiaxial fatigue model that assumed the maximum shear strain amplitude acting at a material plane to be the driving force of the fatigue crack initiation. It is a modification of the Brown and Miller (1973) model, which depended upon principal

strains ε_1 and ε_3 , to consider non-proportional hardening by replacing the normal strain by the normal stress. The mathematical description of this model is

$$\text{FP}_{\text{FS}} = \frac{\Delta\gamma_{\text{max}}}{2} \left(1 + k \frac{\sigma_{\text{nmax}}}{\sigma_y} \right) = g(N_f). \quad (3.2)$$

In Equation 3.2, $\Delta\gamma_{\text{max}}/2$ is the maximum shear strain amplitude, σ_{nmax} is the maximum normal stress at the plane in which $\Delta\gamma_{\text{max}}/2$ is maximum, σ_y is the monotonic yield stress of the material, and $g(N_f)$ is a function of the fatigue life. The material constant k , which correlates axial and torsional data, could be determined by fitting experimental data of axial and torsional of experiments and may vary throughout the loading cycles (Socie and Marquis, 1997). In this work, it will be assumed to be a constant, as adopted by Jiang et al. (2007).

For a fully reversed axial load, the maximum shear strain amplitude occurs at the plane $\theta = \pm 45^\circ$. For a torsional load, it occurs at $\theta = 0$ and $\theta = 90^\circ$. Originally, Fatemi and Socie (1988) defined the critical plane as the plane in which shear strain was maximum, which means that the critical plane **does not** depend upon fatigue parameters for axial and torsional loads. Therefore, it is possible that fatigue parameter maximum value is not the one of the critical plane. Chu (1995) argued that, if there is any influence of the maximum stress/strain upon fatigue crack nucleation, it should be taken into account for all planes. It follows that the critical plane could be defined as the plane in which fatigue parameter is maximum rather than the original definition. Hence,

$$\left[\frac{\Delta\gamma}{2} \left(1 + k \frac{\sigma_{\text{nmax}}}{\sigma_y} \right) \right]_{\text{max}} = g(N_f). \quad (3.3)$$

The critical plane may now depend upon the parameter k . For the Smith–Watson–Topper model, the critical plane for an axial or a torsional load remains the same whichever definition of critical plane (maximum normal strain or combination of normal stress and normal strain) is assumed. In this work, a maximization of the fatigue parameter was adopted.

3.1.3 Critical plane definition

According to Socie and Marquis (1997):

“From a mathematical point of view the maximum stress or strain exists on only one plane. From a fatigue and fracture of materials viewpoint, any plane near the maximum stress or strain plane will experience the effects of the applied loading.”

In the light of this point of view, critical planes may be defined as the planes in which fatigue parameter is greater than a given percentage of the maximum fatigue parameter. In this work, if the fatigue parameter at a given plane is such that $\text{FP} \geq 0.9\text{FP}_{\text{max}}$, it will be considered a critical plane, similar to Jiang et al. (2007). Note that the choice of which percentage is used is arbitrary.

3.2 Non-stabilized cyclic stress-strain behaviour

The stresses and strains of Equations 3.1 and 3.2 are the ones of the stabilized hysteresis loop, which is usually assumed to be the half fatigue life cycle. However, as reported in Section 2.1, the 304L stainless steel may exhibit secondary hardening, which means that there may be no stabilized elastic-plastic behaviour for this material. The hysteresis loops at half fatigue life cycle of two torsional experiments performed by Carneiro Junior (2017) are shown in Figure 3.1

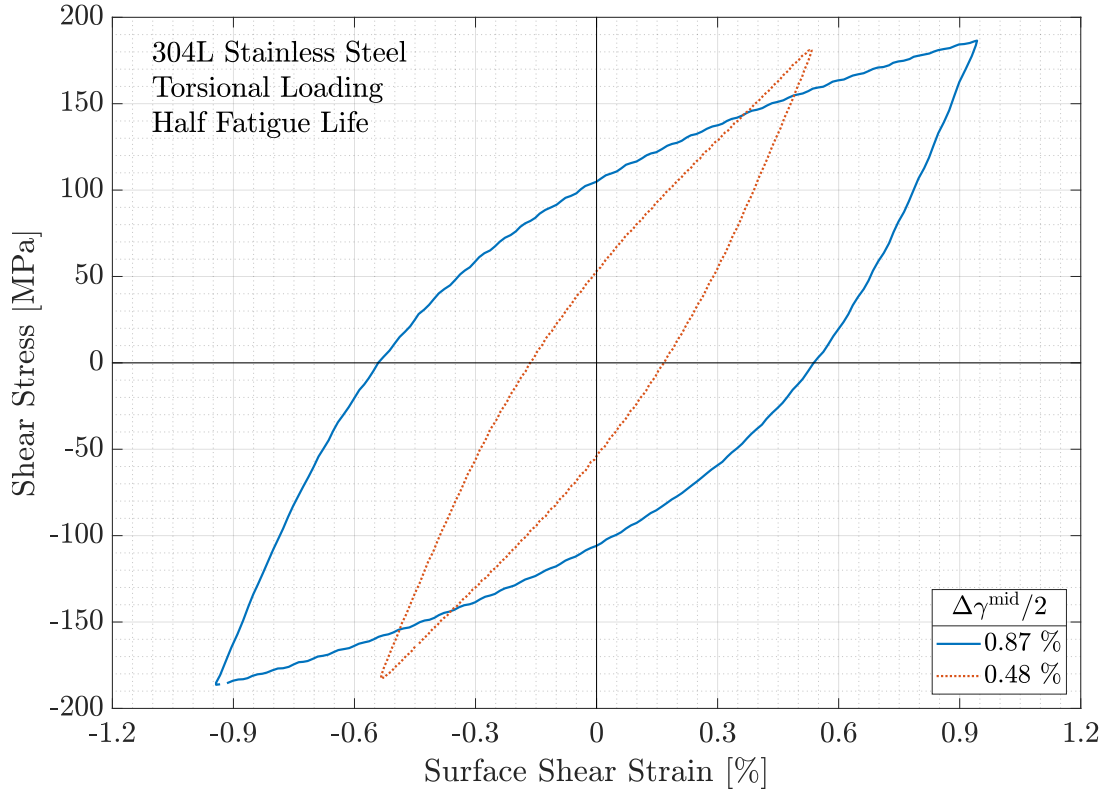


Figure 3.1: Hysteresis Loops for two prescribed shear strain amplitudes at half fatigue life cycle.

The shear stress amplitude is approximately the same for two experiments whose strain amplitudes are significantly different. Although this may seem contradictory, it is a consequence of the assumption that the half fatigue life cycle is representative of the whole elastic-plastic cyclic behaviour. On the other hand, for materials whose behaviour does not vary significantly during a test, this assumption is very reasonable. Another important consequence is that fatigue parameters may vary significantly during the experiments, as shown in Figure 3.2 for a 7050-T7451 aluminium alloy (Hernández, 2016) and the 304L stainless steel.

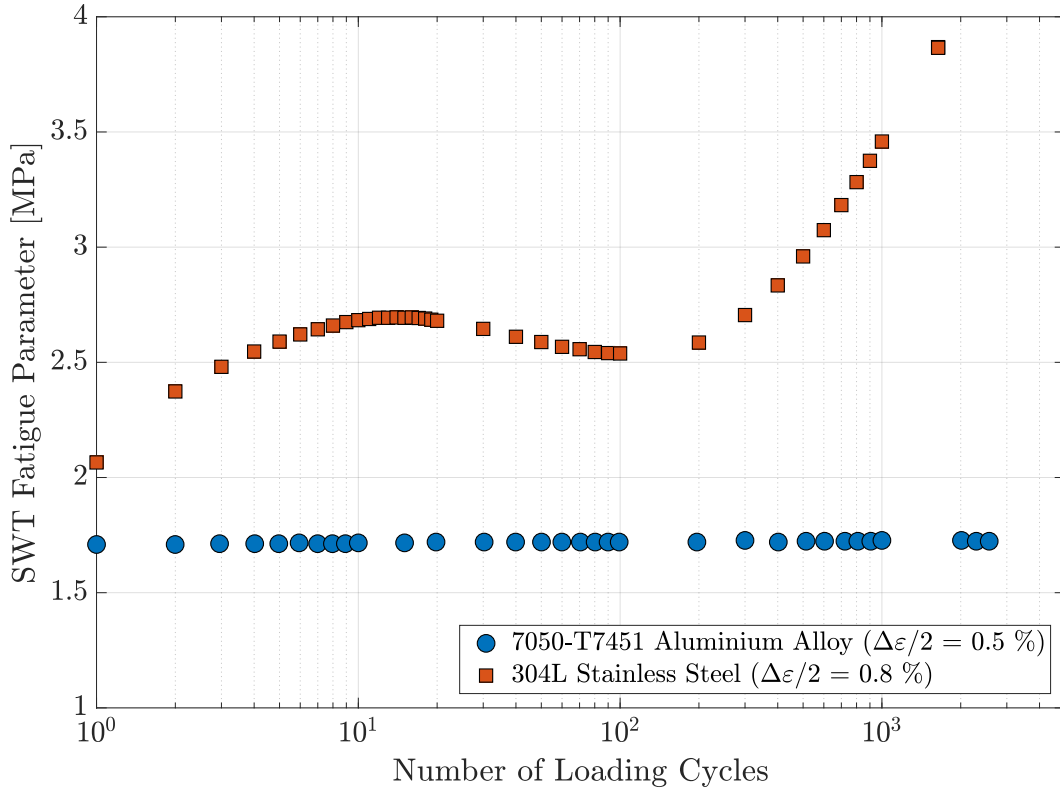


Figure 3.2: Smith–Watson–Topper fatigue parameter during fully reversed strain-controlled test for a 7050-T7451 aluminium alloy and the 304L stainless steel.

3.3 Fatigue life

In order to estimate fatigue life, the following three-parameter relationship is used:

$$(FP - FP_0)^v N_f = C. \quad (3.4)$$

This relationship has been used by some authors (Castro and Jiang, 2016; Jiang et al., 2007; Zhao and Jiang, 2008) and is similar to the one proposed by Manson (1965). In Equation 3.4, FP is the fatigue parameter, and FP_0 , v and C are material constants. The constant FP_0 may be understood as the fatigue parameter threshold below which there is no fatigue failure.

Material constants are obtained by fitting experimental data to Equation 3.4. As a single value of the fatigue parameter is used for a given test, the choice of which value *represents* an experiment may not be straightforward. For the 7050-T7451 aluminium alloy (Fig. 3.2), as the fatigue parameter almost does not vary, the half fatigue life cycle (or almost any other cycle) is representative of the experiment. On the other hand, the fatigue parameter at the half fatigue life cycle for the 304L stainless steel is somewhat different from other cycles.

One could estimate fatigue life by adopting a single value of FP or by calculating the evolution of a damage parameter throughout the loading cycles. For the latter, a damage rule must be used in order to cumulate fatigue damage. In this work, a variation of Palmgren-Miner rule will be adopted. Failure occurs when cumulative damage reaches a critical damage FD_c such that

$$FD_c = \sum_{i=1}^{N_{est}} FD_i = 1. \quad (3.5)$$

Critical damage is assumed here to be equal to one. For a load such that all cycles produce the same damage, one can calculate the damage per cycle as follows:

$$1 = N_{est}FD \Rightarrow FD = \frac{1}{N_{est}}. \quad (3.6)$$

One can estimate damage per cycle for a given FP_i from Equations 3.4 and 3.6 as follows:

$$N_{est}^i = \frac{C}{(FP_i - FP_0)^v} \Rightarrow FD_i = \frac{(FP_i - FP_0)^v}{C}. \quad (3.7)$$

Therefore,

$$1 = \sum_{i=1}^{N_{est}} \frac{(FP_i - FP_0)^v}{C}. \quad (3.8)$$

One should note that, if FP is assumed to be constant, Equations 3.4 and 3.8 coincide.

Chapter 4 – Experimental Procedures

In this work, strain-controlled fully reversed proportional axial-torsional fatigue experiments with thin-walled tubular specimens were performed at room temperature. Experiments were conducted until failure, which was defined as the appearance of a macroscopic fatigue crack, or run-out, which was defined as 10^6 cycles. Due to the rate-dependence of the cyclic stress-strain behaviour, all tests were performed with an equivalent von Mises strain rate of approximately 10^{-2} s^{-1} . After failure, macroscopic crack orientation was determined for all specimens.

4.1 Material, heat treatment and specimens

The monotonic properties of the 304L stainless steel obtained by Carneiro Junior (2017) are presented in Table 4.1:

Table 4.1: Monotonic properties of the 304L stainless steel (Carneiro Junior, 2017).

Yield stress σ_y [MPa]	Young's modulus E [GPa]	Ultimate tensile strength σ_u [MPa]	True strain at fracture ε_f [%]
213	208	616	160

The 304L stainless steel was received as extruded bars whose length and diameter were 1000 mm and 19 mm, respectively. The chemical composition of the material, obtained from the supplier, is presented in Table 4.2.

Table 4.2: Chemical composition of the 304L stainless steel, weight %

C	Mn	P	S	Si	Cr	Ni	Mo	N
0.018	1.340	0.034	0.028	0.430	18.160	8.300	0.220	0.081

In order to maintain the same conditions of the axial and torsional experiments previously performed by Carneiro Junior (2017), the same heat treatment (normalization) process was adopted. It was performed in a Nabertherm LHT 04/16 P310 furnace, which features a maximum temperature of 1600 °C, a capacity of 4 litres and a load of 5.2 kW. The bars were cut into

smaller bars, whose length was 125 mm, due to the size of the furnace. Batches of six bars were placed at the centre of the furnace upon a support, and a K-Type thermocouple, connected to a computer via a data acquisition system, was used to monitor the temperature at the vicinity of the bars. They were heated up to 1050 °C, kept at this temperature for 1 h, and cooled at room temperature. There was a discrepancy between the temperature measures of the furnace and the thermocouple. Due to the thermocouple’s location, its measure was assumed to be the correct one. Further details can be found in Carneiro Junior (2017).

The critical dimension was the outer diameter of the specimen in the grip end, which must be 15 mm due to the test machine collet grip. Hence, all other dimensions were such that the suggested dimensions presented in ASTM E2207-08 (ASTM, 2015) were respected. After the heat treatment, specimens were machined at a computer numerical controlled (CNC) lathe. The geometry and dimensions of the thin-walled tubular specimen are shown in Figure 4.1.

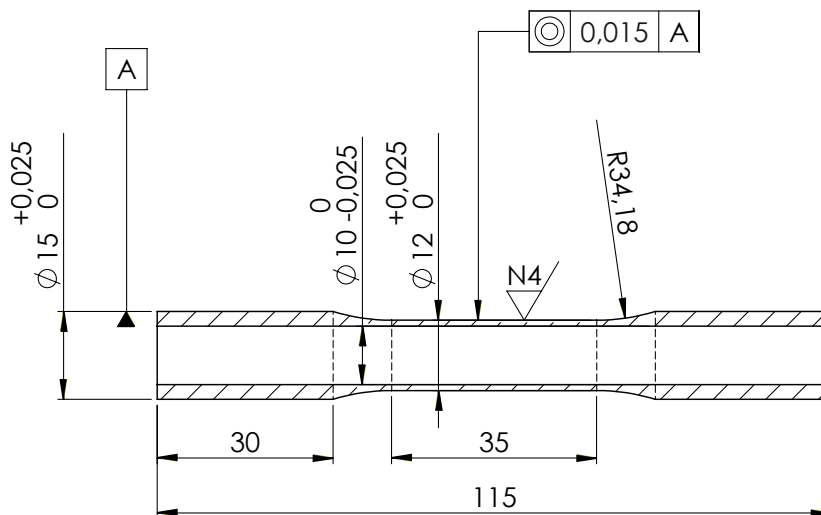


Figure 4.1: Thin-walled tubular specimens used in fatigue experiments, all dimensions in mm (Carneiro Junior, 2017).

After the machining, grinding was performed upon specimens at a mechanical lathe by using sandpapers whose grit sizes ranged from 68 μm to 8.4 μm (ISO P220-P2500). Specimens roughness parameter R_a was verified at an Olympus LEXT OLS4100 3D laser measuring microscope, whose magnification range is from 108x to 17280x, via three roughness measures performed along the specimen with a 50x objective, and an analogue and a digital surface roughness testers. All measurements coincided and were inferior to 0.2 μm , the threshold imposed by the ASTM E2207-08.

4.2 Fatigue test procedure and crack orientation

Three strain paths were investigated in this work: fully reversed axial and torsional strain-controlled tests reported earlier (Carneiro Junior, 2017), and fully reversed proportional test

whose $\lambda = (\Delta\gamma/2)/(\Delta\varepsilon/2) = \sqrt{3}$, performed in this work. Strain paths are shown in Figure 4.2.

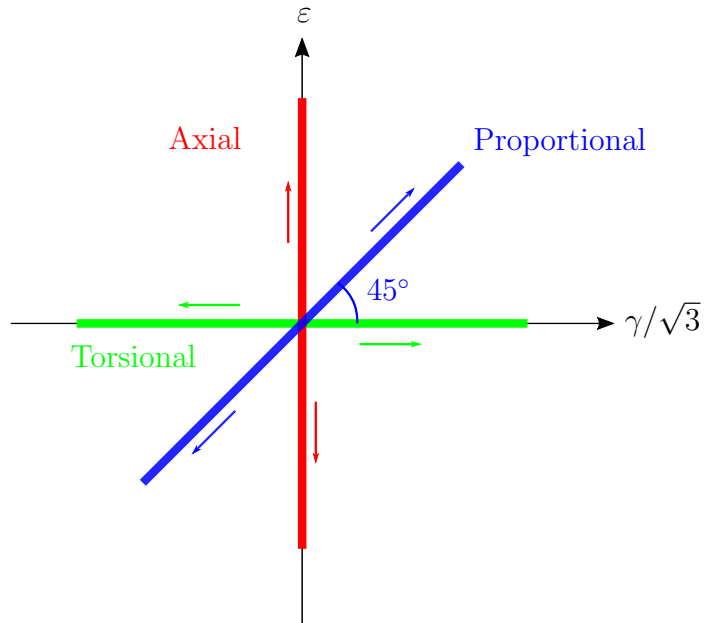


Figure 4.2: Axial-torsional strain paths.

Inner and outer diameters of the specimens were measured three times by using a digital calliper, and their mean value, adopted. The inner diameter was measured at the grip end, with a reasonable variability, whilst the outer diameter was measured at the gauge length, with a small deviation from the mean value.

In order to avoid slip of the specimens, the pressure of the hydraulic collet grip was estimated via an equation proposed by the collet manual (MTS, 2009):

$$\sigma_{collet} = 0.422 \sqrt{P^2 + \left(\frac{2T}{D_{grip}} \right)^2}, \quad (4.1)$$

in which P is the axial load in kN, T is the torque in Nm and D_{grip} is the outer diameter in the grip end **in cm**. Collet pressure varied from 10 MPa to 18 MPa for proportional experiments. It was observed a significant deformation of the specimens' grip end for a collet pressure superior to 14 MPa. To avoid this, a small cylinder was placed inside the grip end, and no significant deformation was observed for a collet pressure up to 20 MPa.

Before the beginning of the test, a verification procedure was adopted in order to verify whether the extensometer was correctly installed: first, an axial load of 2 kN, within the elastic domain, was applied; then, a torque of 8 N.m, within the elastic domain too, was applied. Both loads lasted together approximately 200 cycles. A warm-up procedure was later introduced in order to diminish the undesired effects upon hysteresis loops.

Strain-controlled fatigue procedure is described in ASTM (2015). Fatigue tests were designed by

using the MTS TestSuiteTM Multipurpose Elite. During the test, axial force and torque were monitored in order to verify whether an axial or a torsional load drop caused by the nucleation of a fatigue crack had occurred. Tests were stopped if a) a macroscopic fatigue failure had been observed by the user or b) a load drop of 4–5% had occurred. No compensator was used in the experiments. For some tests, a tapered sine wave was used in order to avoid abrupt start. Frequencies varied from 0.30 to 2.00 Hz, and no significant heating of the specimens was observed for this range of frequencies.

In this work, the crack orientation follows the convention shown in Figure 4.3. The thick black line represents the fatigue crack, the red dashed line is obtained by linking the extremities of the fatigue crack, and the solid blue is a line orthogonal to the red one. The crack orientation is the angle θ between the blue line and the specimen axis, which coincides with the direction of the axial load.

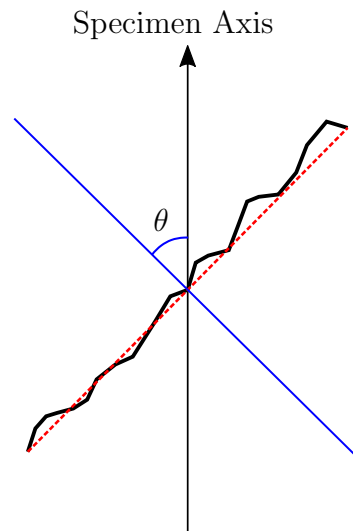


Figure 4.3: Crack orientation convention.

4.3 Equipments and softwares

All experiments were performed with an MTS 809 Axial-Torsional servo-hydraulic test system equipped of an MTS 662.20D-05 Axial-Torsional Load Transducer, whose capacity is ± 100 kN and ± 1100 Nm for axial force and torque, respectively, an MTS 646.10 Collet Grip, and an MTS FlexTest 40 controller. In order to control total strain, an MTS 632.80F-04 Axial-Torsional extensometer, whose gauge length is 25 mm, and travel is -2.0 % and +4.8 % for axial load, and $\pm 5^\circ$ for torsional angle, was used. It measures the angle of twist between the planes defining the gauge length, which is indicated by θ in ASTM E2207-08. The axial-torsional extensometer and the servo-hydraulic test system are shown in Figures 4.4 and 4.5.

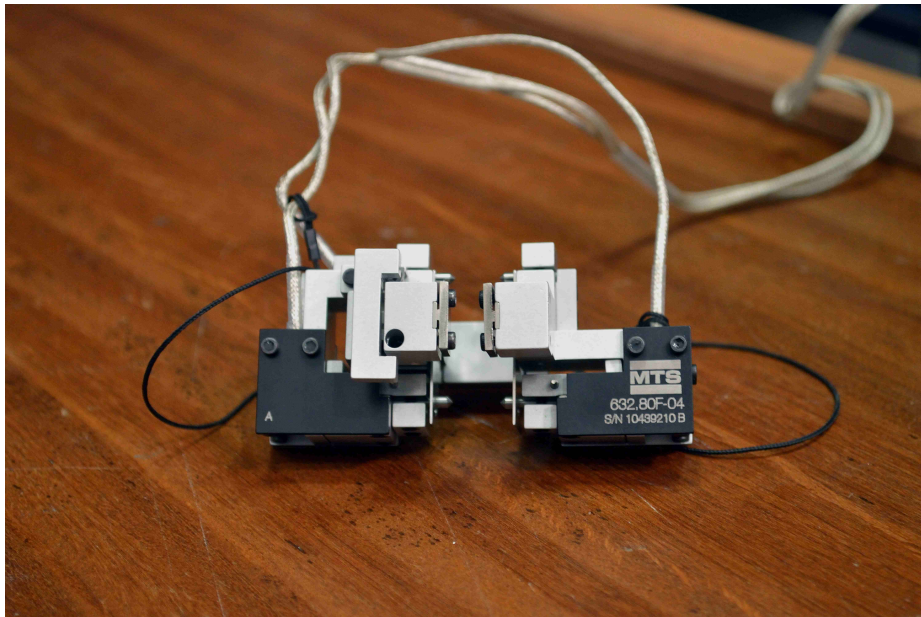


Figure 4.4: MTS 632.80F-04 axial-torsional extensometer.

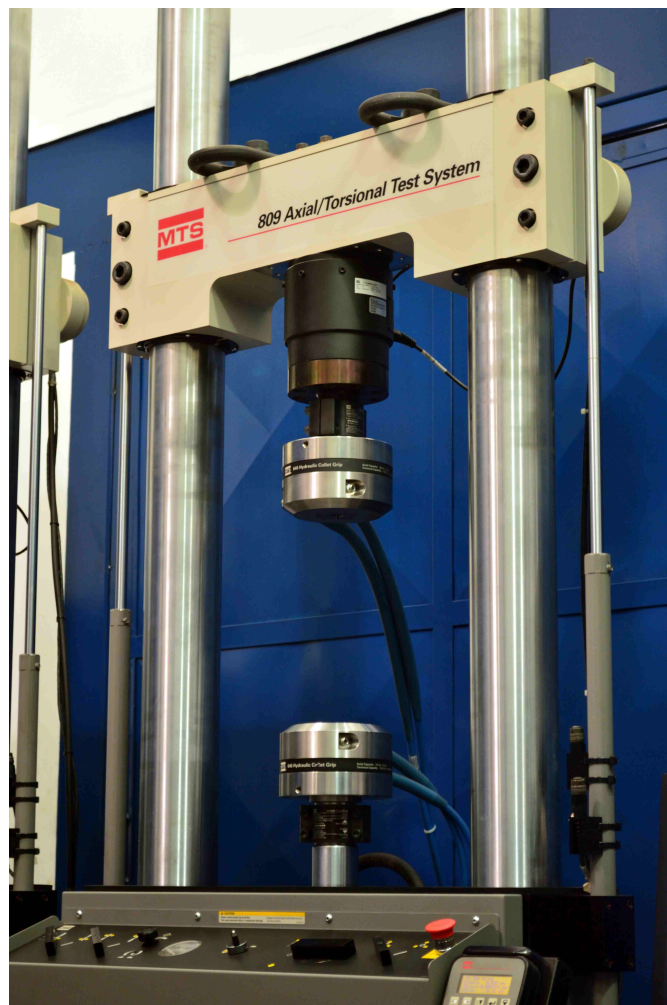


Figure 4.5: MTS 809 axial-torsional test system.

4.3.1 Experimental data post-process

In order to standardize the output of experimental data and to calculate true stresses and strains, and stress and plastic strain amplitudes based upon the definition proposed by Jiang and Kurath (1997a), a code was developed. The hypothesis of a uniform distribution of normal and shear stresses, which is a good approximation for thin-walled specimens, is assumed.

Normal stress and shear stress

The axial stress σ acting upon a thin-walled tubular specimen can be calculated from the axial force P measured by the load cell, outer diameter D and inner diameter d of the specimen as follows:

$$\sigma = \frac{4P}{\pi(D^2 - d^2)}. \quad (4.2)$$

The shear stress τ acting upon a thin-walled tubular specimen can be calculated from the torque T measured by the load cell, outer diameter D and inner diameter d of the specimen as follows:

$$\begin{aligned} T &= \int_A r\tau \, dA \\ T &= \tau \int_A r \, dA \\ T &= \tau \int_0^{2\pi} \int_{d/2}^{D/2} r \, r \, dr \, d\theta \\ T &= 2\pi\tau \left(\frac{D^3}{24} - \frac{d^3}{24} \right) \\ T &= \frac{\pi\tau(D^3 - d^3)}{12} \\ \tau &= \frac{12T}{\pi(D^3 - d^3)}. \end{aligned} \quad (4.3)$$

Note that Equation 4.3 is not the one proposed in ASTM E2207-08. Despite equally assuming a uniform shear stress distribution, it is derived from the balance between the applied torque and the shear stress distribution instead of considering the shear stress applied at the mean diameter of the cross section.

Shear strain

As reported in Section 4.3, the extensometer measures the angle of twist between the planes defining the gauge length. The shear strain γ could be calculated from diameter D , angle of

twist θ_{Twist} in radians, and the gauge length L as follows:

$$\gamma = \frac{D\theta_{Twist}}{2L}. \quad (4.4)$$

Equation 4.4 could be used to calculate shear strains at any material point of the specimen. As fatigue crack nucleation usually occurs at the surface (Socie and Marquis, 1997), surface shear strain γ^{sur} is more suitable for fatigue analysis. Nonetheless, the shear strain at the middle of the specimens' wall γ^{mid} was controlled all experiments performed by Carneiro Junior (2017), whilst the surface one was controlled upon proportional experiments. The ratio between surface and middle shear stress for the specimen shown in Figure 4.1 is approximately equal to 1.09.

True stress and true strain

In order to calculate the instant outer and inner diameter of the specimen, it was assumed that transversal strain could be calculated as¹

$$\varepsilon_{true}^{transversal} = -\nu_{el}\varepsilon_{true}^e - \nu_{pl}\varepsilon_{true}^p. \quad (4.5)$$

Based upon the aforementioned equations, a program to calculate true stresses and strains was developed.

Equivalent stress and plastic strain amplitudes

Stress amplitude measures are usually based upon the equivalent measures (Jiang and Kurath, 1997a), as the equivalent von Mises stress

$$\sigma_{eq}(t) = \sqrt{\frac{3}{2}}\|\mathbf{S}(t)\| \quad (4.6)$$

and the equivalent von Mises plastic strain

$$\varepsilon_{eq}^p(t) = \sqrt{\frac{2}{3}}\|\boldsymbol{\varepsilon}^p(t)\|. \quad (4.7)$$

For an axial-torsional stress state,

$$\boldsymbol{\sigma}(t) = \begin{bmatrix} \sigma(t) & \tau(t) & 0 \\ \tau(t) & 0 & 0 \\ 0 & 0 & 0 \end{bmatrix}. \quad (4.8)$$

¹It is assumed the plastic strain incompressibility, which implies $\nu_{pl} = 1/2$.

The deviatoric stress tensor \mathbf{S} can be calculated as

$$\mathbf{S}(t) = \begin{bmatrix} \frac{2}{3}\sigma(t) & \tau(t) & 0 \\ \tau(t) & -\frac{1}{3}\sigma(t) & 0 \\ 0 & 0 & -\frac{1}{3}\sigma(t) \end{bmatrix} \quad (4.9)$$

and the plastic strain tensor $\boldsymbol{\varepsilon}^p$ as

$$\boldsymbol{\varepsilon}^p(t) = \begin{bmatrix} \varepsilon^p(t) & \frac{\gamma^p}{2}(t) & 0 \\ \frac{\gamma^p}{2}(t) & -\frac{1}{2}\varepsilon^p(t) & 0 \\ 0 & 0 & -\frac{1}{2}\varepsilon^p(t) \end{bmatrix}. \quad (4.10)$$

The equivalent von Mises stress can be calculated as

$$\sigma_{eq}(t) = \sqrt{\sigma^2(t) + 3\tau^2(t)}. \quad (4.11)$$

For a proportional load, stress amplitude can be defined as

$$\frac{\Delta\sigma_{eq}}{2} = \sqrt{\left(\frac{\Delta\sigma}{2}\right)^2 + 3\left(\frac{\Delta\tau}{2}\right)^2}. \quad (4.12)$$

The equivalent von Mises plastic strain amplitude can be calculate from the plastic strain tensor as

$$\varepsilon_{eq}^p(t) = \sqrt{[\varepsilon^p(t)]^2 + \frac{1}{3}[\gamma^p(t)]^2}. \quad (4.13)$$

For a proportional load, plastic strain amplitude can be defined as

$$\frac{\Delta\varepsilon_{eq}^p}{2} = \sqrt{\left(\frac{\Delta\varepsilon^p}{2}\right)^2 + \frac{1}{3}\left(\frac{\Delta\gamma^p}{2}\right)^2}. \quad (4.14)$$

For non-proportional loads, Jiang and Kurath (1997a) proposed as a measure of both stress and plastic strain amplitudes the radii of the minimum circles that circumscribe the loading paths. Mathematically,

$$\bar{\sigma}_a = \frac{\Delta\sigma_{eq}}{2} = \text{Min}_{\mathbf{S}_0} \left\{ \text{Max}_t \left\{ \sqrt{\frac{3}{2}} \|\mathbf{S}(t) - \mathbf{S}_0\| \right\} \right\}, \quad (4.15a)$$

$$\bar{\varepsilon}_a^p = \frac{\Delta\varepsilon_{eq}^p}{2} = \text{Min}_{\boldsymbol{\varepsilon}_0^p} \left\{ \text{Max}_t \left\{ \sqrt{\frac{2}{3}} \|\boldsymbol{\varepsilon}^p(t) - \boldsymbol{\varepsilon}_0^p\| \right\} \right\}. \quad (4.15b)$$

For proportional axial-torsional loads, Equations 4.12, 4.14 and 4.15 coincide. It is shown in Figure 4.6 an illustration of the proposed measures.

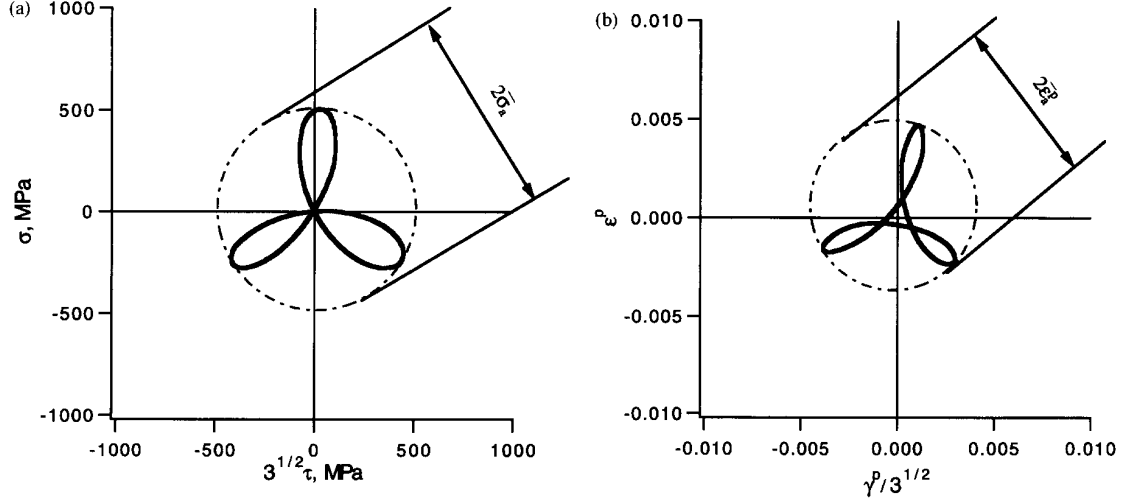


Figure 4.6: Proposed amplitude measures for (a) stress and (b) plastic strain amplitude for a non-proportional loading path (Jiang and Kurath, 1997a).

In order to calculate the stress and plastic strain amplitudes, an incremental algorithm proposed by Dang Van et al. (1989), whose computational cost is very attractive (Bernasconi and Papadopoulos, 2005), is used.

4.4 Rate-dependence and fatigue test design

As mentioned in Section 2.3.1, the cyclic stress-strain behaviour of the 304L stainless steel depends upon the strain rate. Therefore, in order to all tests be performed under the same conditions, frequencies were such that the equivalent von Mises strain rate was close to 10^{-2} s^{-1} , the strain rate used by Carneiro Junior (2017). The von Mises equivalent strain can be calculated as

$$\varepsilon_{eq}(t) = \sqrt{\frac{2}{3}} \|\boldsymbol{\varepsilon}(t)\| = \sqrt{\frac{2}{3}} \|\boldsymbol{\varepsilon}^e(t) + \boldsymbol{\varepsilon}^p(t)\|. \quad (4.16)$$

Assuming that $\boldsymbol{\varepsilon}^p \gg \boldsymbol{\varepsilon}^e$,

$$\varepsilon_{eq}(t) = \sqrt{\frac{2}{3}} \|\boldsymbol{\varepsilon}^p(t)\| = \sqrt{\varepsilon^2(t) + \frac{\gamma^2(t)}{3}}. \quad (4.17)$$

Tests will be performed with a constant ratio between shear strain amplitude $\Delta\gamma/2$ and axial strain amplitudes $\Delta\varepsilon/2$ of $\sqrt{3}$. Therefore,

$$\frac{\Delta \varepsilon_{eq}}{2} = \sqrt{\left(\frac{\Delta \varepsilon}{2}\right)^2 + \left(\frac{1}{\sqrt{3}} \frac{\Delta \gamma}{2}\right)^2} = \sqrt{\frac{\Delta \varepsilon^2}{2} + \frac{\Delta \varepsilon^2}{2}} = \sqrt{2} \frac{\Delta \varepsilon}{2}. \quad (4.18)$$

Axial and shear strain amplitudes can be calculated by using Equation 4.18:

$$\frac{\Delta \varepsilon}{2} = \frac{\sqrt{2}}{2} \frac{\Delta \varepsilon_{eq}}{2} \quad (4.19a)$$

$$\frac{\Delta \gamma}{2} = \sqrt{3} \left(\frac{\sqrt{2}}{2} \frac{\Delta \varepsilon_{eq}}{2} \right) = \sqrt{\frac{3}{2}} \frac{\Delta \varepsilon_{eq}}{2}. \quad (4.19b)$$

For a sinusoidal load, axial and shear strain can be calculated for a given instant t , angular frequency ω and phase angle ϕ as follows:

$$\varepsilon(t) = \frac{\Delta \varepsilon}{2} \sin(\omega t), \quad (4.20a)$$

$$\gamma(t) = \frac{\Delta \gamma}{2} \sin(\omega t + \phi). \quad (4.20b)$$

The equivalent strain at a given instant can be calculated as follows:

$$\begin{aligned} \varepsilon_{eq}(t) &= \sqrt{\left[\frac{\Delta \varepsilon}{2} \sin(\omega t)\right]^2 + \frac{1}{3} \left[\frac{\Delta \gamma}{2} \sin(\omega t + \phi)\right]^2} \\ \varepsilon_{eq}(t) &= \sqrt{\left[\frac{\Delta \varepsilon}{2} \sin(\omega t)\right]^2 + \left[\frac{1}{\sqrt{3}} \frac{\Delta \gamma}{2} \sin(\omega t + \phi)\right]^2} \\ \varepsilon_{eq}(t) &= \sqrt{\left[\frac{\Delta \varepsilon}{2} \sin(\omega t)\right]^2 + \left[\frac{\Delta \varepsilon}{2} \sin(\omega t + \phi)\right]^2} \\ \varepsilon_{eq}(t) &= \frac{\Delta \varepsilon}{2} \sqrt{\sin^2(\omega t) + \sin^2(\omega t + \phi)}. \end{aligned} \quad (4.21)$$

For a proportional test,

$$\varepsilon_{eq}(t) = \frac{\Delta \varepsilon}{2} \sqrt{2} |\sin(\omega t)|. \quad (4.22)$$

Hence, the equivalent strain rate can be calculated as follows:

$$\dot{\varepsilon}_{eq}(t) = \frac{\Delta \varepsilon}{2} \sqrt{2} \omega \operatorname{sign}[\sin(\omega t)] \cos(\omega t). \quad (4.23)$$

Since the strain rate is not constant, it will be assumed for calculations that strain rate is equal

to its maximum value. Therefore,

$$\dot{\epsilon}_{eq} = \frac{\Delta\epsilon}{2}\sqrt{2\omega}. \quad (4.24)$$

One can calculate strain rate as a function of temporal frequency $f = \omega/2\pi$ as follows:

$$\dot{\epsilon}_{eq} = \frac{\Delta\epsilon}{2}\sqrt{2\omega} = \frac{\Delta\epsilon}{2}\sqrt{2\omega}2\pi f \Rightarrow \dot{\epsilon}_{eq} = 2\sqrt{2\pi}\frac{\Delta\epsilon}{2}f. \quad (4.25)$$

Chapter 5 – Results and Discussions

5.1 Fatigue life

For all the analysis presented in this chapter, true stresses and strains were used. A summary of fatigue experiments is presented in Table 5.1. The stress values listed were taken from the cycle that corresponds to the half fatigue life. The equivalent strain amplitude, defined in Section 4.3.1, vs. the number of cycles to failure for the axial, torsional and proportional experiments, and the fit $(\Delta\varepsilon_{eq}/2 - \varepsilon_0)^y N_f = C$ for the three strain paths are shown in Figure 5.1.

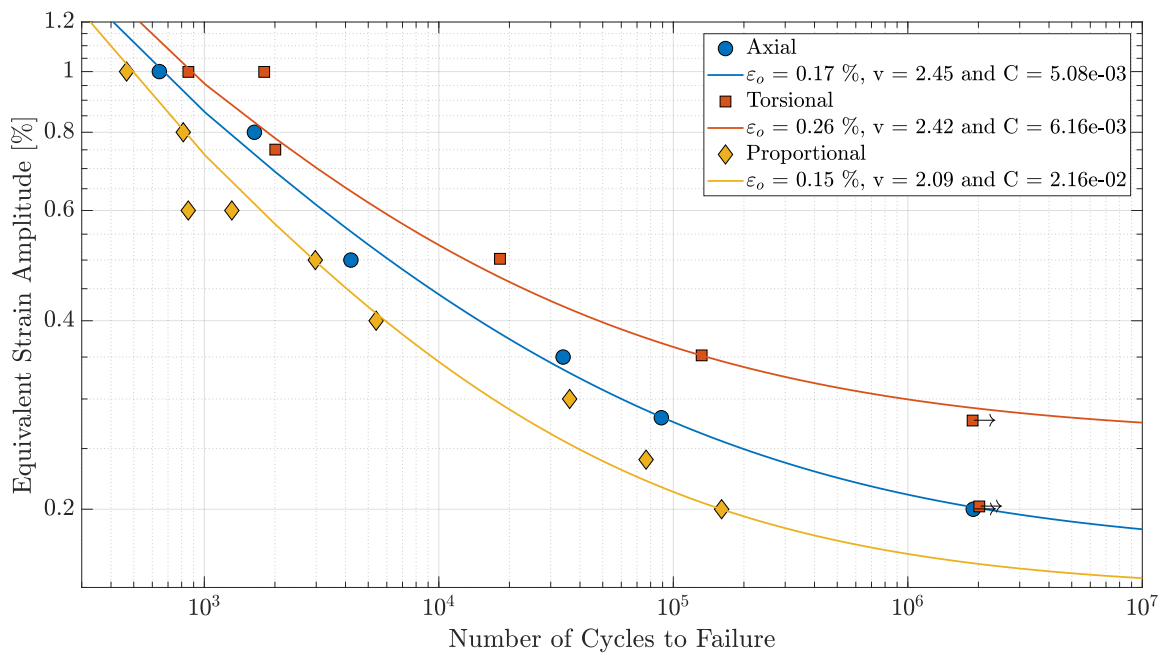


Figure 5.1: Equivalent strain amplitude vs. fatigue life for axial, torsional and axial-torsional proportional loading.

Based upon the results shown in Figure 5.1, fatigue life cannot be predicted by using the same equivalent strain amplitude for the three strain paths since torsional experiments last longer than axial experiments, which last longer than proportional ones for the same prescribed equivalent strain amplitude.

Table 5.1: Fatigue test data for the 304L stainless steel.

Strain Path	Specimen ID	$\Delta\varepsilon_{eq}/2$ [%] ^a	$\Delta\varepsilon/2$ [%]	$\Delta\gamma/2$ [%] ^a	$\Delta\sigma/2$ [MPa] ^b	σ_m [MPa] ^b	$\Delta\tau/2$ [MPa] ^b	τ_m [MPa] ^b	θ [°]	f [Hz]	N_f [Cycles]
Axial ^c	UN14	1.00	1.00	-	377	-6	-	-	-5	0.15	643
	UN19	0.80	0.80	-	320	-5	-	-	- ^d	0.18	1,635
	UN06	0.50	0.50	-	261	-1	-	-	0	0.50	4,218
	UN17	0.35	0.35	-	203	-4	-	-	0	1.40	33,880
	UN24	0.28	0.28	-	200	-1	-	-	0	2.00	88,900
	UN12	0.20	0.20	-	176	-11	-	-	-	7.00	>1,901,074
Torsional ^c	TU20	1.00	-	1.73	-	-	225	0	0	0.15	855
	TU29	1.00	-	1.73	-	-	256	0	0	0.15	1,800
	TU26	0.75	-	1.30	-	-	192	1	0	0.30	2,007
	TU21	0.50	-	0.87	-	-	207	0	0	0.50	18,230
	TU23	0.35	-	0.61	-	-	155	0	45	1.40	132,071
	TU28	0.28	-	0.48	-	-	173	0	-	2.00	>1,889,057
	TU22	0.20	-	0.35	-	-	129	-3	-	2.00	>2,017,640
Proportional	TU40	1.00	0.71	1.22	304	-8	128	2	0	0.30	461
	TU37	0.80	0.57	0.98	266	-7	112	2	10	0.40	780
	TU33	0.60	0.42	0.73	235	-6	99	2	0	0.60	830
	TU41	0.60	0.42	0.73	234	-7	97	2	0	0.60	1,200
	TU32	0.50	0.35	0.61	209	-9	90	2	5	0.80	2,000
	TU35	0.40	0.28	0.49	197	-8	85	3	0	1.00	5,100
	TU36	0.30	0.21	0.37	186	-13	80	1	20	1.20	35,000
	TU42	0.24	0.17	0.29	180	-19	78	3	30	1.75	70,000
	TU38	0.20	0.14	0.24	156	-23	74	2	35	2.00	148,700

^a Middle section shear strain for torsional, and surface shear strain for proportional.

^b Obtained from the hysteresis loop at half fatigue life.

^c Data taken from Carneiro Junior (2017).

^d Failure outside the gauge section.

5.2 Cyclic stress-strain behaviour

In this section, the secondary hardening, the Masing behaviour and the proportionality upon the plastic strain and deviatoric stress spaces will be analysed.

5.2.1 Secondary hardening

The evolution of the equivalent stress amplitude throughout the loading cycles for axial, torsional and proportional axial-torsional loading conditions is shown in Figure 5.2. There was secondary hardening upon all axial and torsional experiments, including those in which specimens did not fail ($\Delta\varepsilon_{eq}/2 = 0.20\%$ for axial, and $\Delta\varepsilon_{eq}/2 = 0.20\%$ and $\Delta\varepsilon_{eq}/2 = 0.28\%$ for torsional loading). On the other hand, secondary hardening was observed only for proportional experiments whose $\Delta\varepsilon_{eq}/2 \geq 0.80\%$.

In order to investigate whether the evolution of secondary hardening throughout the loading cycles was similar for the three strain histories, the equivalent stress amplitude vs. the percentage of fatigue life for axial, torsional and proportional axial-torsional loading conditions is shown in Figure 5.3, in which the arrow denotes run-out, and the cross denotes fatigue failure. The maximum softening, assumed to be the initiation of the secondary hardening, occurred before $0.2N_f$ for all experiments in which secondary hardening was very pronounced (all torsional experiments and axial experiments whose $\Delta\varepsilon_{eq}/2 = 0.20, 0.80$ and 1.00%). Therefore, any analysis that considers the stabilized cycle as the half fatigue life will include the effects of secondary hardening. This may be incoherent since there may be no secondary hardening at all for a range of strain amplitudes, as discussed in Section 2.1.

To investigate whether the evolution of stress amplitude was different for proportional loading, it is shown in Figure 5.4 a comparison between the evolution of stress amplitude for axial, torsional and proportional experiments whose $\Delta\varepsilon_{eq}/2 = 0.20\%$ and $\Delta\varepsilon_{eq}/2 = 1.00\%$. It may be argued that secondary hardening was not significant for some strain amplitudes because fatigue failure occurs before it becomes important, similarly to both torsional experiments whose $\Delta\varepsilon_{eq}/2 = 1.00\%$, in which there was additional hardening for the one which lasted the most. This may sustain the hypothesis that secondary hardening occurs if a cumulative threshold value of a given variable is achieved, not if the strain amplitude is greater than a plastic or a total strain amplitude threshold.

It was also investigated whether the secondary hardening affects axial and shear stresses equally for proportional loading. Axial and shear stresses normalized by the maximum axial or shear stress amplitude vs. the percentage of fatigue life for the two proportional experiments that exhibited secondary hardening are shown in Figure 5.5. It was observed that the increase upon axial and torsional stresses is qualitatively similar, but it occurs later for the shear than for the axial stress for both strain amplitudes.

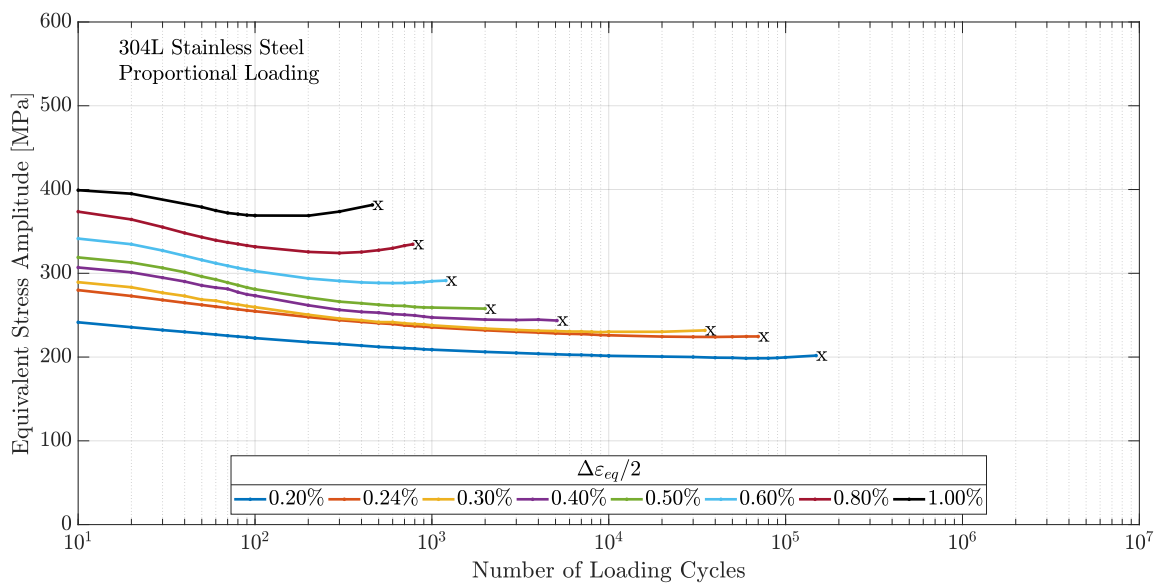
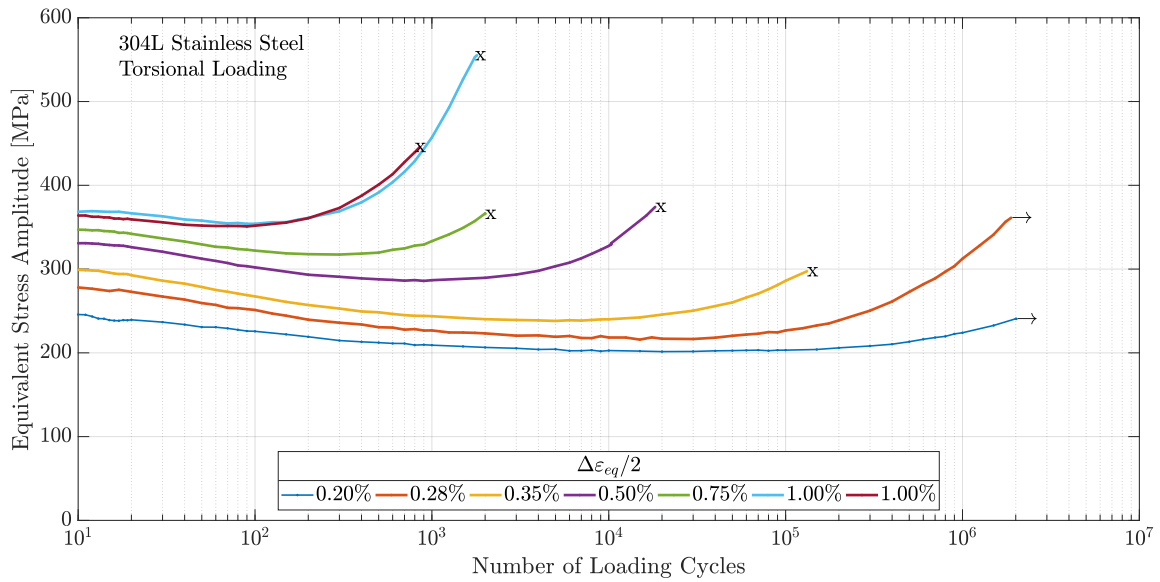
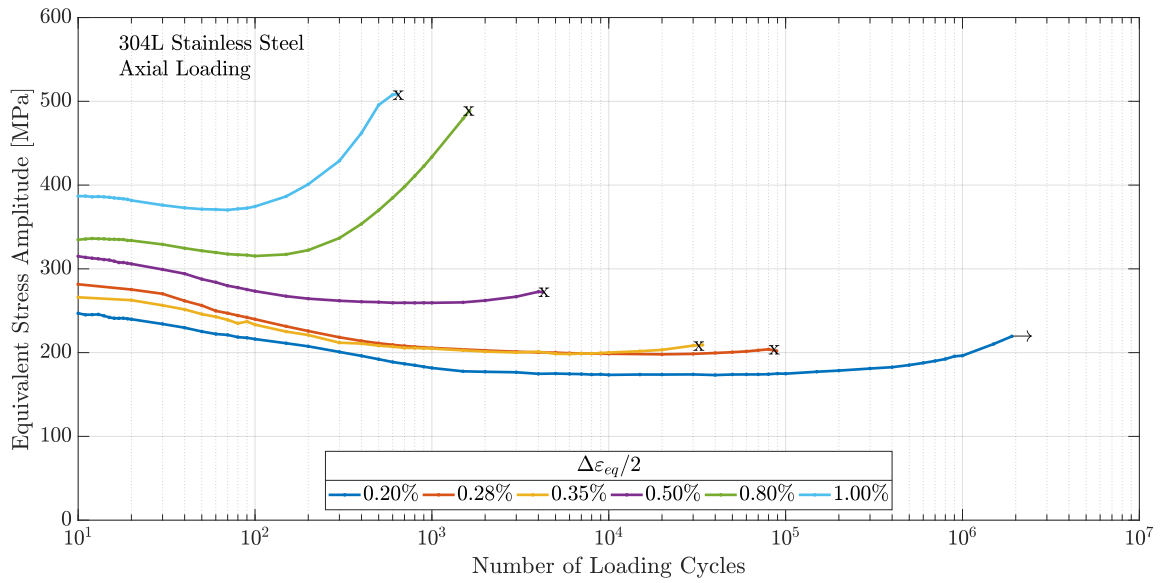


Figure 5.2: Equivalent stress amplitude vs. number of loading cycles for strain-controlled axial, torsional and proportional loading.

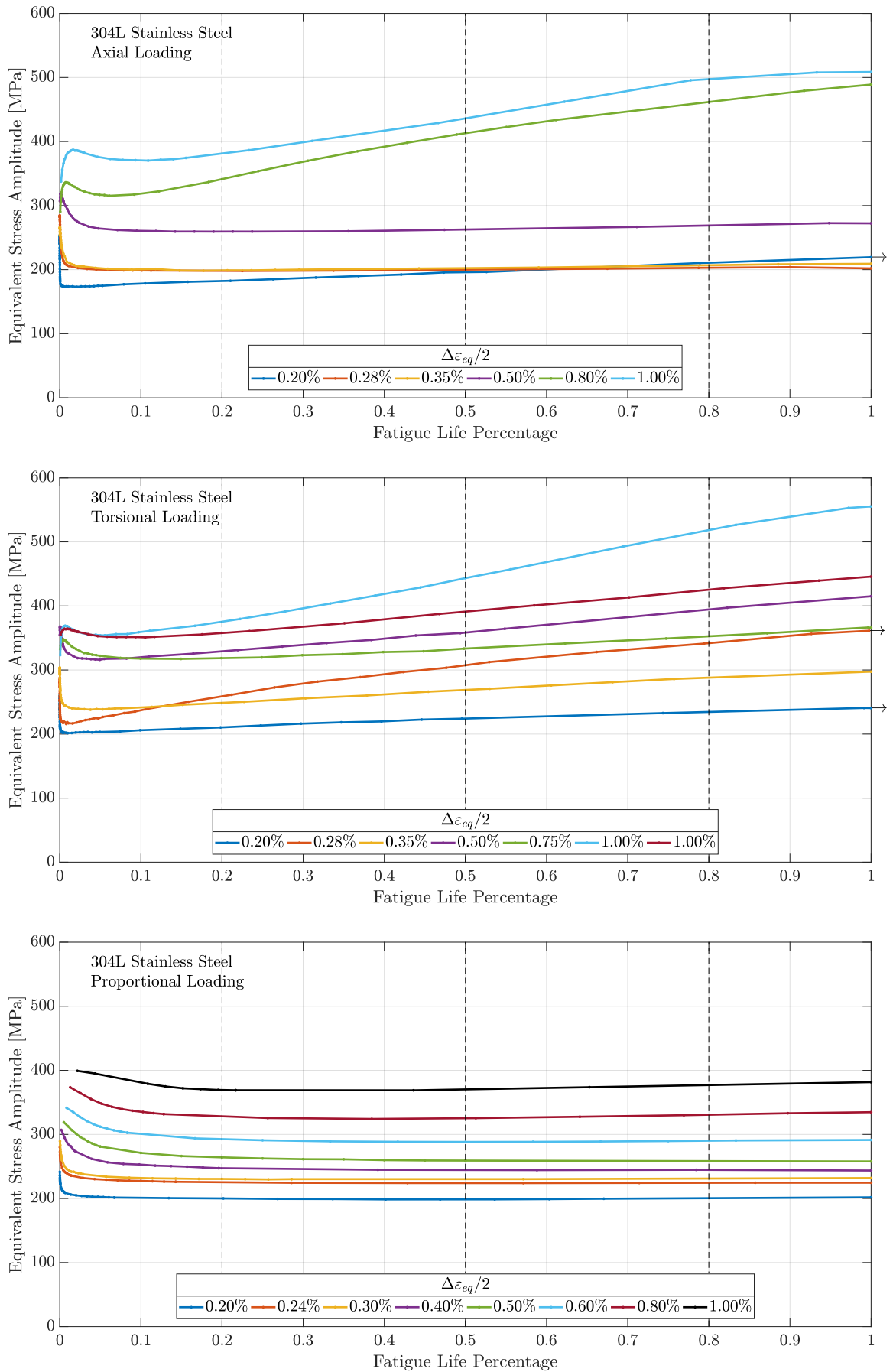


Figure 5.3: Equivalent stress amplitude vs. fatigue life percentage for strain-controlled axial, torsional and proportional loading.

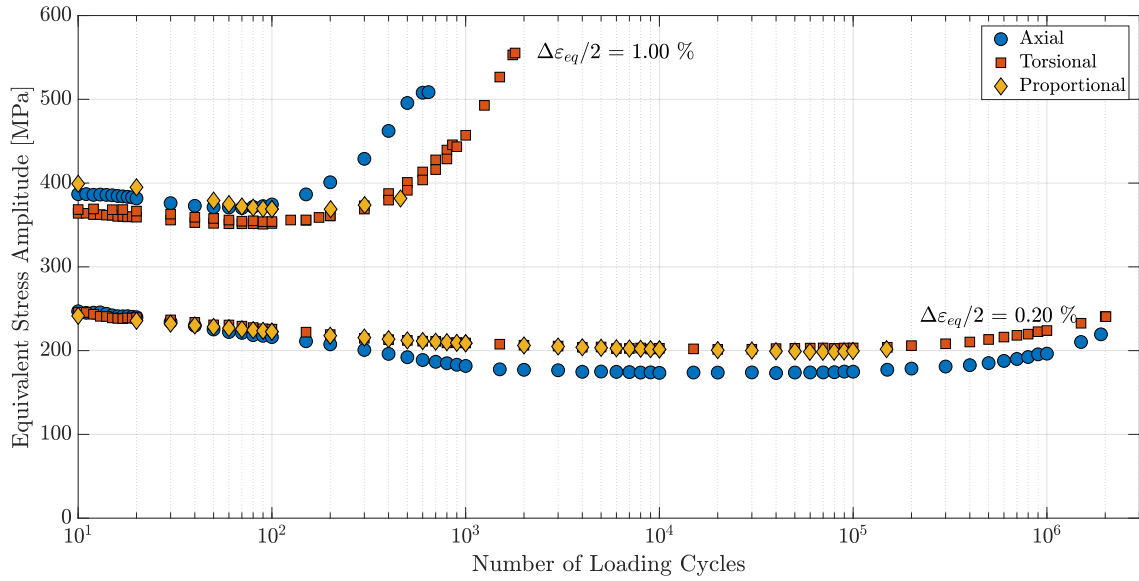


Figure 5.4: Equivalent stress amplitude vs. number of loading cycles for $\Delta\varepsilon_{eq}/2 = 0.20\%$ and $\Delta\varepsilon_{eq}/2 = 1.00\%$.

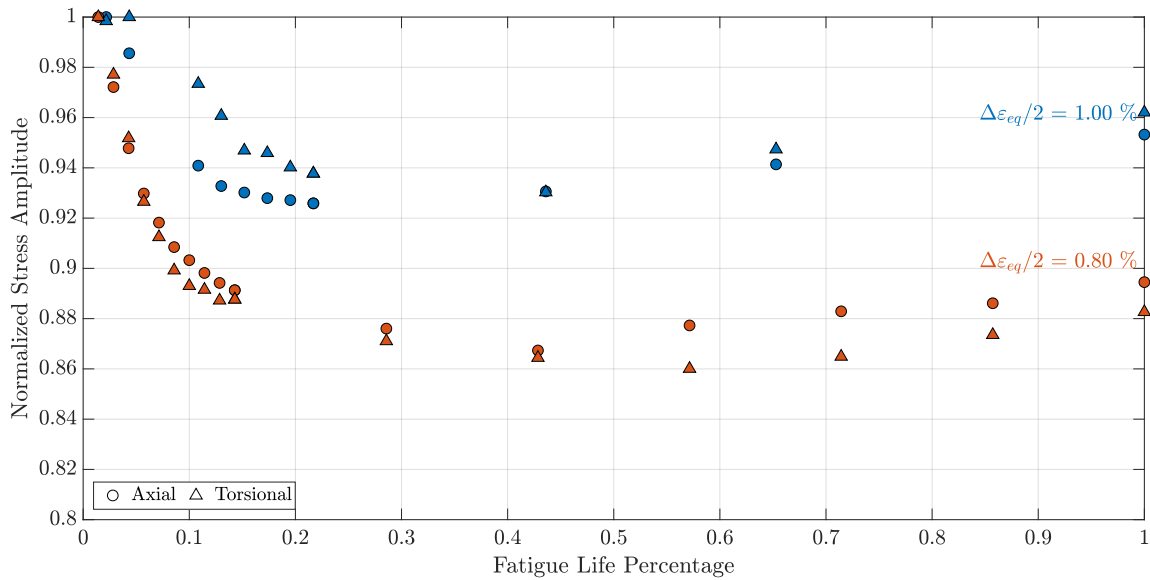


Figure 5.5: Normalized stress amplitude vs. fatigue life percentage for proportional experiments whose $\Delta\varepsilon_{eq}/2 = 0.80\%$ and $\Delta\varepsilon_{eq}/2 = 1.00\%$.

5.2.2 Masing behaviour

Carneiro Junior (2017) observed that the 304L does not exhibit a Masing-type behaviour for the investigated range of equivalent strain amplitudes (0.2–1.0 %). The plastic equivalent strain range vs. the equivalent stress range for axial, torsional and proportional loading is shown in Figures 5.6 and 5.9. Loops were obtained from the maximum softening cycle to minimize the influence of the secondary hardening.

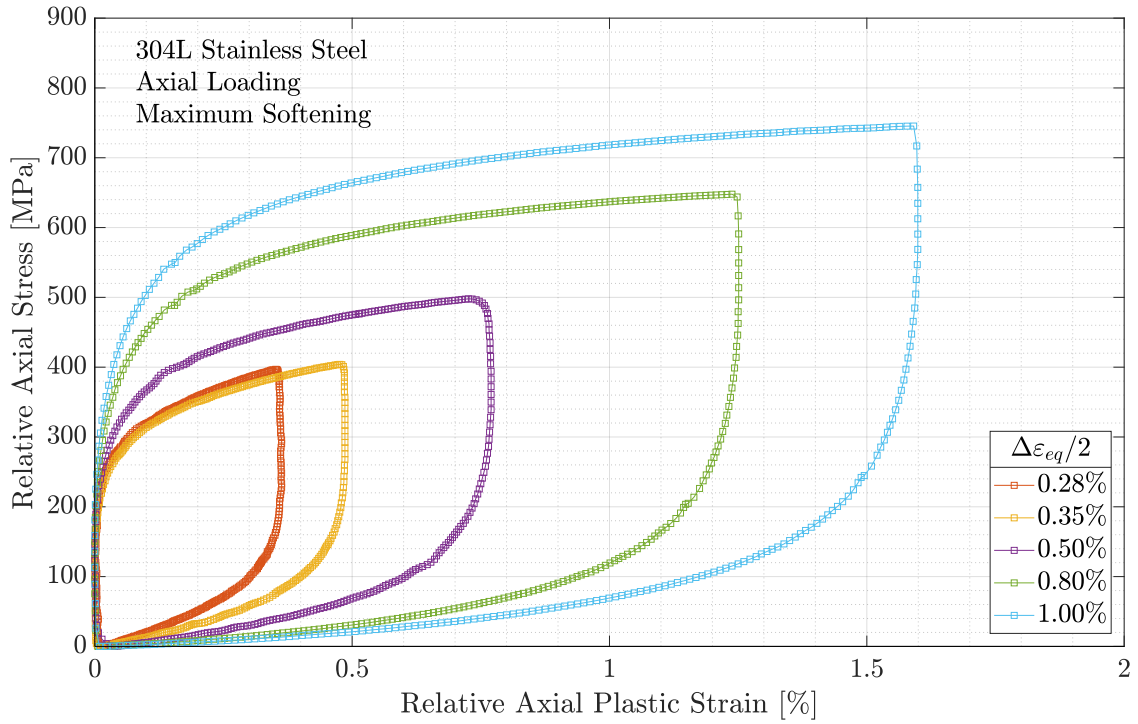


Figure 5.6: Axial stress range vs. axial plastic strain range for axial loading.

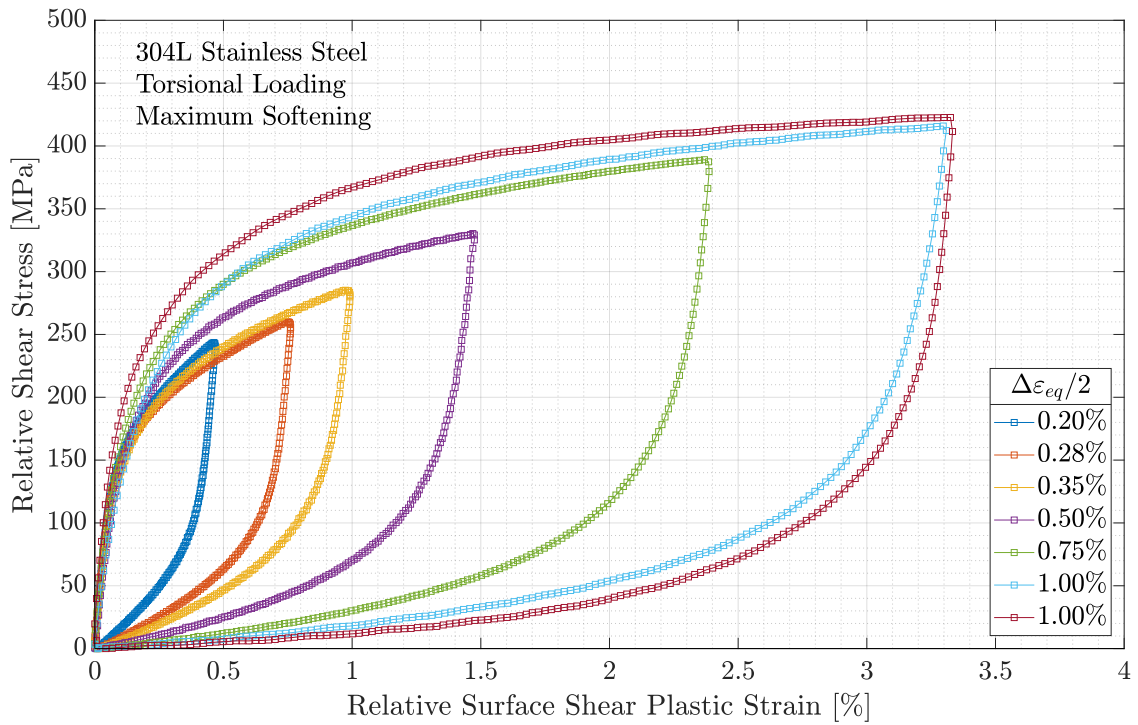


Figure 5.7: Shear stress range vs. plastic shear strain range for torsional loading.

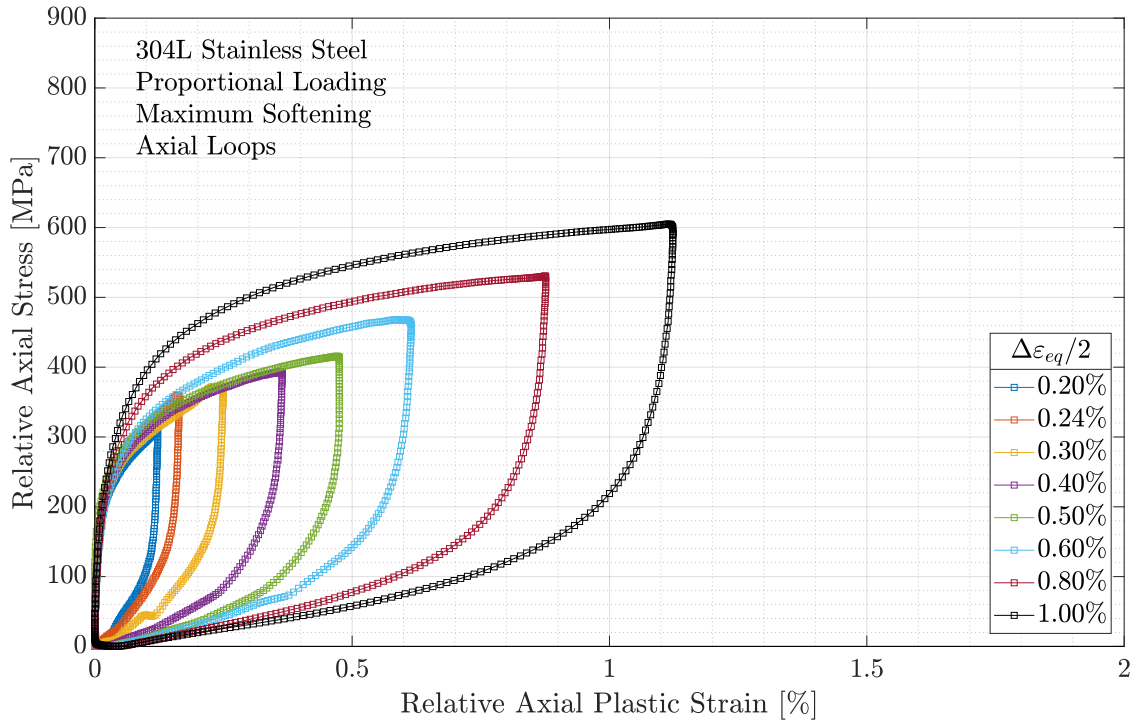


Figure 5.8: Axial stress range vs. axial plastic strain range for proportional loading.

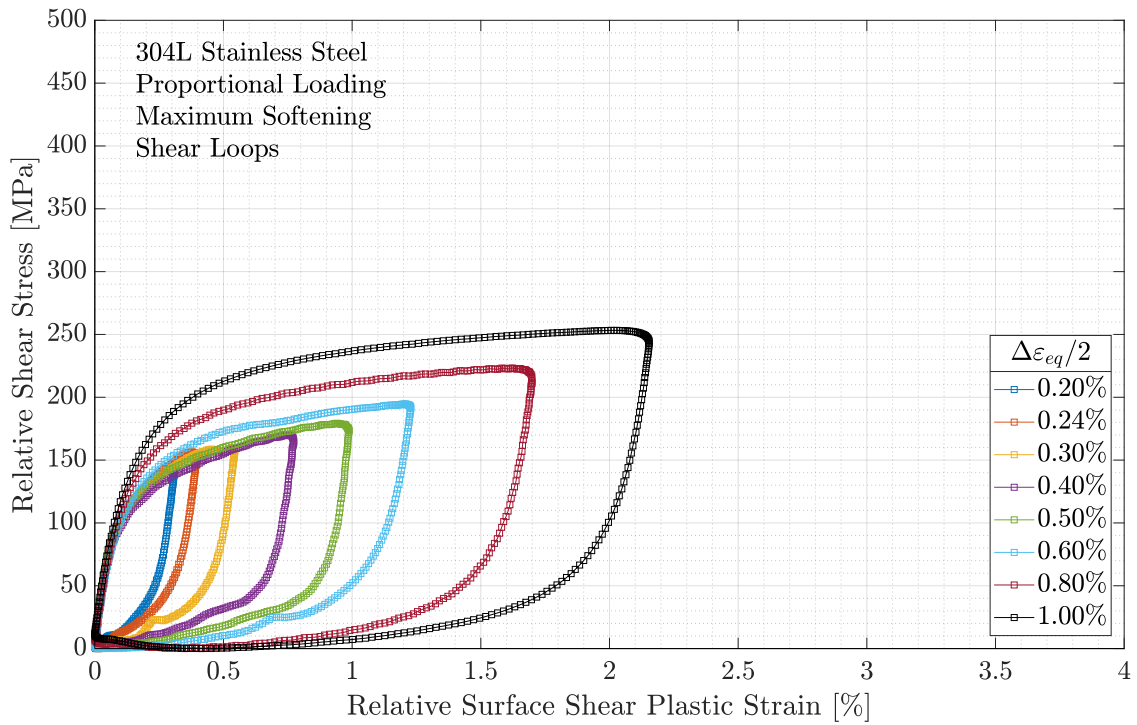


Figure 5.9: Shear stress range vs. plastic shear strain range for proportional loading.

Loops from axial and proportional experiments whose axial strain amplitude $\Delta\epsilon/2 < 0.40\%$ were geometrically similar, as shown in Figure 5.10. On the other hand, there was no similarity between

torsional and proportional loading for a range of equivalent strain amplitudes $\Delta\varepsilon_{eq}/2 = 0.30\text{--}0.50\%$, as shown in Figure 5.11.

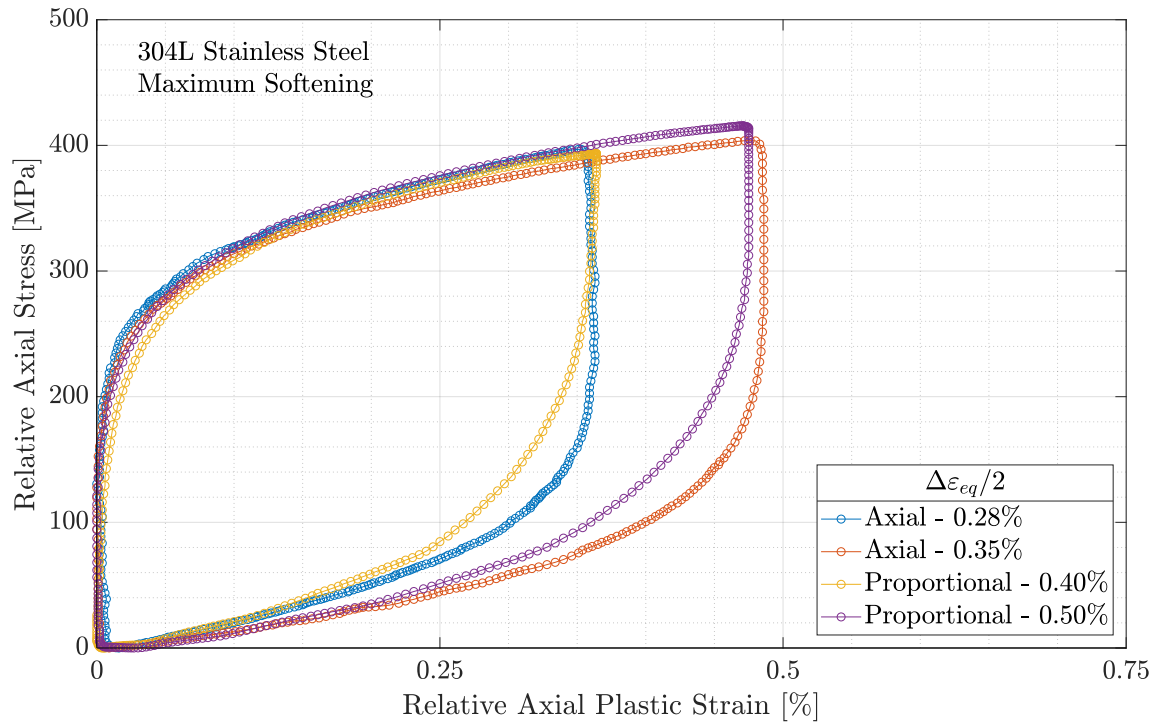


Figure 5.10: Axial stress range vs. axial plastic strain range for axial and proportional loading for selected amplitudes.

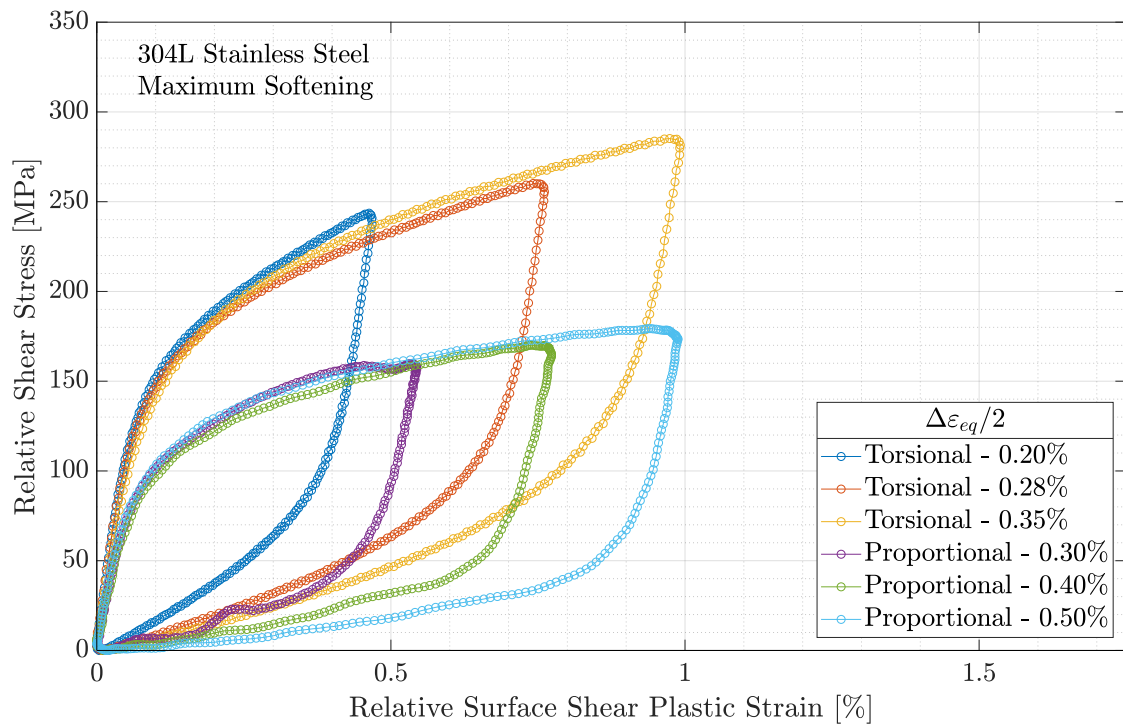


Figure 5.11: Axial stress range vs. axial plastic strain range for axial and proportional loading for selected amplitudes.

Note that the 304L stainless steel exhibits a Masing behaviour for plastic axial and shear strain range for axial, torsional and proportional loading. For axial loading, it occurs for $\Delta\varepsilon^p \leq 0.5\%$, similar to proportional experiments. This coincidence is also observed upon shear loops of torsional and proportional experiments such that $\Delta\gamma^p \leq 1.0\%$. Therefore, it may be argued that the deviation from the Masing behaviour occurs if the plastic axial or shear strain range is greater than an axial or a torsional amplitude threshold. The equivalent von Mises strain amplitude cannot be used as a threshold parameter since for $\Delta\varepsilon_{eq}/2 = 0.50\%$ the material exhibits a Masing-type behaviour for the proportional experiment, whilst this is not observed for the axial one.

5.2.3 Proportionality

The definition of proportional loading may be based upon total strain, plastic strain or deviatoric stress spaces (Jiang and Kurath, 1997a). Non-proportional hardening parameters are usually related to stress and plastic strain measures, which may yield some inconsistent results since there may be some loading proportional upon the total strain space and non-proportional on the plastic strain and deviatoric stress space. From a mathematical point of view, a proportional loading can be defined as a loading such that

$$\mathbf{A}(t) = \mathbf{A}_o \varpi(t), \quad (5.1)$$

in which $\varpi(t)$ is a given function of t . As a consequence, the eigenvectors of \mathbf{A} are the same for all time instants. From a solid mechanics point of view, it means that principal stresses or strains, depending upon which tensor is used to define proportionality, occur at the same material plane for all time instants. The strain tensor components for a proportional loading can be written as

$$\varepsilon(t) = \frac{\Delta\varepsilon}{2} \varpi(t), \quad (5.2a)$$

$$\gamma(t) = \frac{\Delta\gamma}{2} \varpi(t). \quad (5.2b)$$

The ratio between those components is

$$\frac{\varepsilon(t)}{\gamma(t)} = \frac{\Delta\varepsilon/2}{\Delta\gamma/2} \Rightarrow \varepsilon(t) = \frac{1}{\sqrt{3}} \gamma(t) = \frac{\lambda}{\sqrt{3}} \varepsilon(t), \quad (5.3)$$

which is the parametric equation of a straight line whose slope angle is $\arctan(\lambda/\sqrt{3})$ upon an orthonormal coordinate system whose base is $[\varepsilon \vec{e}_1, (\gamma/\sqrt{3}) \vec{e}_2]$.

For strain-controlled experiments, as those performed upon this work, proportionality is usually defined for the total strain tensor. The total strain, the plastic strain and the stress paths of some proportional experiments obtained at maximum softening, in order to minimize the

influence of secondary hardening, are shown in Figures 5.12–5.14.

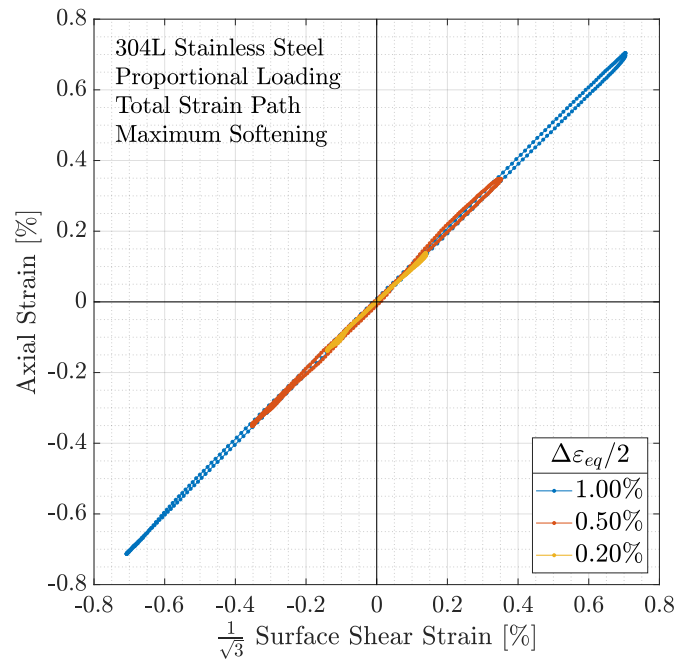


Figure 5.12: Total strain paths for selected proportional experiments.

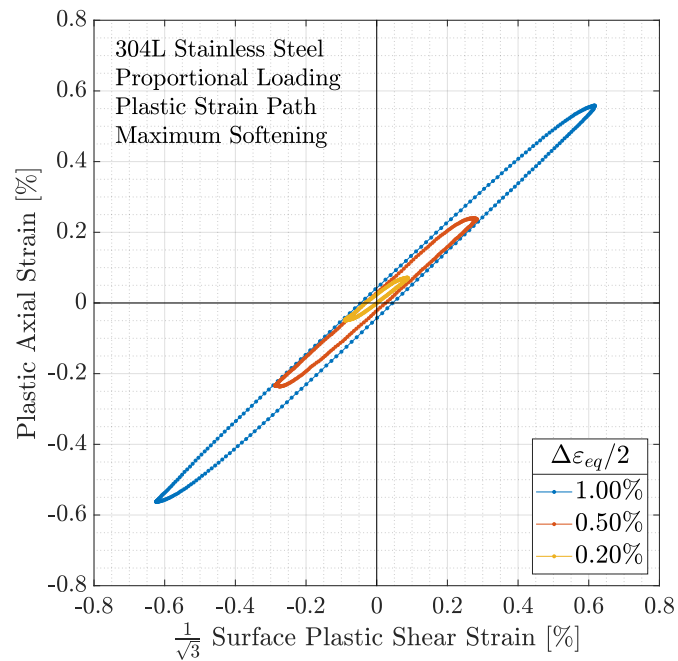


Figure 5.13: Plastic strain paths for selected proportional experiments.

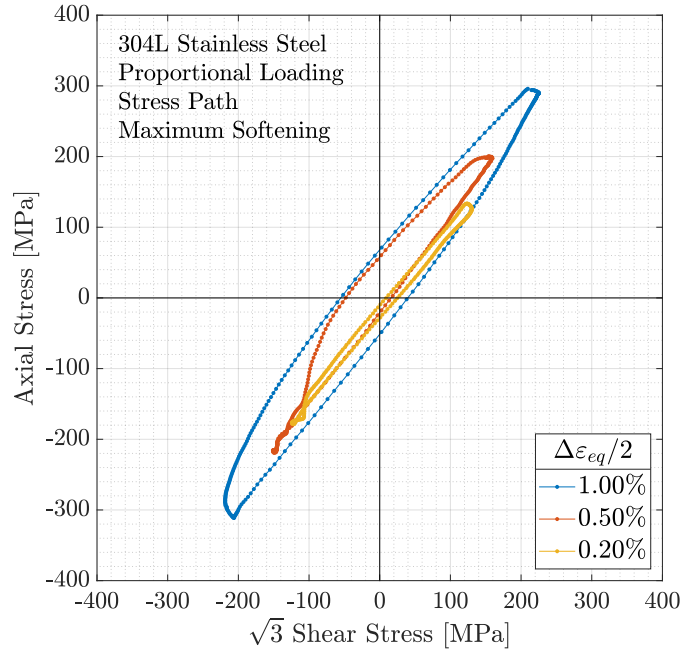


Figure 5.14: Stress paths for selected proportional experiments.

Based upon the results shown in Figures 5.13 and 5.14, there may be neither stress nor plastic strain proportionality given that there is total strain proportionality, which means that, from a stress and plastic strain point of view, those experiments are non-proportional. As discussed in Section 2.3.2, the 304L stainless steel exhibits non-proportional hardening. Nonetheless, stress amplitudes were similar for axial, torsional and proportional experiments for the maximum softening cycle, as shown in Figure 5.15.

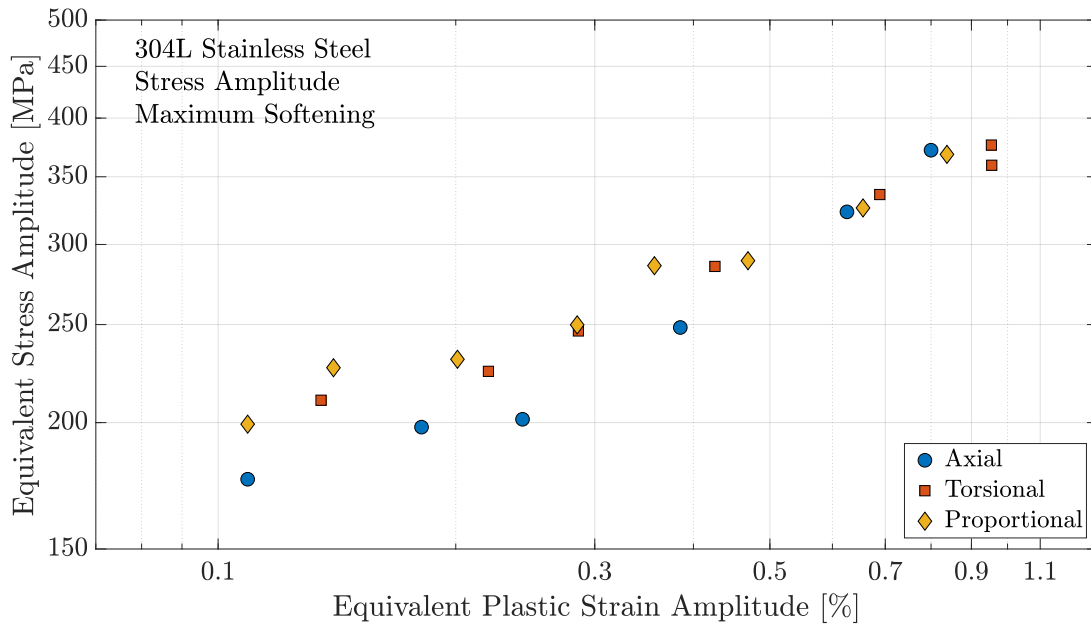


Figure 5.15: Equivalent stress amplitude vs. equivalent plastic strain amplitude for minimum softening.

5.3 Fatigue models

5.3.1 Determination of the material constants

Run-out data

Run-out data is a set of experiments that were halted by the user, even if fatigue failure has not occurred, after a predetermined number of cycles. Therefore, if the test had not been interrupted, fatigue failure might have occurred. Hence, it is argued that run-out experiments should not be used to obtain fatigue constants, as one does not know their fatigue life, only that $N > N_{run-out}$.

Error functions

Let N_f and N_{est} be the observed and estimated life of a given fatigue experiment. The absolute error can be calculated as

$$\delta N = N_{est} - N_f \quad (5.4)$$

and the relative error as

$$e_{rel} = \left| \frac{N_{est} - N_f}{N_f} \right|. \quad (5.5)$$

It is usual upon fatigue analysis to quantify the error as the ratio between estimated and observed lives as $F = N_{est}/N_f$. Therefore, absolute error can be rewritten as

$$\delta N = N_f(F - 1), \quad (5.6)$$

and relative error as

$$e_{rel} = \left| \frac{FN_f - N_f}{N_f} \right| \Rightarrow e_{rel} = |F - 1|. \quad (5.7)$$

The ordinary least square method minimize the error function

$$\mathcal{E} = \sum_{i=1}^n \delta_i^2 = [N_{obs}^i(F - 1)]^2. \quad (5.8)$$

Due to the N_f factor, the error contribution of a given experiment is dependent upon fatigue life and F , which may yield contradictory results. For two fatigue experiments N_1 and N_2 whose observed fatigue lives are 1×10^4 and 1×10^5 cycles and whose estimated fatigue lives are 9×10^4

and 2×10^5 cycles, respectively, error can be calculated as

$$\mathcal{E} = (9 \times 10^4 - 1 \times 10^4)^2 + (2 \times 10^5 - 1 \times 10^5)^2 = (8 \times 10^4)^2 + (10 \times 10^4)^2. \quad (5.9)$$

From a fatigue analysis point of view, life estimate for N_2 is much better (factor of 2) than for N_1 (factor of 9). However, if the error function proposed in Equation 5.8 is adopted, error for N_2 is actually greater than for N_1 , which means that high cycle fatigue error contribution is more significant than the low cycle one, even if its observed-estimated life ratio is significantly smaller. If a relative error function is adopted,

$$\mathcal{E}' = \left| \frac{9 \times 10^4 - 1 \times 10^4}{1 \times 10^4} \right| + \left| \frac{2 \times 10^5 - 1 \times 10^5}{1 \times 10^5} \right| = 8 + 1. \quad (5.10)$$

The relative error may be misleading too. Let N_3 be a fatigue experiment, and $N_{est}^1 = 0.1N_3$ and $N_{est}^2 = 10N_3$ two life estimates. The absolute relative error can be calculated as

$$\mathcal{E}' = |0.1 - 1| + |10 - 1| = 0.9 + 9. \quad (5.11)$$

Again, two experiments with the same F ratio have distinct errors. Therefore, a logarithmical error function is proposed:

$$\mathcal{E}'' = \left| \ln \left(\frac{N_{est}}{N_f} \right) \right| \quad (5.12)$$

For N_1 and N_2 ,

$$\mathcal{E}'' = |\ln 9| + |\ln 2|, \quad (5.13)$$

and for N_{est}^1 and N_{est}^2 ,

$$\mathcal{E}'' = |\ln 0.1| + |\ln 10| = |-\ln 10| + |\ln 10| = 2 \ln 10. \quad (5.14)$$

Hence, the logarithmical error function does not distinguish between conservative and non-conservative errors, whilst the relative error does. However, for the same F ratio, the relative error associated to a conservative estimate is greater than the one associated with a non-conservative one. As a consequence, if this error function is adopted, the error associated to conservative estimates will dominate the fit, whilst non-conservative life estimates will not have the same importance. From an engineering point of view, this is the worst scenario, since there may be a trend to underestimate fatigue life. Therefore, the logarithmical error function was adopted in this work. The fit of Smith–Watson–Topper model for the three discussed error functions at half fatigue life, and the observed vs. estimated life for these three set of material constants are

shown in Figures 5.16 and 5.17, respectively. Note that there are no conservative life estimates for the relative error, whilst the least square fit predict almost perfectly experiments whose $N_f \geq 1 \times 10^4$ cycles, but fails to predict ($F > 2$) experiments whose $N_f \leq 2 \times 10^3$ cycles.

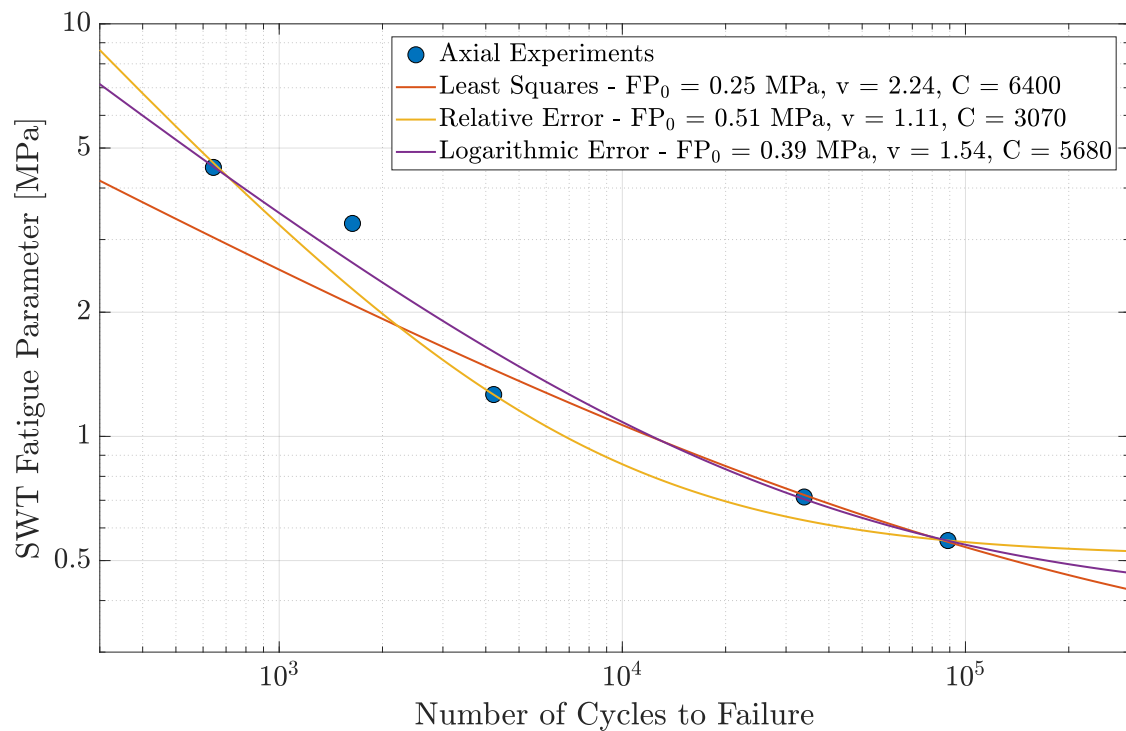


Figure 5.16: Smith–Watson–Topper material constants obtained from three different error functions at half fatigue life.

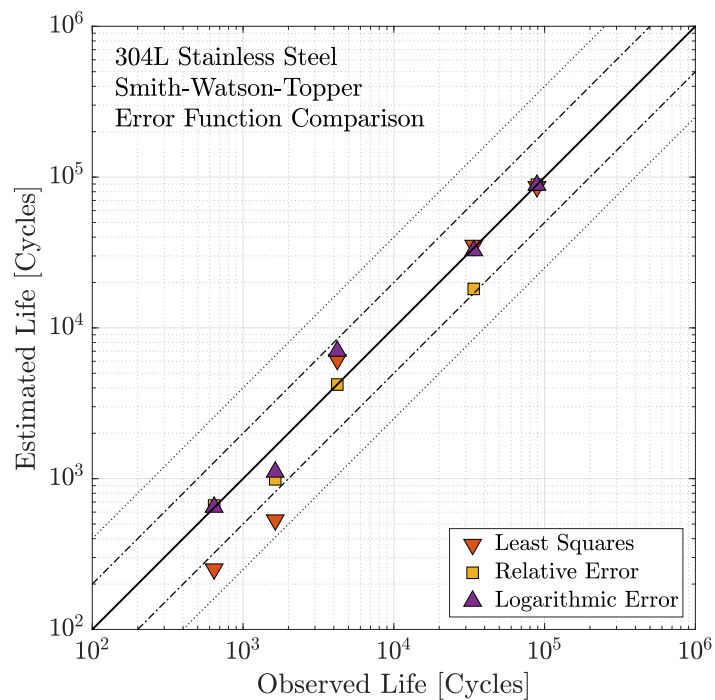


Figure 5.17: Life prediction for the Smith–Watson–Topper model for three different sets of material constants obtained from different error functions at half fatigue life.

Choice of stabilized cycle influence

In order to assess the influence of the choice of the stabilized cycle upon fatigue life estimate, the material constants of the Smith–Watson–Topper model were obtained from five reference cycles: three percentages of the fatigue life ($0.2N_f$, $0.5N_f$ and $0.8N_f$), the cycle of maximum softening and the cycle in which fatigue parameters was equal to the average fatigue parameter of a given experiment. It is shown in Figure 5.18 the material constants of the Smith–Watson–Topper model for those cycles.

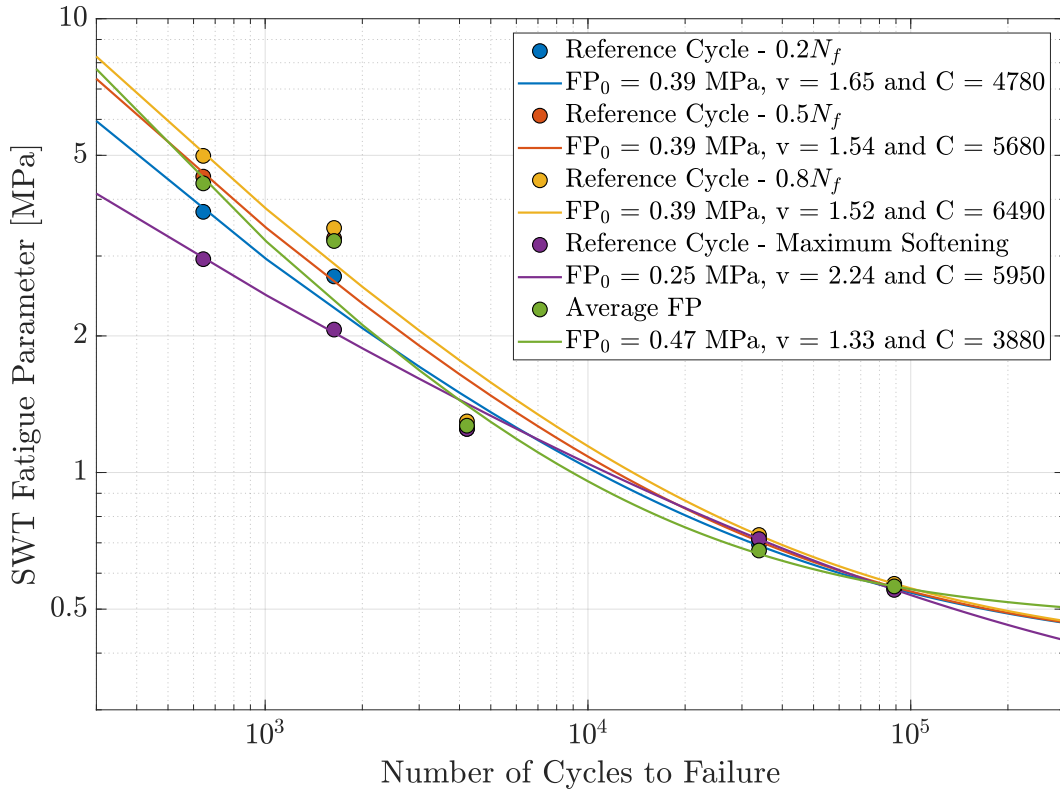


Figure 5.18: Smith–Watson–Topper material constants for different reference cycles.

For the Smith–Watson–Topper model, there was no significant difference for experiments in which secondary hardening was not very pronounced, whilst there was a reasonable difference for $\Delta\varepsilon_{eq} = 0.80\%$ and $\Delta\varepsilon_{eq} = 1.00\%$. Nonetheless, as shown in Figure 5.19, the ratio f is less than 2 (represented by the dashed lines) for life estimates obtained from material constants of half fatigue life cycle for all selected cycles.

For the Fatemi–Socie model, the value of k was obtained by performing multiple fits with a set of predetermined value for k . The fit whose logarithm error was minimum was selected. The material constants of the Fatemi–Socie model obtained from $0.2N_f$, $0.5N_f$, $0.8N_f$ and the cycle of maximum softening are shown in Figure 5.20. As for the Smith–Watson–Topper model, the ratio F is less than 2 for almost all life estimates obtained from material constants of $0.5N_f$ cycle for all selected cycles, shown in Figure 5.21.

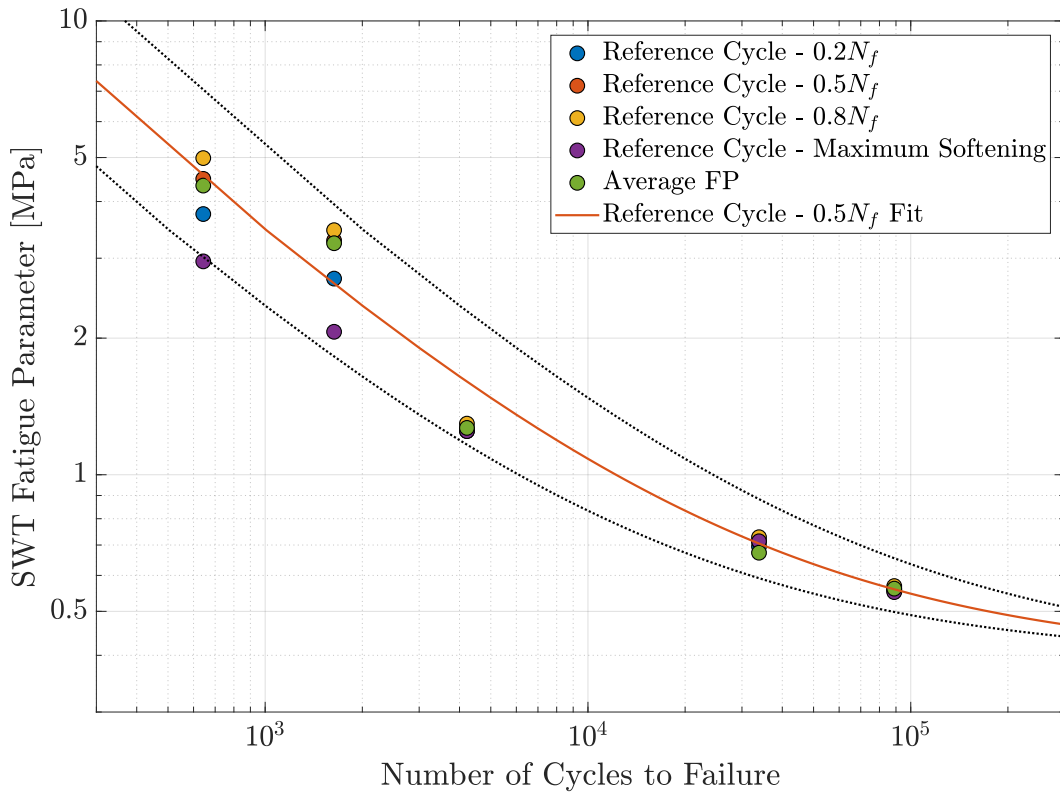


Figure 5.19: Smith–Watson–Topper fit for half fatigue life.

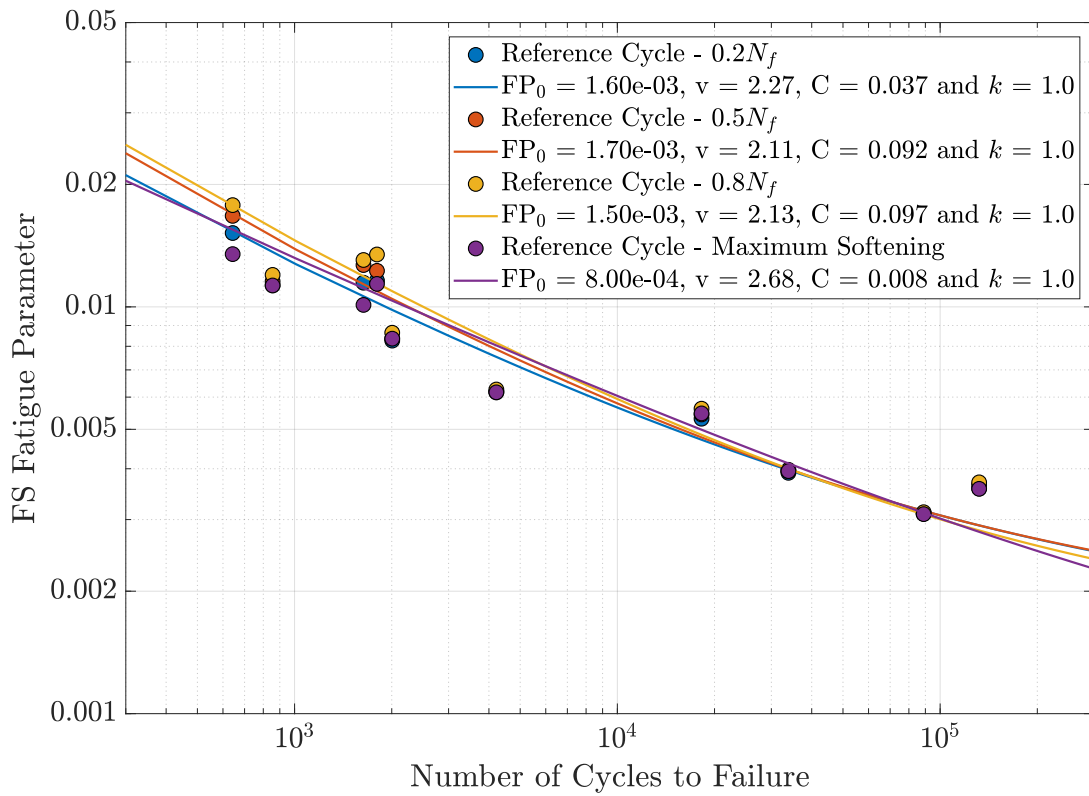


Figure 5.20: Fatemi–Socie material constants for different reference cycles.

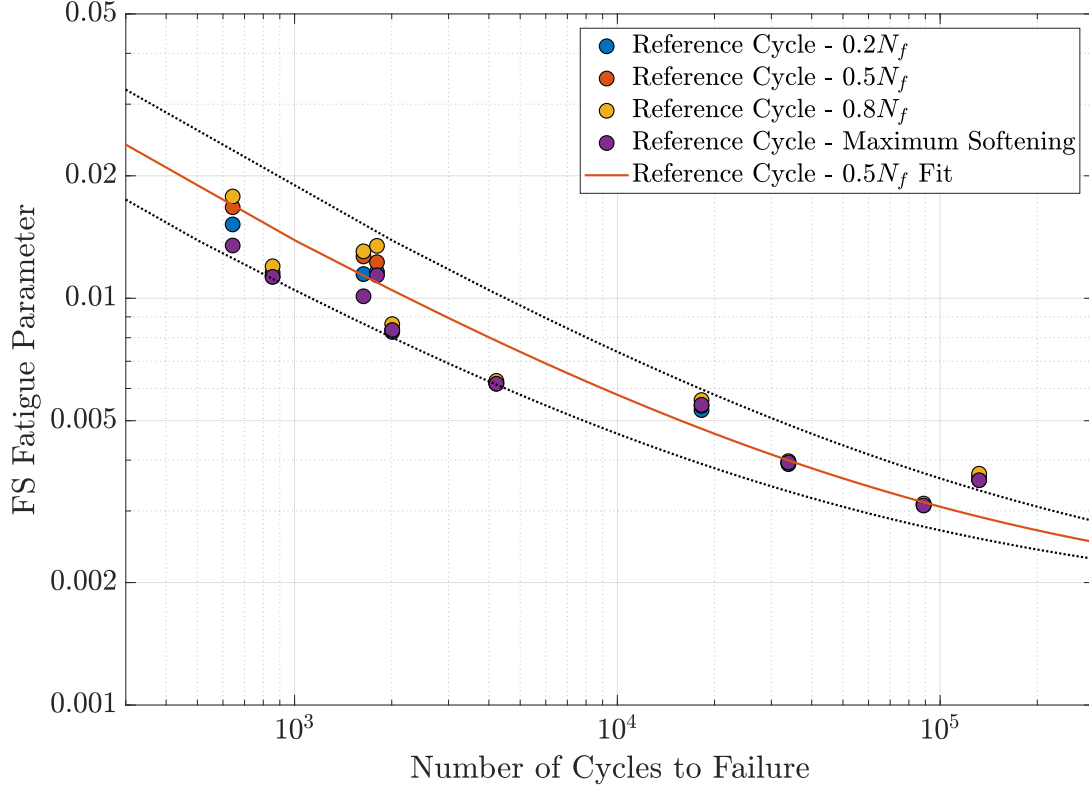


Figure 5.21: Fatemi–Socie fit for half fatigue life.

5.3.2 Life predictions

Smith–Watson–Topper model

It is shown in Figures 5.22–5.26 the fatigue life estimates for the five sets of material constants shown in Figure 5.18. The dash-dot line represents the factor of two, whilst the dashed one represents the factor of four.

The average logarithmic error of life estimates, which does not consider run-out data, were $\mathcal{E}_{MS}'' = 0.3768$ ($\bar{F} = 1.44$), $\mathcal{E}_{0.2}'' = 0.4339$ ($\bar{F} = 1.54$), $\mathcal{E}_{0.5}'' = 0.4426$ ($\bar{F} = 1.55$), $\mathcal{E}_{0.8}'' = 0.4084$ ($\bar{F} = 1.50$), and $\mathcal{E}_{avg}'' = 1.0426$ ($\bar{F} = 2.83$). For stabilized cycles defined as a percentage of fatigue life, errors were similar, which suggests that there is almost no influence of secondary hardening upon fatigue life percentage obtained from reference cycles defined as a percentage of the fatigue life.

For the maximum softening estimates, the two torsional experiments whose life predictions were such that $F > 2$ were obtained for experiments that exhibited significant secondary hardening. On the other hand, there was an almost perfect estimate the other torsional experiment whose $\Delta\varepsilon_{eq} = 1.00\%$, which featured significant secondary hardening too. Therefore, it seems that life estimates for torsional loading such that $F > 2$ are not caused by the secondary hardening.

Two out of four torsional loading that exhibited shear cracking mode and the one whose mode

was tensile were predicted accurately ($F < 2$) for the maximum softening life estimates. For the reference cycle $0.2N_f$, $F > 2$ for the shear mode experiment. Therefore, it may be argued that torsional life estimates such that $F > 2$ are not associated with the cracking mode.

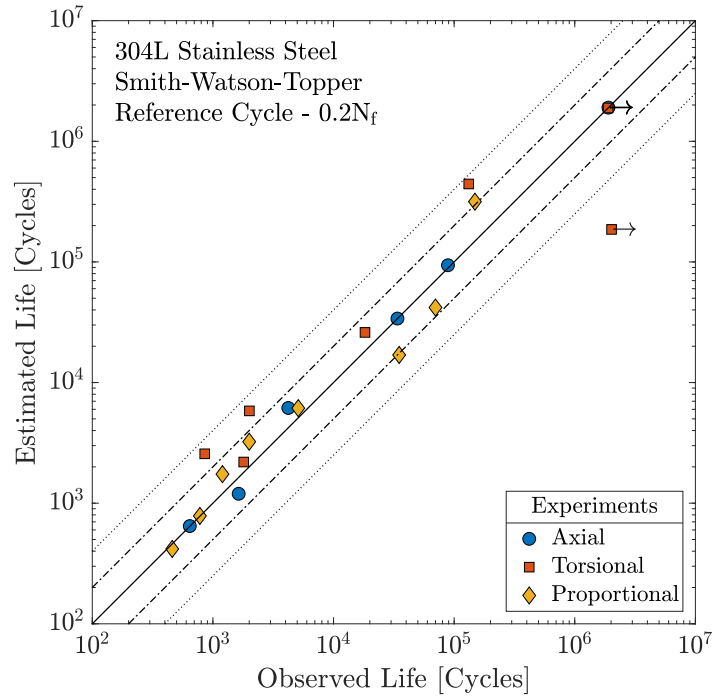


Figure 5.22: Smith–Watson–Topper life estimates for $0.2N_f$.

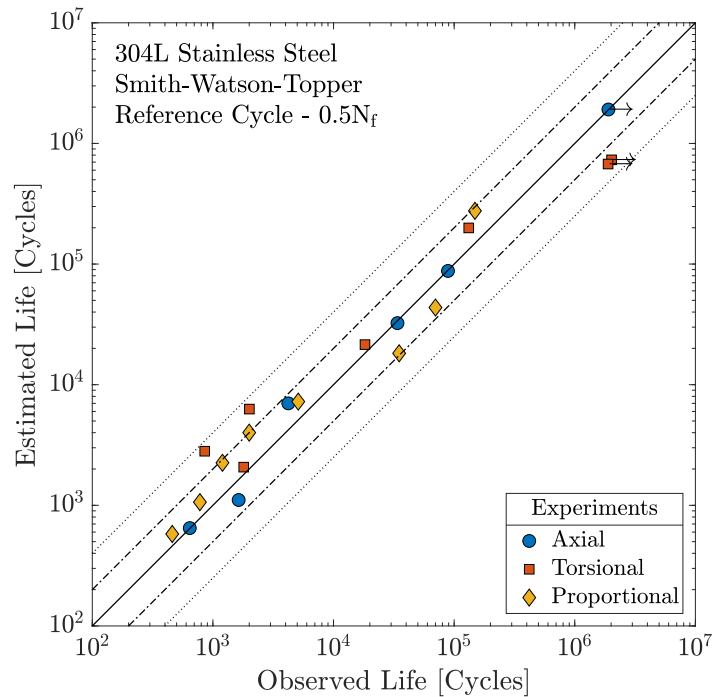


Figure 5.23: Smith–Watson–Topper life estimates for $0.5N_f$.

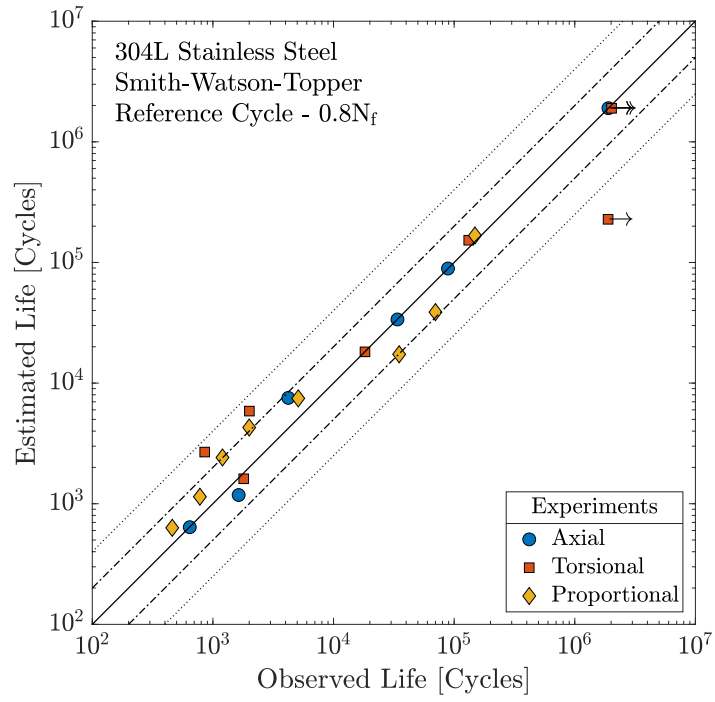


Figure 5.24: Smith–Watson–Topper life estimates for $0.8N_f$.

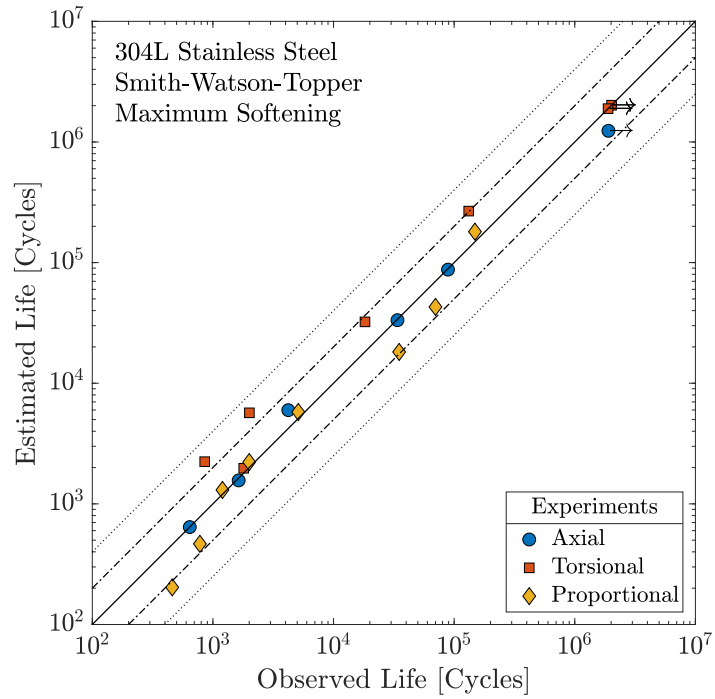


Figure 5.25: Smith–Watson–Topper life estimates for maximum softening.

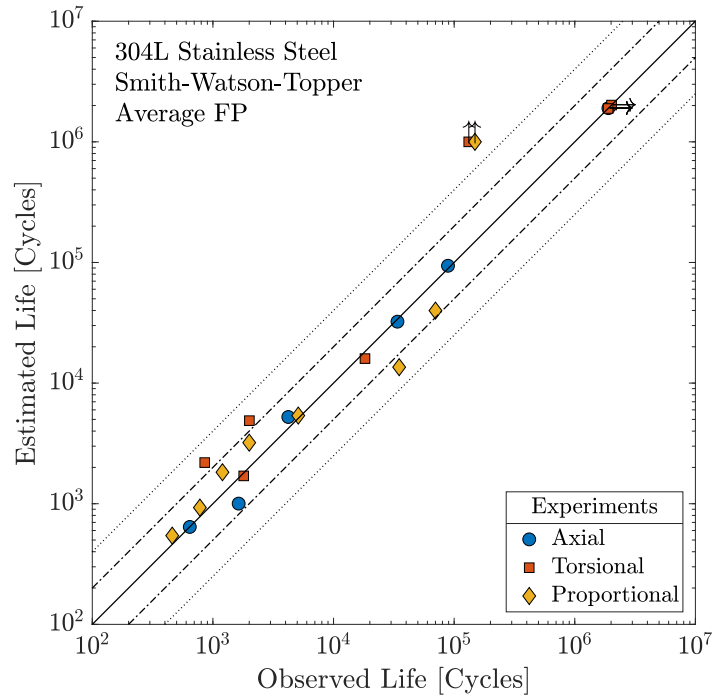


Figure 5.26: Smith–Watson–Topper life estimates for average fatigue parameter.

Fatemi–Socie model

It is shown in Figures 5.27–5.30 the life estimates for the four sets of material constants shown in Figure 5.20. The dash-dot line represents the factor of two, whilst the dashed one represents the factor of four.

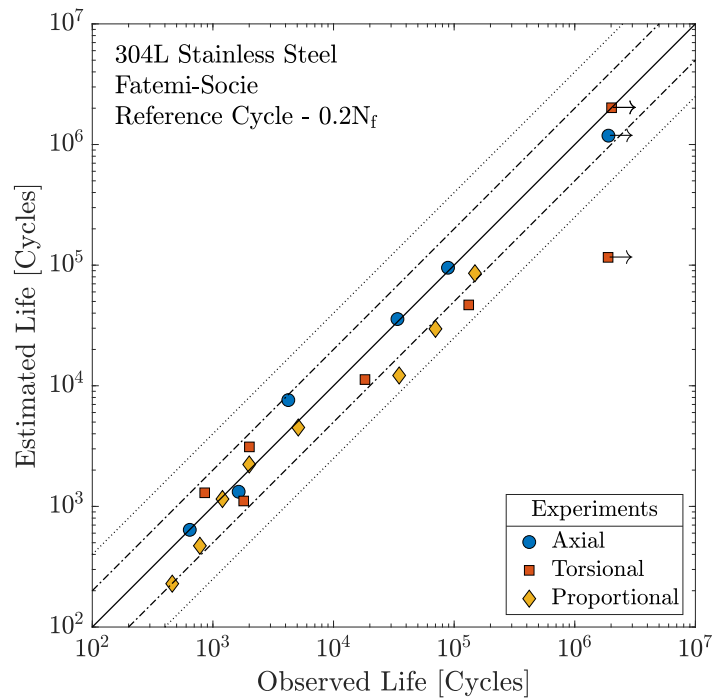


Figure 5.27: Fatemi–Socie life estimates for $0.2N_f$.

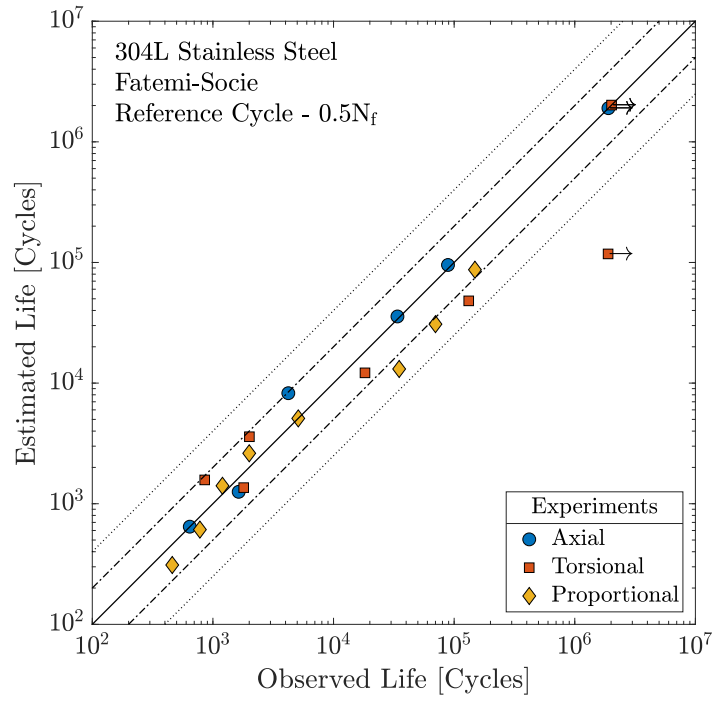


Figure 5.28: Fatemi–Socie life estimates for $0.5N_f$.

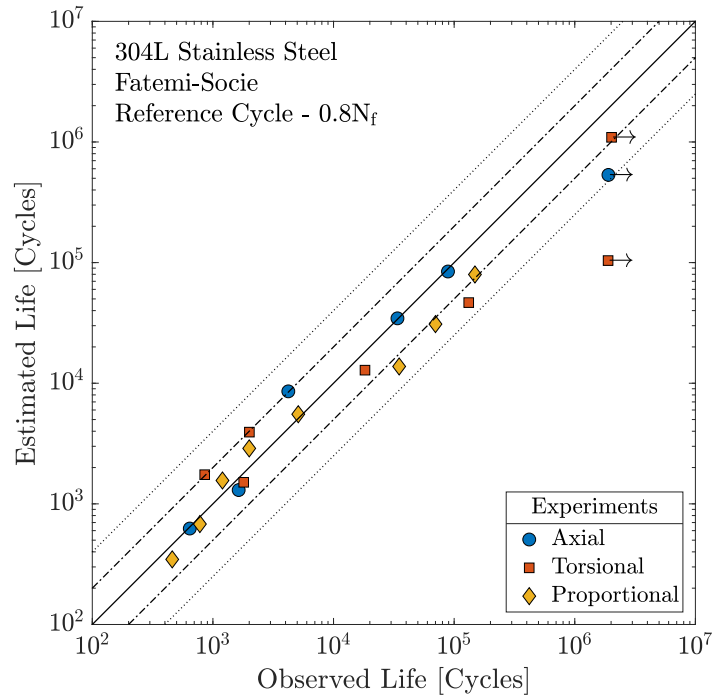


Figure 5.29: Fatemi–Socie life estimates for $0.8N_f$.

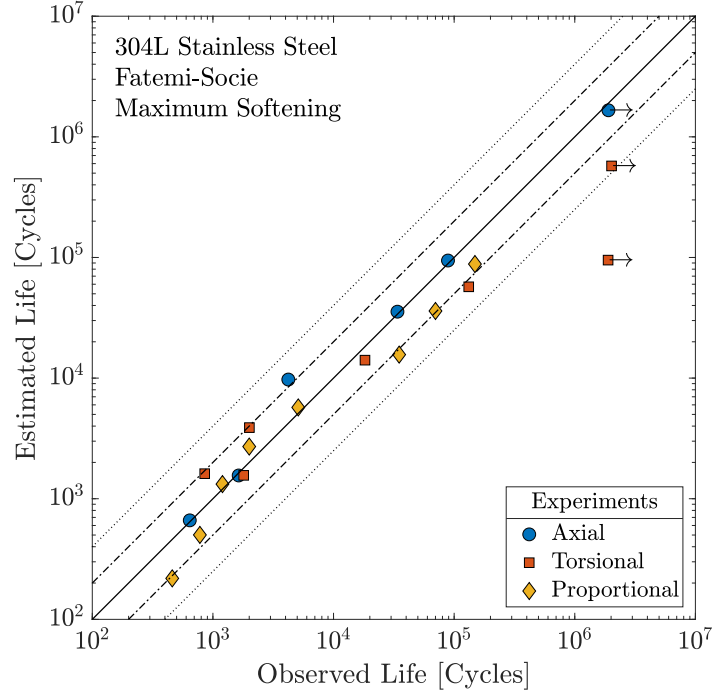


Figure 5.30: Fatemi–Socie life estimates for maximum softening.

The average logarithmic error of life estimates was $\mathcal{E}_{MS}^{\bar{\epsilon}} = 0.4024$ ($\bar{F} = 1.50$), $\mathcal{E}_{0.2}^{\bar{\epsilon}} = 0.4295$ ($\bar{F} = 1.54$), $\mathcal{E}_{0.5}^{\bar{\epsilon}} = 0.4088$ ($\bar{F} = 1.50$), and $\mathcal{E}_{0.8}^{\bar{\epsilon}} = 0.4164$ ($\bar{F} = 1.52$). This result suggests that there is no influence of secondary hardening upon the life estimates for the Fatemi–Socie model.

5.3.3 Critical plane orientation

As discussed in Section 3.1, the Smith–Watson–Topper model predicts $\theta = 0$ and $\theta = \pm 45^\circ$ for axial and torsional loading, respectively. For Fatemi–Socie model, θ depends upon k . The observed and predicted crack orientation for both models are shown in Figures 5.31–5.36. Photographs of the observed fatigue cracks are shown in Appendix B.

The Smith–Watson–Topper model predicts all axial, one torsional and three proportional, an accuracy of approximately 44 %. The Fatemi–Socie models did not predict any crack orientation accurately, including the torsional loading whose $\Delta\epsilon_{eq}/2 > 0.35\%$, which seems incoherent since the 304L stainless steel exhibits a shear cracking mode. The Fatemi–Socie model originally is shear-based, as it defines the critical plane as the plane in which shear strain is maximum. If the critical plane is defined as the plane in which fatigue parameter is maximum, the cracking mode assumed by the model depends upon k . For the proportional loading, there is a smooth transition between crack modes, which is tensile for low strain amplitudes and mixed for all other amplitudes.

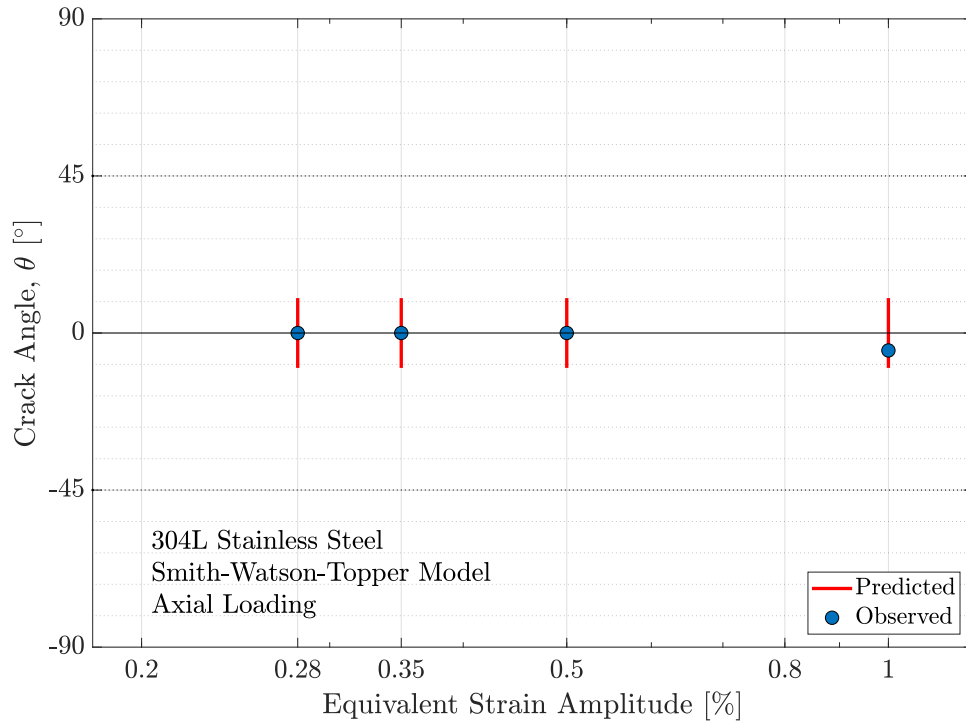


Figure 5.31: Observed and predicted fatigue crack angle based upon the Smith–Watson–Topper for axial loading.

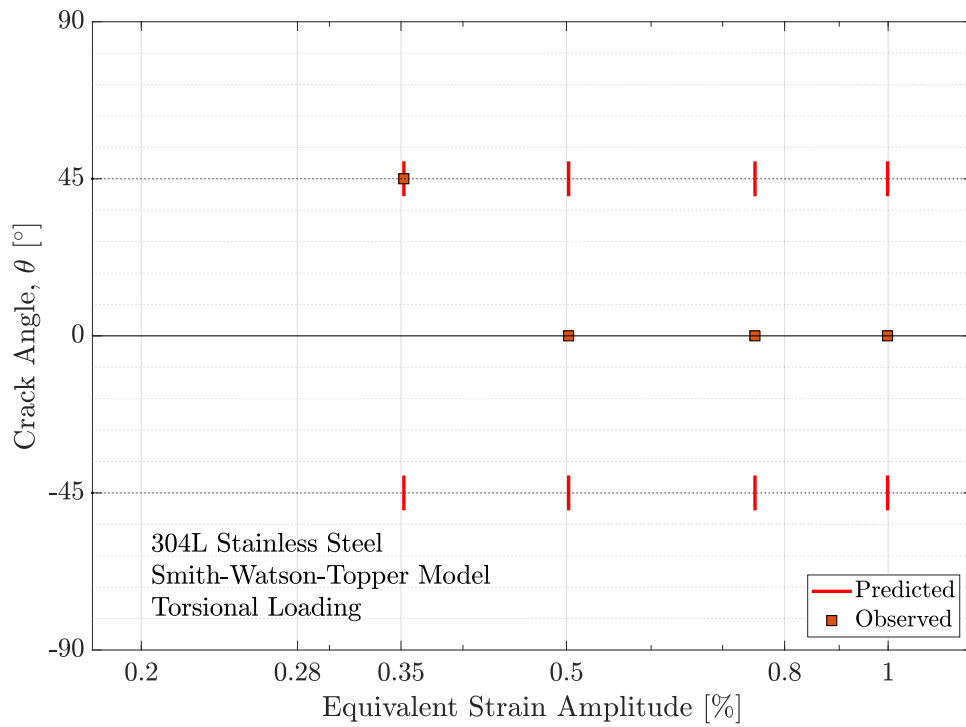


Figure 5.32: Observed and predicted fatigue crack angle based upon the Smith–Watson–Topper for torsional loading.

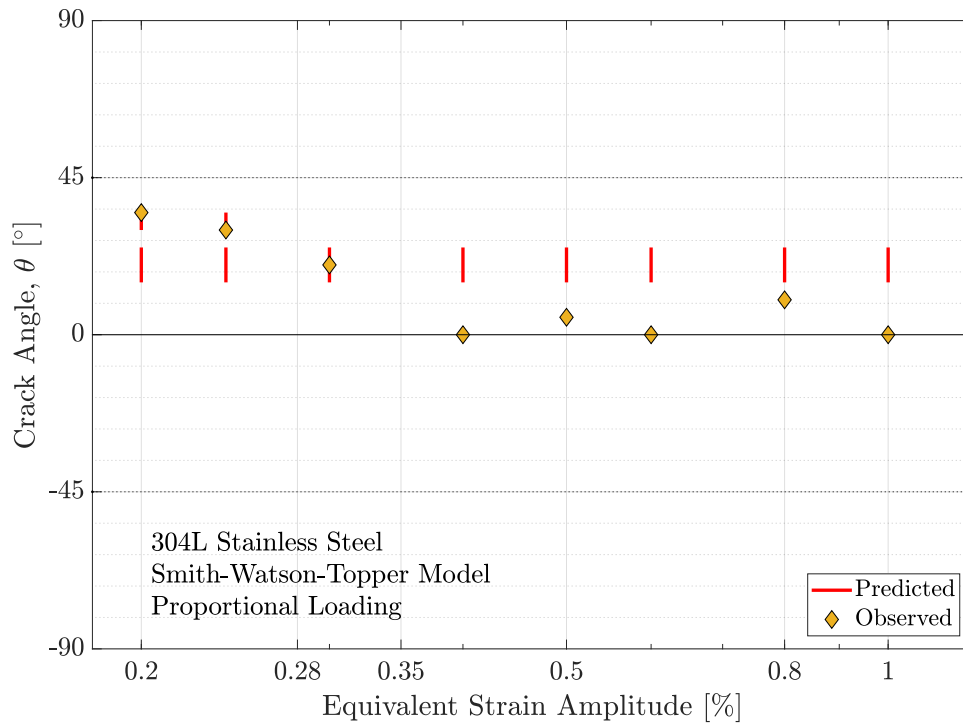


Figure 5.33: Observed and predicted fatigue crack angle based upon the Smith–Watson–Topper for proportional loading.

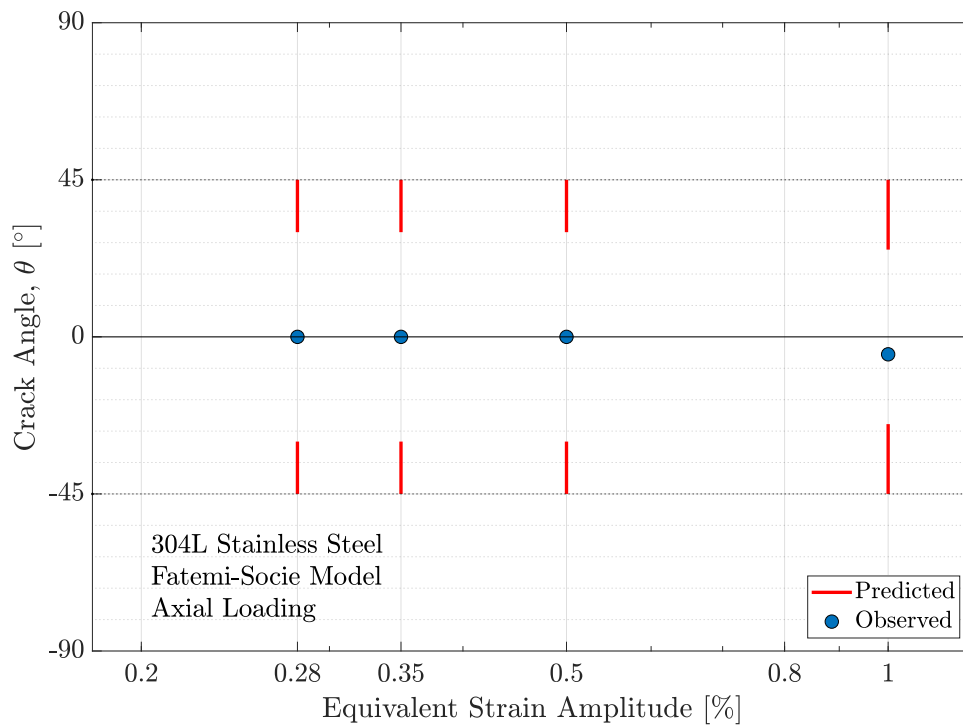


Figure 5.34: Observed and predicted fatigue crack angle based upon the Fatemi–Socie for axial loading.

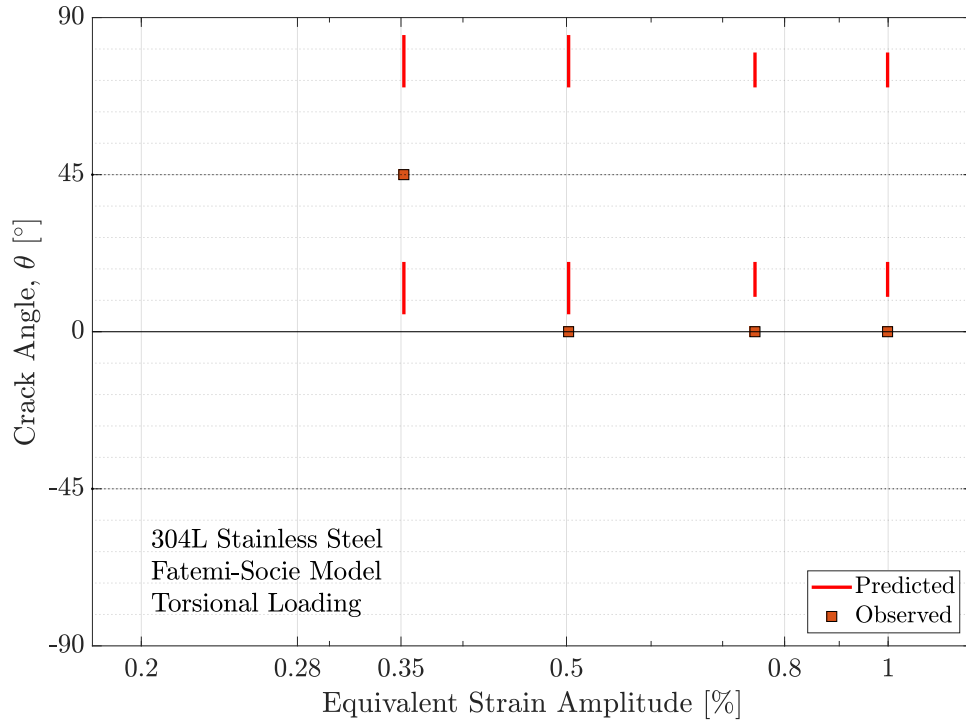


Figure 5.35: Observed and predicted fatigue crack angle based upon the Fatemi–Socie for torsional loading.

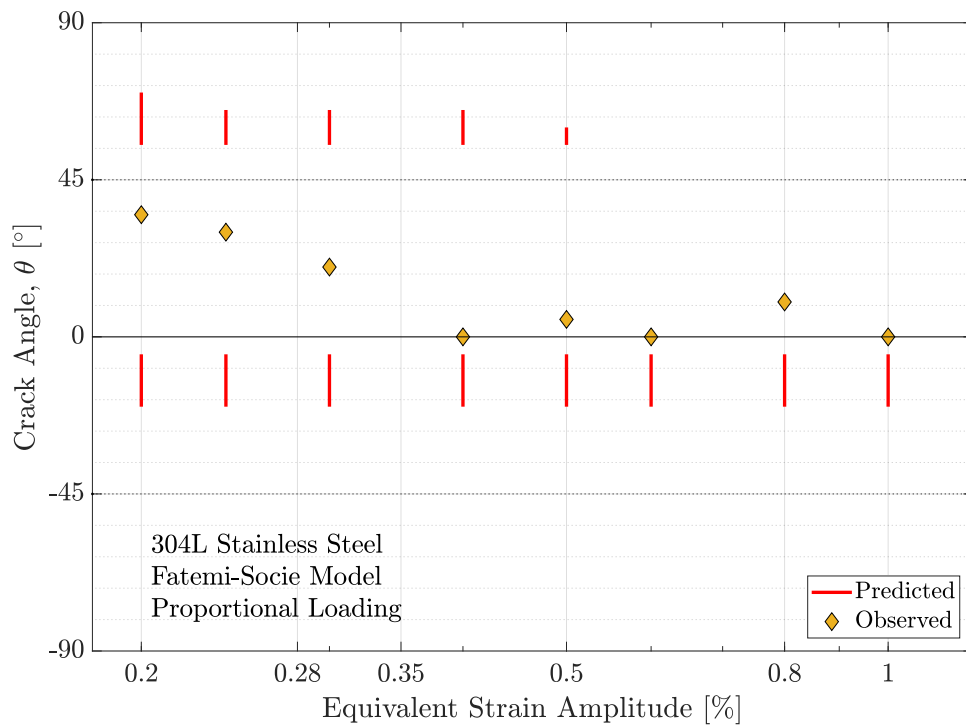


Figure 5.36: Observed and predicted fatigue crack angle based upon the Fatemi–Socie for proportional loading.

5.4 Further discussion

5.4.1 Hysteresis Loops

During proportional experiments, the shape of hysteresis loops was not impeccable, especially the torsion one, as presented in Figure 5.37.

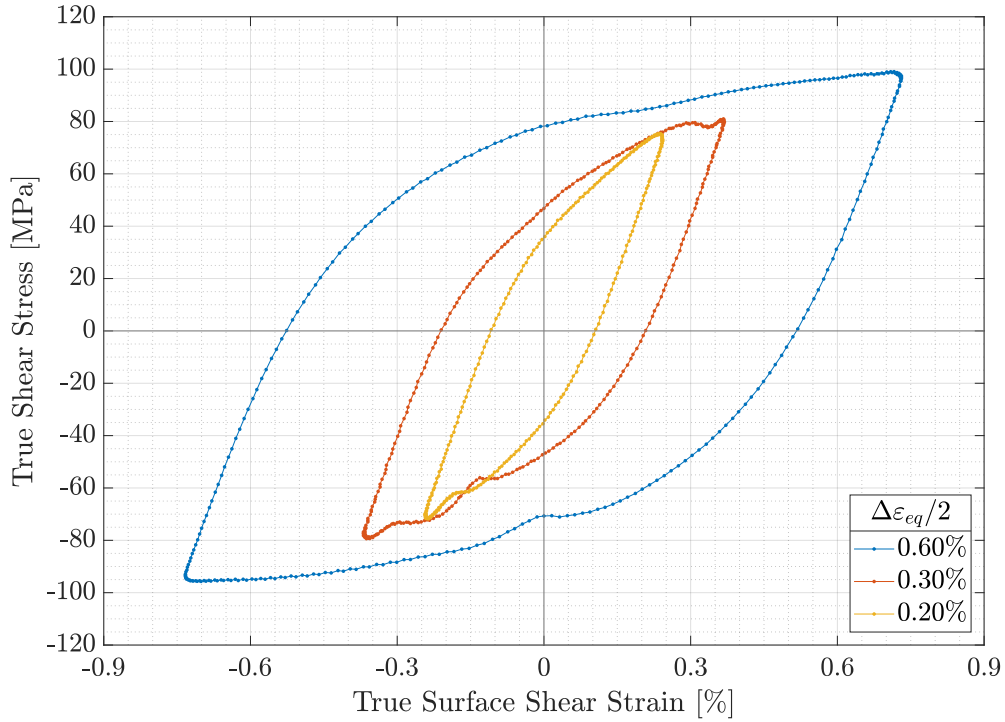


Figure 5.37: Shear hysteresis loops for selected proportional experiments.

It was observed that force and torque waveforms were poor at the point in which imperfections had appeared. Hence, several solutions to mitigate this problem have been tested:

1. The influence of specimens' grip area was tested. There was no significant difference between loops obtained from tests in which 25 mm or all the grip end were placed inside the collet.
2. Since force and torque waveforms seemed to be the problem, a tuning upon force and torque was performed, with no success at all.
3. A warm-up of the test machine was introduced. With no specimen, a displacement of 0.8 mm and an angle of 6° were prescribed upon the collet before the proper test. This solution has been reasonably successful.

Even after the introduction of the warm-up, there were still some problems with the hysteresis loops. It was observed that prescribed waveforms degenerated slightly throughout the test, causing imperfections upon loops that were previously impeccable.

5.4.2 Cyclic stress-strain behaviour

As reported in Section 2.1, the secondary hardening is associated with a martensitic transformation. Therefore, a rigorous modelling of this phenomenon must consider some quantity associated with martensite, as volume or mass fraction, for example. It was assumed in this work that the secondary hardening starts at the minimum softening cycle, which may not be true since there may be a competition between the cyclic softening and the secondary hardening. From this point of view, the maximum softening may be understood as the moment in which the hardening associated with this phase transformation overcomes the cyclic softening, not the initiation of the secondary hardening.

According to Mughrabi and Christ (1997), one of the hypotheses of the Masing-type behaviour is that there are no microstructural changes during the loading cycles, which means that it can only occur if the same microstructure prevails. In this work, the analysis of the Masing behaviour was performed at the maximum softening, which means that there was no significant martensitic transformation if the above-mentioned hypothesis for the initiation of the secondary hardening is verified. Therefore, the crystalline structure is similar for all the compared experiments and the deviation from the Masing behaviour cannot be attributed to the martensitic transformation.

For the proportional experiments, which were non-proportional upon deviatoric stress and plastic strain spaces, equivalent stress amplitudes were similar to those of axial and torsional experiments for the maximum softening cycle, a result that must be analysed with caution. Since non-proportionality is not very pronounced, especially for the plastic strain space, the increase of the stress amplitude associated with non-proportional hardening may be very mild. Another possible interpretation is that the non-proportional hardening is associated with total strain non-proportionality. If the latter interpretation is correct, an important consequence is that non-proportional hardening models based upon the deviatoric stress and plastic strain spaces will predict a stress amplitude greater than the observed, especially for the 304L stainless steel, whose additional hardening due to non-proportionality is very pronounced.

5.4.3 Fatigue analysis

The three parameter equation used to estimate fatigue life assumes the hypothesis that there is a fatigue limit, which may affect significantly the error due to the asymptotic behaviour of this equation, investigated here for the Smith–Watson–Topper model:

1. Let $FP_0^1 = 0.456$ MPa, $FP_0^2 = 0.460$ MPa and $FP_0^3 = 0.464$ MPa be three values of FP_0 that can be rounded to 0.47 MPa. For the proportional experiment whose $\Delta\varepsilon_{eq} = 0.20\%$, $FP = 0.4661$ MPa for the average fatigue cycle analysis, and life estimates for the three values of FP_0 are $N_{est}^1 = 1.73 \cdot 10^6$ cycles, $N_{est}^2 = 3.39 \cdot 10^6$ cycles and $N_{est}^3 = 1.37 \cdot 10^7$ cycles, a ratio $N_{est}^3/N_{est}^1 \approx 8$. If this proportional and a torsional experiments whose life estimates were very poor are not taken into account, $\mathcal{E}_{avg}^{\bar{F}} = 0.3623$ ($\bar{F} = 1.44$) for the

original $FP_0 = 0.47$ MPa, similar to the maximum softening analysis.

2. Let FP_1 and FP_2 be two fatigue parameters such that $FP_1 = 0.476$ MPa and $FP_2 = 0.484$ MPa, which can be both rounded to 0.48 MPa. Life estimates obtained for the material constants from the average fatigue parameter are $N_{est}^1 = 3.50 \cdot 10^6$ cycles and $N_{est}^2 = 1.13 \cdot 10^6$ cycles, a ratio of approximately 3. For $FP_3 = 0.99$ MPa and $FP_4 = 1.00$ MPa, $N_{est}^3 = 9.25 \cdot 10^3$ cycles and $N_{est}^4 = 9.02 \cdot 10^3$ cycles, a ratio of approximately 1.0, which means that low cycle experiments are far less sensitive to numerical errors.

Therefore, one shall assess carefully the error of life estimates whose fatigue parameter is close to FP_0 since they are much more sensitive to numerical errors than other experiments.

Despite their diametrically opposed hypotheses, life estimates for both models are quite similar. This suggests that there is no influence of the reference cycle upon fatigue life estimates. A more rigorous life estimate method is the integration of the damage throughout the cycles, as presented in Equation 3.8. However, this approach has an important drawback: if the cumulative damage calculated up to fatigue life is less than 1, there must be an extrapolation of the fatigue parameter evolution throughout the loading cycles in order to estimate fatigue life. Whichever extrapolation is adopted, there is an additional hypothesis that may contribute to errors upon fatigue life estimates, as one does not know how the material would have behaved had it not failed (e.g. the secondary hardening evolution may not be similar to the one observed hitherto). Since life estimates obtained from a reference cycle were very good, this analysis is not necessary.

Due to the mixed cracking mode, it was expected that both models could not predict crack orientation for axial and torsional loading, especially due to the crack mode change observed upon low strain amplitudes for torsional experiments. Nonetheless, fatigue life was estimated accurately for the three strain paths, which may lead to the following question: have both models been successful? The Fatemi–Socie model failed to predict crack orientation for all experiments, although life predictions were correct, which may argue in favour of a pragmatic outlook. On the other hand, a rigorous interpretation, which is assumed by this author, may argue that both critical planes and fatigue life must be predicted accurately due to the physical nature of these models.

Axial experiments whose $\Delta\varepsilon_{eq}/2 \geq 0.80\%$ exhibited multiple fatigue cracks, similar to the Region I-type behaviour of the 304 stainless steel investigated by Bannantine and Socie (1988). For torsional experiments, a Region II-type behaviour without multiple cracking may have been observed for $\Delta\varepsilon_{eq}/2 = 0.50$ and 0.75% since there was bifurcation after the fatigue crack had reached a certain length, and a Region-III-type behaviour occurred for $\Delta\varepsilon_{eq}/2 = 0.35\%$. Axial experiments whose $\Delta\varepsilon_{eq}/2 \leq 0.60\%$ and torsional ones whose $\Delta\varepsilon_{eq}/2 \geq 0.50\%$ exhibited the same crack orientation of Region I experiments, although multiple cracking did not occur. Therefore, it may be argued that axial and torsional loading have displayed a behaviour similar to the one of the 304 stainless steel investigated by Bannantine and Socie (1988).

For proportional experiments, the fatigue crack of specimen 304LTU35, whose $\Delta\varepsilon_{eq}/2 = 0.40\%$, is of special interest: the direction of propagation changes after a certain length, a Region

II-type behaviour without multiple cracking. On the other hand, proportional experiments whose $\Delta\varepsilon_{eq}/2 < 0.40\%$ did not exhibit a Region III-type behaviour and only displays a crack orientation change. For experiments whose $\Delta\varepsilon_{eq}/2 \geq 0.40\%$, fatigue cracking was similar to the one observed for axial experiments whose $\Delta\varepsilon_{eq}/2 \leq 0.60\%$

The smooth crack orientation change related by Kalnaus (2009) was not observed for torsional experiments. Unlike torsional and proportional loading, axial loads exhibited only tensile mode, which may suggest that this behaviour is not directly linked to equivalent strain amplitudes, but somehow to shear strain amplitudes. It is shown in Figure 5.38 the crack orientation for torsional and proportional experiments vs. the prescribed surface shear strain amplitude.

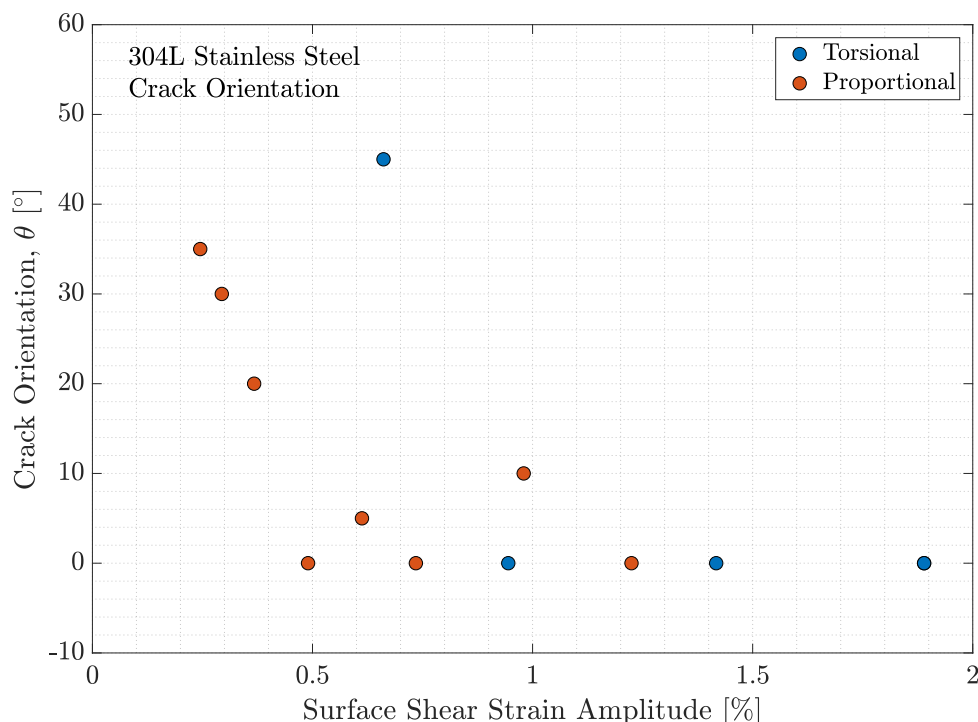


Figure 5.38: Crack orientation vs prescribed shear strain amplitude for torsional and proportional experiments.

There is an almost linear relation between the crack orientation and the strain amplitude for proportional loading whose $\Delta\gamma^{sur}/2 < 0.80\%$. As there is only one torsional experiment at this range, any attempt to verify whether torsional loading exhibit the same trend will demand more experimental data.

Both the Smith-Watson-Topper and the Fatemi-Socie models incorporate stresses and strains into their mathematical formulation. Due to secondary hardening, models that incorporate only stress measures at a given reference cycle may yield very similar life estimates for two experiments whose observed lives are completely different, as for the torsional loading of $\Delta\gamma^{mid}/2 = 0.87\%$ and $\Delta\gamma^{mid}/2 = 0.48\%$ (Fig. 3.1).

Chapter 6 – Conclusions and Suggestions for Future Work

Conclusions

In this work, proportional axial-torsional experiments have been performed. The cyclic stress-strain behaviour of the 304L stainless steel has been investigated through a Masing behaviour analysis, a comparison between secondary hardening observed upon axial, torsional and proportional experiments, and the stress and plastic strain proportionality. Fatigue life and critical plane orientation predictions from the critical plane models of Smith–Watson–Topper and Fatemi–Socie have been compared with axial, torsional and proportional experimental data for the 304L stainless steel. The following conclusions have arisen:

1. Significant or mild secondary hardening was observed for all axial and torsional experiments. For proportional ones, only a mild hardening occurred for $\Delta\varepsilon_{eq}/2 \geq 0.80\%$. Based upon the comparison between stress states, the absence of hardening may be attributed to the occurrence of fatigue failure prior to the initiation of the secondary hardening.
2. A Masing-type behaviour was observed for $\Delta\varepsilon^p \leq 0.5\%$ and $\Delta\gamma^p \leq 1.0\%$. The equivalent von Mises strain amplitude cannot be used as a threshold since there is a Masing-type behaviour for the proportional experiment whose $\Delta\varepsilon_{eq}/2 \geq 0.50\%$, whilst it does not occur for the proportional one with the same equivalent amplitude.
3. Proportional loads are non-proportional upon stress and plastic strain spaces. Despite the absence of stress amplitude increase for the maximum softening cycle, it is not clear whether non-proportional hardening is very mild or nonexistent since non-proportionality is not very pronounced.
4. For the same equivalent strain amplitude, torsional experiments last longer than axial ones, which last longer than proportional experiments. This result is similar to the one observed for axial, torsional and non-proportional experiments by Kalnaus (2009).
5. There has been no significant difference between life estimates obtained from multiple reference cycles and between both fatigue models investigated. The Smith–Watson–Topper model predicted approximately 56% of the observed macroscopic crack orientations for

axial, torsional and proportional experiments accurately, whilst the Fatemi–Socie model failed to predict all crack orientations.

6. The cracking behaviour of the 304L stainless steel exhibits some trends that are similar to the behaviour of the 304 stainless steel investigated by Bannantine and Socie (1988), as the multiple fatigue cracks observed for axial experiments whose $\Delta\varepsilon_{eq} \geq 0.80\%$ and the bifurcation for the torsional load whose $\Delta\varepsilon_{eq} \leq 0.75\%$. A smooth crack orientation change has been observed for proportional experiments, similar to the one observed by Kalnaus (2009) for torsional loads.

Suggestions for future work

Some suggestions for future work are presented below:

1. Investigation the non-proportional hardening through fully reversed 90° out-of-phase non-proportional experiments upon thin-walled tubular specimens in order to obtain the material constants of the Tanaka (1994) model.
2. Performed unbalanced stress and strain-controlled multiaxial fatigue experiments upon thin-walled tubular specimens in order to verify whether cyclic plasticity models, like the one proposed by Zhang and Jiang (2008), can predict both ratcheting and mean stress relaxation.
3. Perform creep-ratcheting tests similar to those of Taleb and Cailletaud (2011) upon thin-walled tubular specimens for torsional, proportional and non-proportional loads.
4. Perform stress-controlled fatigue test upon notched specimens submitted to fully reversed and unbalanced loads.
5. Predict fatigue life and crack orientation of all these experiments through the Smith–Watson–Topper, Fatemi–Socie and the Jiang (2000) models.
6. Quantify the volume or the mass fraction of martensite for axial, torsional, proportional and non-proportional specimens in order to model the secondary hardening.

References

- ASTM (2015). *E2207-15, Standard Practice for Strain-Controlled Axial-Torsional Fatigue Testing with Thin-Walled Tubular Specimens*. West Conshohocken, PA.
- BANNANTINE, J. A. and SOCIE, D. F. (1988). “Observations of cracking behavior in tension and torsion low cycle fatigue”. In: *ASTM special technical publication 942*, pp. 899–921.
- BARI, S. and HASSAN, T. (2002). “An advancement in cyclic plasticity modeling for multiaxial ratcheting simulation”. In: *International Journal of Plasticity* 18.7, pp. 873–894.
- BAUDRY, G. and PINEAU, A. (1977). “Influence of strain-induced martensitic transformation on the low-cycle fatigue behavior of a stainless steel”. In: *Materials Science and Engineering* 28.2, pp. 229–242.
- BAYERLEIN, M., CHRIST, H.-J. and MUGHRABI, H. (1989). “Plasticity-induced martensitic transformation during cyclic deformation of AISI 304L stainless steel”. In: *Materials Science and Engineering: A* 114, pp. L11–L16.
- BELATTAR, A., TALEB, L., HAUET, A. and TAHERI, S. (2012). “Dependence of the cyclic stress-strain curve on loading history and its interaction with fatigue of 304L stainless steel”. In: *Materials Science and Engineering A* 536, pp. 170–180.
- BELATTAR, A., KELLER, C. and TALEB, L. (2016). “Multiscale analysis of the pre-hardening effect on the cyclic behavior and fatigue life of 304L stainless steel”. In: *Materials Science and Engineering A* 662, pp. 468–480.
- BERNASCONI, A. and PAPADOPOULOS, I. V. (2005). “Efficiency of algorithms for shear stress amplitude calculation in critical plane class fatigue criteria”. In: *Computational Materials Science* 34.4, pp. 355–368.
- BROWN, M. W. and MILLER, K. J. (1973). “A theory for fatigue failure under multiaxial stress-strain conditions”. In: *Proceedings of the Institution of Mechanical Engineers* 187.1, pp. 745–755.
- CARNEIRO JUNIOR, L. A. (2017). “Estudo experimental da plasticidade cíclica e fadiga do aço inoxidável 304L”. MSc Dissertation. Universidade de Brasília.
- CASTRO, F. and JIANG, Y. (2016). “Fatigue life and early cracking predictions of extruded AZ31B magnesium alloy using critical plane approaches”. In: *International Journal of Fatigue* 88, pp. 236–246.
- CHABOCHE, J. L. and ROUSSELIER, G. (1983). “On the plastic and viscoplastic constitutive equations—part I: rules developed with internal variable concept”. In: *Journal of Pressure Vessel Technology* 105.2, p. 153.

- CHOPRA, O. K. and GAVENDA, D. J. (1998). “Effects of LWR coolant environments on fatigue lives of austenitic stainless steels”. In: *Journal of pressure vessel technology* 120.2, pp. 116–121.
- CHU, C.-C. (1995). “Fatigue damage calculation using the critical plane approach”. In: *Journal of Engineering Materials and Technology* 117.1, p. 41.
- COLIN, J. (2010). “Deformation history and load sequence effects on cumulative fatigue damage and life predictions”. PhD thesis. University of Toledo, p. 265.
- COLIN, J., FATEMI, A. and TAHERI, S. (2010). “Fatigue behavior of stainless steel 304L including strain hardening, prestraining, and mean stress effects”. In: *Journal of Engineering Materials and Technology* 132.2, p. 021008.
- DANG VAN, K., GRIVEAU, B. and MESSAGE, O. (1989). “On a new multiaxial fatigue limit criterion theory and application”. In: *Mechanical Engineering Publications*, pp. 479–496.
- DOONG, S.-H., SOCIE, D. F. and ROBERTSON, I. M. (1990). “Dislocation substructures and nonproportional hardening”. In: *Journal of Engineering Materials and Technology* 112.4, pp. 456–464.
- FATEMI, A. and SOCIE, D. F. (1988). “A critical plane approach to multiaxial fatigue damage including out-of-phase loading”. In: *Fatigue and Fracture of Engineering Materials and Structures* 11.3, pp. 149–165.
- HADDAR, N. and FISSOLO, A. (2005). “2D simulation of the initiation and propagation of crack array under thermal fatigue”. In: *Nuclear Engineering and Design* 235.9, pp. 945–964.
- HASSAN, T., TALEB, L. and KRISHNA, S. (2008). “Influence of non-proportional loading on ratcheting responses and simulations by two recent cyclic plasticity models”. In: *International Journal of Plasticity* 24.10, pp. 1863–1889.
- HENNESSY, D., STECKEL, G., ALTSTETTER, C. and HENNESSY, D. (1976). “Phase transformation of stainless steel during fatigue.pdf”. In: *Metallurgical Transactions A* 7.3, pp. 415–424.
- HERNÁNDEZ, K. V. F. (2016). “Fadiga e comportamento tensão-deformação cíclico da liga de alumínio 7050-T7451”. MSc Dissertation. Universidade de Brasília, p. 54.
- HUDA, Z. and EDI, P. (2013). “Materials selection in design of structures and engines of supersonic aircrafts: a review”. In: *Materials & Design* 46, pp. 552–560.
- ITOH, T, SAKANE, M, OHNAMI, M and SOCIE, D. F. (1995). “Nonproportional low cycle fatigue criterion for type 304 stainless steel”. In: *Journal of Engineering Materials and Technology* 117.3, pp. 285–292.
- ITOH, T, CHEN, X, NAKAGAWA, T and SAKANE, M (2000). “A simple model for stable cyclic stress-strain relationship of type 304 stainless steel under nonproportional loading”. In: *Journal of Engineering Materials and Technology* 122.January, pp. 1–9.
- JIANG, Y. (2000). “A fatigue criterion for general multiaxial loading”. In: *Fatigue and Fracture of Engineering Materials and Structures* 23.1, pp. 19–32.
- JIANG, Y. and KURATH, P. (1997a). “Nonproportional cyclic deformation: critical experiments and analytical modeling”. In: *International Journal of Plasticity* 13.8-9, pp. 743–763.

- JIANG, Y. and KURATH, P. (1997b). “An investigation of cyclic transient behavior and implications on fatigue life estimates”. In: *Journal of Engineering Materials and Technology* 119.2, p. 161.
- JIANG, Y., HERTEL, O. and VORMWALD, M. (2007). “An experimental evaluation of three critical plane multiaxial fatigue criteria”. In: *International Journal of Fatigue* 29.8, pp. 1490–1502.
- KALNAUS, S. (2009). “Investigation of fatigue behavior of two austenitic stainless steels”. PhD thesis. University of Nevada, p. 199.
- KANG, G., GAO, Q. and YANG, X. (2004). “Uniaxial and non-proportionally multiaxial ratcheting of SS304 stainless steel at room temperature: Experiments and simulations”. In: *International Journal of Non-Linear Mechanics* 39.5, pp. 843–857.
- KRAL, M. V., MAHER, C. M. and MCSWAIN, R. H. (2018). “Failure analysis of a brazed, stainless steel fuel injection line”. In: *Engineering Failure Analysis*.
- KREMPL, E. (1979). “An experimental study of room-temperature creep and relaxation of AISI type 304 stainless steel”. In: *Mech. Phys. Solids* 27, pp. 363–375.
- KREMPL, E and LU, H (1984). “Hardening and rate-dependent behavior of fully annealed AISI type 304 stainless steel under biaxial in-phase and out-of-phase strain cycling at room temperature”. In: *Journal of Engineering Materials and Technology, Transactions of the ASME* 106.4, pp. 376–382.
- KRUPP, U., CHRIST, H. J., LEZUO, P., MAIER, H. J. and TETERUK, R. G. (2001). “Influence of carbon concentration on martensitic transformation in metastable austenitic steels under cyclic loading conditions”. In: *Materials Science and Engineering A* 319-321, pp. 527–530.
- LAMBA, H. S. and SIDEBOTTOM, O. M. (1978a). “Cyclic plasticity for nonproportional paths: part 1—cyclic hardening, erasure of memory, and subsequent strain hardening experiments”. In: *Journal of Engineering Materials and Technology* 100.1, pp. 96–103.
- LAMBA, H. S. and SIDEBOTTOM, O. M. (1978b). “Cyclic plasticity for nonproportional paths part II - comparison with predictions of three incremental plasticity models”. In: *Journal of Engineering Materials and Technology* 100.1, pp. 104–111.
- LIU, M. C. and KREMPL, E. (1979). “A uniaxial viscoplastic model based on total strain and overstress”. In: *Journal of the Mechanics and Physics of Solids* 27.5-6, pp. 377–391.
- MTS (2009). *Series 646 Hydraulic Collet Grips - Product Information*.
- MANSON, S. S. (1965). “Fatigue: a complex subject- some simple approximations”. In: *Experimental Mechanics* 5.4, pp. 193–226.
- MARTINS, C., MOREIRA, J. and MARTINS, J. (2014). “Corrosion in water supply pipe stainless steel 304 and a supply line of helium in stainless steel 316”. In: *Engineering Failure Analysis* 39, pp. 65–71.
- MRÓZ, Z (1969). “An attempt to describe the behaviour of metals under cyclic loading using a more general work hardening model”. In: *Acta Mech.* 7, pp. 199–212.
- MUGHRABI, H. and CHRIST, H. J. (1997). “Cyclic deformation and fatigue of selected ferritic steels : specific aspects review”. In: *ISIJ international* 37, pp. 54–69.

- MÜLLER-BOLLENHAGEN, C., ZIMMERMANN, M. and CHRIST, H.-J. (2010). “Very high cycle fatigue behaviour of austenitic stainless steel and the effect of strain-induced martensite”. In: *International Journal of Fatigue* 32.6, pp. 936–942.
- PRAGER, W. (1955). “The theory of plasticity: a survey of recent achievements”. In: *Proceedings of the Institution of Mechanical Engineers* 169.1, pp. 41–57.
- REED, R. (1962). “The spontaneous martensitic transformations in 18% Cr, 8% Ni steels”. In: *Acta Metallurgica* 10.9, pp. 865–877.
- SHAMSAEI, N., FATEMI, A. and SOCIE, D. F. (2011). “Multiaxial fatigue evaluation using discriminating strain paths”. In: *International Journal of Fatigue* 33.4, pp. 597–609.
- SMITH, K., WATSON, P. and TOPPER, T. (1970). “A stress-strain function for fatigue of metals”. In: *Journal of materials* 5, pp. 767–778.
- SOCIE, D. (1987). “Multiaxial fatigue damage models”. In: *Journal of Engineering Materials and Technology* 109.4, p. 293.
- SOCIE, D. F. and MARQUIS, G. (1997). *Multiaxial Fatigue*. Society of Automotive Engineers, p. 502.
- TALEB, L. and CAILLETAUD, G. (2011). “Cyclic accumulation of the inelastic strain in the 304L SS under stress control at room temperature: Ratcheting or creep?” In: *International Journal of Plasticity* 27.12, pp. 1936–1958.
- TALEB, L., CAILLETAUD, G. and BLAJ, L. (2006). “Numerical simulation of complex ratcheting tests with a multi-mechanism model type”. In: *International Journal of Plasticity* 22.4, pp. 724–753.
- TANAKA, E. (1994). “A nonproportionality parameter and a cyclic viscoplastic constitutive model taking into account amplitude dependences and memory effects of isotropic hardening”. In: *European Journal of Mechanics, A- Solids* 2, pp. 155–173.
- VINCENT, L., LE ROUX, J.-C. and TAHERI, S. (2012). “On the high cycle fatigue behavior of a type 304L stainless steel at room temperature”. In: *International Journal of Fatigue* 38, pp. 84–91.
- YOON, K. B., YU, J. M. and NGUYEN, T. S. (2015). “Stress relaxation cracking in 304H stainless steel weld of a chemical reactor serviced at 560 C”. In: *Engineering Failure Analysis* 56, pp. 288–299.
- YOSHIDA, F. (1990). “Uniaxial and biaxial creep-ratcheting behavior of SUS304 stainless steel at room temperature”. In: *International Journal of Pressure Vessels and Piping* 44.2, pp. 207–223.
- ZHANG, J. and JIANG, Y. (2008). “Constitutive modeling of cyclic plasticity deformation of a pure polycrystalline copper”. In: *International Journal of Plasticity* 24.10, pp. 1890–1915.
- ZHAO, T. and JIANG, Y. (2008). “Fatigue of 7075-T651 aluminum alloy”. In: *International Journal of Fatigue* 30.5, pp. 834–849.
- ZIEGLER, H. (1959). “A modification of Prager’s hardening rule”. In: *Quarterly of Applied Mathematics* 17.1, pp. 55–65.
- ZINKLE, S. J. and WAS, G. S. (2013). “Materials challenges in nuclear energy”. In: *Acta Materialia* 61.3, pp. 735–758.

Appendices

Appendix A – Stresses and Strains

In this section, stresses and strains for axial and torsional experiments upon thin-walled tubular specimens are obtained. As fatigue crack is usually a surface phenomenon, a material point at the specimens' surface under plane stress state and $\phi = \pi/2$ are assumed, as well as plastic incompressibility, which yields $\text{tr}(\boldsymbol{\varepsilon}^p) = 0$. A three-dimensional orthonormal base xyz is adopted.

A.1 Axial load

For an axial load upon a linear elastic isotropic material, stress tensor $\boldsymbol{\sigma}$ could be written as follows:

$$\boldsymbol{\sigma}(t) = \begin{bmatrix} \sigma_x(t) & 0 & 0 \\ 0 & 0 & 0 \\ 0 & 0 & 0 \end{bmatrix}. \quad (\text{A.1})$$

The elastic component of the strain tensor $\boldsymbol{\varepsilon}$ could be calculated as follows:

$$\boldsymbol{\varepsilon}^e(t) = \begin{bmatrix} \varepsilon_x^e(t) & 0 & 0 \\ 0 & -\nu\varepsilon_x^e(t) & 0 \\ 0 & 0 & -\nu\varepsilon_x^e(t) \end{bmatrix}. \quad (\text{A.2})$$

The plastic component of the strain tensor $\boldsymbol{\varepsilon}$ could be calculated as follows:

$$\boldsymbol{\varepsilon}^p(t) = \begin{bmatrix} \varepsilon_x^p(t) & 0 & 0 \\ 0 & -\frac{1}{2}\varepsilon_x^p(t) & 0 \\ 0 & 0 & -\frac{1}{2}\varepsilon_x^p(t) \end{bmatrix}. \quad (\text{A.3})$$

Total strain could be calculated as the sum of elastic and plastic strains.

$$\begin{aligned}\boldsymbol{\varepsilon}(t) = \boldsymbol{\varepsilon}^e(t) + \boldsymbol{\varepsilon}^p(t) &= \begin{bmatrix} \varepsilon_x^e(t) & 0 & 0 \\ 0 & -\nu\varepsilon_x^e(t) & 0 \\ 0 & 0 & -\nu\varepsilon_x^e(t) \end{bmatrix} + \begin{bmatrix} \varepsilon_x^p(t) & 0 & 0 \\ 0 & -\frac{1}{2}\varepsilon_x^p(t) & 0 \\ 0 & 0 & -\frac{1}{2}\varepsilon_x^p(t) \end{bmatrix} \\ \boldsymbol{\varepsilon}(t) &= \begin{bmatrix} \varepsilon_x^e(t) + \varepsilon_x^p(t) & 0 & 0 \\ 0 & -\nu\varepsilon_x^e(t) - \frac{1}{2}\varepsilon_x^p(t) & 0 \\ 0 & 0 & -\nu\varepsilon_x^e(t) - \frac{1}{2}\varepsilon_x^p(t) \end{bmatrix}.\end{aligned}\quad (\text{A.4})$$

In order to obtain the normal and shear stresses at a given plane, the stress and strain transformation equations could be used. Normal and shear stress can be calculated as follows:

$$\sigma'_x(t) = \frac{\sigma_x(t)}{2} + \frac{\sigma_x(t)}{2} \cos 2\theta, \quad (\text{A.5a})$$

$$\tau'_{xy}(t) = -\frac{\sigma_x(t)}{2} \sin 2\theta. \quad (\text{A.5b})$$

Normal and shear total strains can be calculated as follows:

$$\varepsilon'_x(t) = \left[\frac{2\varepsilon_x^e(t)(1-\nu) + \varepsilon_x^p(t)}{4} \right] + \left[\frac{2\varepsilon_x^e(t)(1+\nu) + 3\varepsilon_x^p(t)}{4} \right] \cos 2\theta, \quad (\text{A.6a})$$

$$\frac{\gamma'_{xy}(t)}{2} = - \left[\frac{2\varepsilon_x^e(t)(1+\nu) + 3\varepsilon_x^p(t)}{4} \right] \sin 2\theta. \quad (\text{A.6b})$$

Normal and shear plastic strains can be calculated as follows:

$$\varepsilon_x^{ip}(t) = \frac{\varepsilon_x^p(t)}{2} \left[\left(\frac{1 + \cos 2\theta}{2} \right) + \cos 2\theta \right], \quad (\text{A.7a})$$

$$\frac{\gamma_{xy}^{ip}(t)}{2} = -\frac{3\varepsilon_x^p(t)}{4} \sin 2\theta. \quad (\text{A.7b})$$

A.2 Torsional load

For a torsional load upon a linear elastic isotropic material, stress tensor $\boldsymbol{\sigma}$ could be written as follows:

$$\boldsymbol{\sigma}(t) = \begin{bmatrix} 0 & \tau_{xy}(t) & 0 \\ \tau_{xy}(t) & 0 & 0 \\ 0 & 0 & 0 \end{bmatrix}. \quad (\text{A.8})$$

The elastic component of the strain tensor $\boldsymbol{\varepsilon}$ could be calculated as follows:

$$\boldsymbol{\varepsilon}^e(t) = \begin{bmatrix} 0 & \frac{\gamma_{xy}^e(t)}{2} & 0 \\ \frac{\gamma_{xy}^e(t)}{2} & 0 & 0 \\ 0 & 0 & 0 \end{bmatrix}. \quad (\text{A.9})$$

The plastic component of the strain tensor $\boldsymbol{\varepsilon}$ could be calculated as follows:

$$\boldsymbol{\varepsilon}^p(t) = \begin{bmatrix} 0 & \frac{\gamma_{xy}^p(t)}{2} & 0 \\ \frac{\gamma_{xy}^p(t)}{2} & 0 & 0 \\ 0 & 0 & 0 \end{bmatrix}. \quad (\text{A.10})$$

Total strain could be calculated as the sum of elastic and plastic strains.

$$\begin{aligned} \boldsymbol{\varepsilon}(t) = \boldsymbol{\varepsilon}^e(t) + \boldsymbol{\varepsilon}^p(t) &= \begin{bmatrix} 0 & \frac{\gamma_{xy}^e(t)}{2} & 0 \\ \frac{\gamma_{xy}^e(t)}{2} & 0 & 0 \\ 0 & 0 & 0 \end{bmatrix} + \begin{bmatrix} 0 & \frac{\gamma_{xy}^p(t)}{2} & 0 \\ \frac{\gamma_{xy}^p(t)}{2} & 0 & 0 \\ 0 & 0 & 0 \end{bmatrix} \\ \boldsymbol{\varepsilon}(t) &= \frac{1}{2} \begin{bmatrix} 0 & \gamma_{xy}^e(t) + \gamma_{xy}^p(t) & 0 \\ \gamma_{xy}^e(t) + \gamma_{xy}^p(t) & 0 & 0 \\ 0 & 0 & 0 \end{bmatrix}. \end{aligned} \quad (\text{A.11})$$

In order to obtain the normal and shear stresses at a given plane the stress and strain transformation equations could be used. Normal and shear stress can be calculated as follows:

$$\sigma'_x(t) = \tau_{xy}(t) \sin 2\theta, \quad (\text{A.12a})$$

$$\tau'_{xy}(t) = \tau_{xy}(t) \cos 2\theta. \quad (\text{A.12b})$$

Normal and shear total strains can be calculated as follows:

$$\varepsilon'_x(t) = \left[\frac{\gamma_{xy}^e(t) + \gamma_{xy}^p(t)}{2} \right] \sin 2\theta, \quad (\text{A.13a})$$

$$\frac{\gamma'_{xy}(t)}{2} = \left[\frac{\gamma_{xy}^e(t) + \gamma_{xy}^p(t)}{2} \right] \cos 2\theta. \quad (\text{A.13b})$$

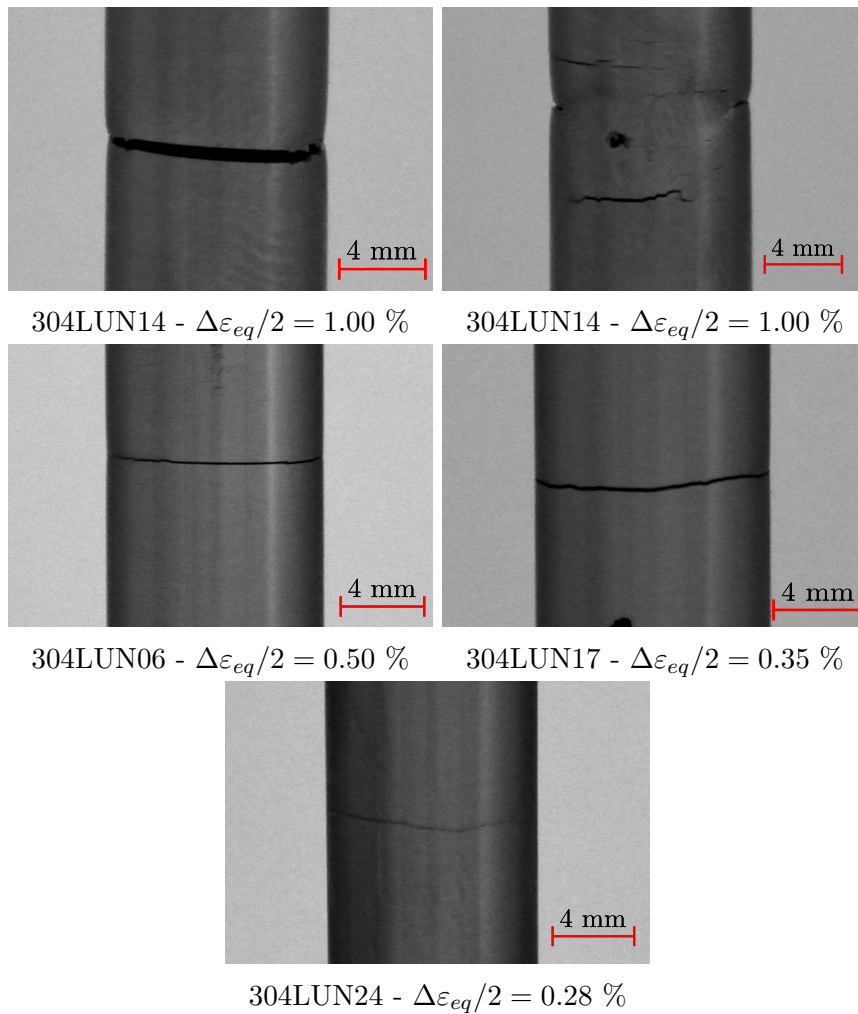
Normal and shear plastic strains can be calculated as follows:

$$\varepsilon_x{}^p(t) = \frac{\gamma_{xy}^p(t)}{2} \sin 2\theta, \quad (\text{A.14a})$$

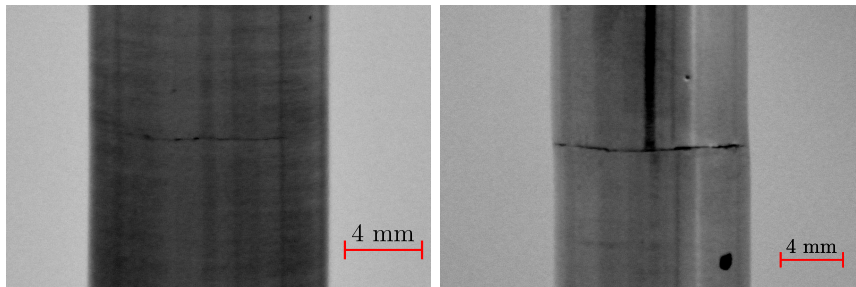
$$\frac{\gamma_{xy}{}^p(t)}{2} = \frac{\gamma_{xy}^p(t)}{2} \cos 2\theta. \quad (\text{A.14b})$$

Appendix B – Observed Fatigue Cracks

B.1 Axial Loading

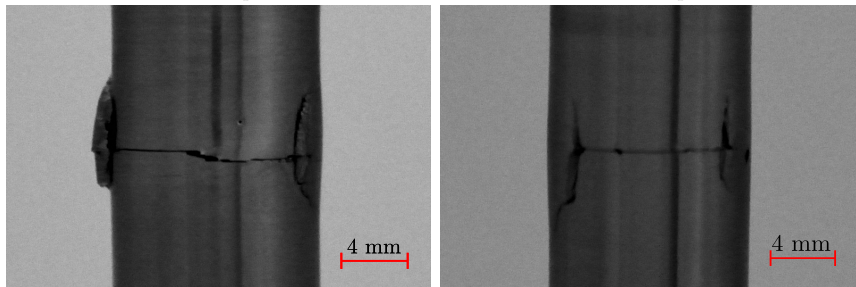


B.2 Torsional Loading



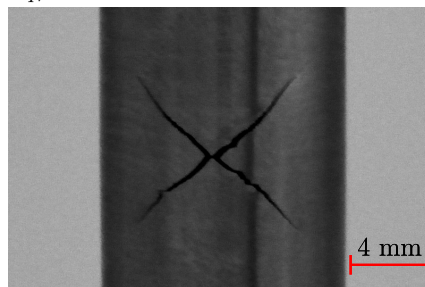
304LTU20 - $\Delta\varepsilon_{eq}/2 = 1.00\%$

304LTU29 - $\Delta\varepsilon_{eq}/2 = 1.00\%$



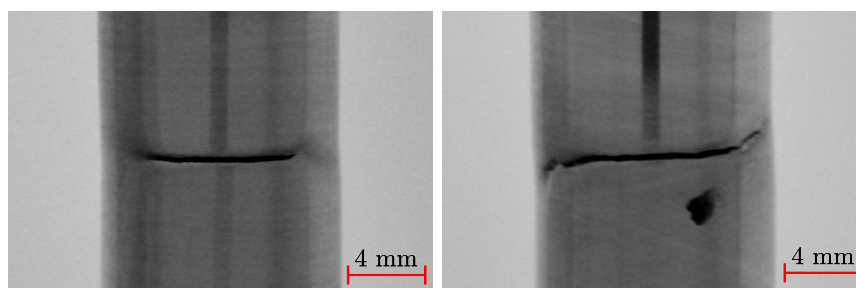
304LTU26 - $\Delta\varepsilon_{eq}/2 = 0.75\%$

304LTU21 - $\Delta\varepsilon_{eq}/2 = 0.50\%$



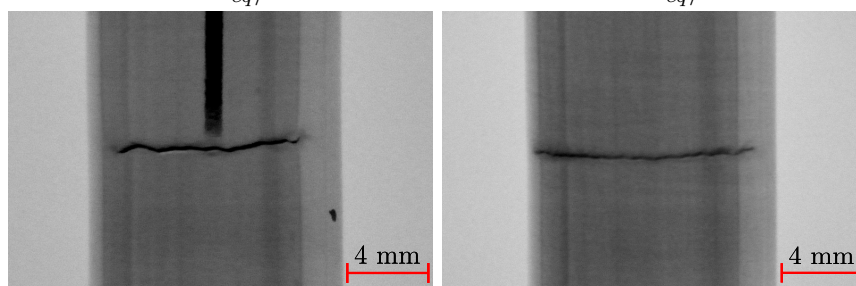
304LTU23 - $\Delta\varepsilon_{eq}/2 = 0.35\%$

B.3 Proportional Loading



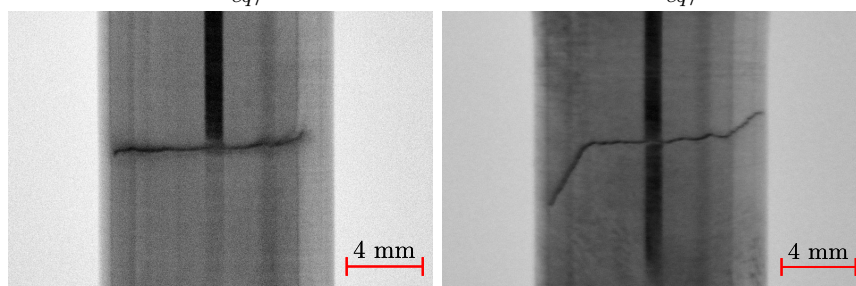
304LTU40 - $\Delta\varepsilon_{eq}/2 = 1.00\%$

304LTU37 - $\Delta\varepsilon_{eq}/2 = 0.80\%$



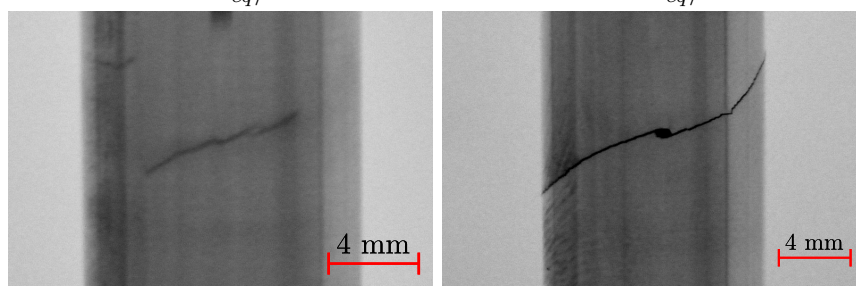
304LTU41 - $\Delta\varepsilon_{eq}/2 = 0.60\%$

304LTU33 - $\Delta\varepsilon_{eq}/2 = 0.60\%$



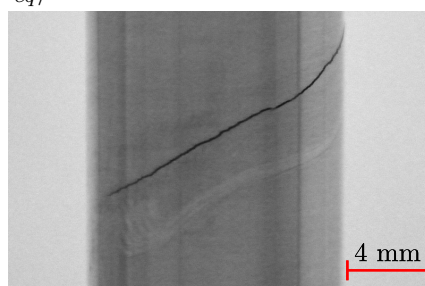
304LTU32 - $\Delta\varepsilon_{eq}/2 = 0.50\%$

304LTU35 - $\Delta\varepsilon_{eq}/2 = 0.40\%$



304LTU36 - $\Delta\varepsilon_{eq}/2 = 0.30\%$

304LTU42 - $\Delta\varepsilon_{eq}/2 = 0.24\%$



304LTU38 - $\Delta\varepsilon_{eq}/2 = 0.20\%$